NASA Technical Paper 3573

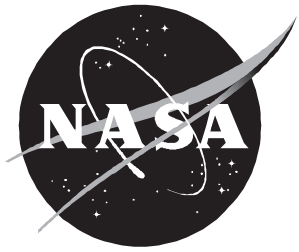

Computational Methods for Frictional Contact With Applications to the Space Shuttle Orbiter Nose-Gear Tire

Comparisons of Experimental Measurements and Analytical Predictions

John A. Tanner
Langley Research Center • Hampton, Virginia

National Aeronautics and Space Administration
Langley Research Center • Hampton, Virginia 23681-0001

May 1996

Acknowledgment

This report is based on a dissertation submitted to the faculty of the school of Engineering and Applied Sciences of The George Washington University in partial satisfaction of the requirements for the degree of Doctor of Science.

Available electronically at the following URL address: http://techreports.larc.nasa.gov/ltrs/ltrs.html

Printed copies available from the following:

NASA Center for AeroSpace Information
800 Elkridge Landing Road
Linthicum Heights, MD 21090-2934
(301) 621-0390

National Technical Information Service (NTIS)
5285 Port Royal Road
Springfield, VA 22161-2171
(703) 487-4650

Contents

Abstract

A computational procedure is presented for the solution of frictional contact problems for aircraft tires. A Space Shuttle nose-gear tire is modeled using a two-dimensional laminated anisotropic shell theory which includes the effects of variations in material and geometric parameters, transverse-shear deformation, and geometric nonlinearities. Contact conditions are incorporated into the formulation by using a perturbed Lagrangian approach with the fundamental unknowns consisting of the stress resultants, the generalized displacements, and the Lagrange multipliers associated with both contact and friction conditions. The contact-friction algorithm is based on a modified Coulomb friction law. A modified two-field, mixed-variational principle is used to obtain elemental arrays. This modification consists of augmenting the functional of that principle by two terms: the Lagrange multiplier vector associated with normal and tangential node contact-load intensities and a regularization term that is quadratic in the Lagrange multiplier vector. These capabilities and computational features are incorporated into an in-house computer code. Experimental measurements were taken to define the response of the Space Shuttle nose-gear tire to inflation-pressure loads and to combined inflation-pressure loads and static normal loads against a rigid flat plate. These experimental results describe the meridional growth of the tire cross section caused by inflation loading, the static load-deflection characteristics of the tire, the geometry of the tire footprint under static loading conditions, and the normal and tangential load-intensity distributions in the tire footprint for the various static vertical-loading conditions. Numerical results were obtained for the Space Shuttle nose-gear tire subjected to inflation-pressure loads and combined inflation-pressure and contact loads against a rigid flat plate. The experimental measurements and the numerical results are compared.

Introduction

Contact-friction problems are inherently nonlinear and path dependent. Nonlinearity occurs partly because both the contact area and the contact-load intensities are not known beforehand and vary during the loading history. Path dependency is a result of the nonconservative (irreversible dissipative) character of the frictional forces.

A review of static contact problems presented in reference 1, which includes a bibliography of approximately 700 papers, points out that contact problems are important to thermomechanical stress analyses, fracture mechanics, mechanical problems involving elastic foundations, the mechanics of joints, geomechanics, and tires.

Contact problems occupy a position of special importance in aircraft tire mechanics because the contact zone is where the forces are generated to support, guide, and maneuver the airplane. Distributions of contact loads and frictional forces define the moments and shears that are applied to the landing gear system (ref. 2). Under rolling conditions, the distribution of sliding velocities within the tire footprint combined with the frictional forces developed by the tire defines the rate of energy dissipation associated with the loading conditions and provides a measure of tire wear (refs. 3 and 4). In the case of the Space Shuttle orbiter, this wear mechanism is strong enough to cause tire failures during individual landing operations (refs. 5 and 6). Therefore, an understanding of these tire friction forces and the resulting slip velocities is critical to the design of aircraft tires for the next generation of high-performance aircraft, such as the National Aero-Space Plane and the High-Speed Civil Transport.

Modeling contact phenomena in the tire footprint is a formidable task partly because of difficulty of modeling tire response. Distribution of tractions and the footprint geometry are both functions of the normal, frictional, and inflation tire loads. Moreover, the complex mechanisms of dynamic friction, which allow the tire to develop the necessary steering and braking forces for aircraft control during ground operations, are not fully understood (ref. 7). The tire analyst thus is forced to choose among several friction theories. When the tire contact problem includes frictional effects, the solution becomes path dependent and a unique solution is not guaranteed.

The aircraft tire is a composite structure of rubber and textile constituents that exhibit anisotropic and nonhomogeneous material properties. Normal tire operating conditions create loads that can produce large deformations. Elevated operating temperatures from the combined effects of material hysteresis and frictional heating can cause variations in the material characteristics of the

tire constituents (refs. 8–10). The laminated carcass of the aircraft tire is thick enough to allow significant transverse-shear deformations.

These facts and attendant difficulties emphasize the need to develop modeling strategies and analysis methods that include efficient, powerful and economical contact algorithms. Intense research has recently focused on nonlinear analyses of static and dynamic problems involving contact. Novel techniques that have emerged from these efforts include semi-analytic finite-element models for nonlinear analysis of shells of revolution (refs. 11 and 12), reduced methods (refs. 13 and 14), and operator splitting techniques (refs. 15–17). References 14, 17, and 18 summarize applications of these new tire modeling techniques.

Objectives and Scope

Langley tire modeling research concentrates on developing an accurate and efficient strategy for predicting aircraft tire responses to a variety of loading conditions. This research focuses on developing tire contact modeling techniques, and the specific objectives of this research are (1) to develop a contact algorithm with friction effects included to predict tire response to combined inflation-pressure and static vertical-loading conditions, (2) to demonstrate the capabilities of this algorithm through numerical studies, and (3) to validate these numerical results with experimental data. Distribution of normal and frictional forces in the tire contact zone (or footprint area) is of particular interest.

The contact algorithm is incorporated into a mixed-formulation, two-field, two-dimensional finite-element model based on the moderate-rotation Sanders-Budiansky shell theory, including the effects of transverse-shear deformations, laminated anisotropic material response, and nonhomogeneous shell characteristics (refs. 19 and 20). A perturbed Lagrangian formulation (refs. 21 and 22) is the basis for this contact algorithm. The Lagrangian formulation uses the preconditioned conjugate gradient (PCG) iteration procedure (refs. 23–25) to determine contact area, distribution of normal-force intensities, and allocation of friction-force intensities. A modified version of the Coulomb friction law is incorporated into the contact algorithm in which the friction coefficient at the onset of sliding is different from that during sliding. This algorithm also monitors the energy dissipated within the sliding portion of the contact zone. In this investigation it will be assumed that the tire is loaded on a surface that is much stiffer than the tire, thus the surface will be treated as rigid. Hence, the static tire contact problem will be treated as a unilateral contact problem. Reference 26 summarizes the characteristics of this algorithm.

Numerical studies presented for an inflated Space Shuttle nose-gear tire under static load on a flat surface demonstrate the capabilities of the analysis techniques. These analyses incorporate both friction and frictionless contact. Detailed studies are made of the effects of tire tread pattern on the contact-force intensities, the influence of friction coefficient variations on the distribution of tire contact-force intensities, the convergence characteristics of the contact algorithm, and the history of energy dissipation in the static footprint.

Experimental measurements were carried out on the Space Shuttle orbiter nose-gear tire to define its response to combined inflation-pressure and static vertical-loading conditions. This report discusses experimental procedures used to define the tire structural response to loading conditions and to measure the footprint-force intensities and empirical procedures used to define the geometry and construction details of the tire for modeling purposes. Finally, the analytical results are compared with the experimental measurements.

This report describes numerical studies, experimental measurements, and comparisons between analytical results and experimental measurements. Reference 27 describes development of this contact algorithm.

Nomenclature

c_{ij}, d_{ij}, f_{ij}	tire stiffness coefficients (i, j = 1, 2, 6)
d	nylon cord diameter
E_1, E_2	Young's moduli
E_c, G_c	nylon cord moduli
E_r, G_r	rubber moduli
G_{23}, G_{13}, G_{12}	shear moduli
f_c	volume fraction of nylon cord
h	total thickness of tire
h_k	thickness of individual tire plies
n	normal vector to reference surface
p_0	intensity of inflation pressure
R_1, R_2	principal radii of curvature in meridional and circumferential directions
r	normal distance from tire axis to reference surface
s, θ	shell coordinates of tire
u, v, w	displacement components of reference surface of tire in meridional, circumferential, and normal directions (see fig. 1)
$\bar{w}$	normal displacement at $\varepsilon = \theta = 0$ (see fig. 7)

$\mathbf{x}$	two-dimensional position vector (see eq. (3))
$\mathbf{y}$	data vector
x, y, z	Cartesian coordinate system
$\varepsilon_1, \varepsilon_2, \varepsilon_s, \varepsilon_\theta, 2\varepsilon_{s\theta}$	extensional strains of tire reference surface
$2\varepsilon_{s3}, 2\varepsilon_{\theta 3}$	transverse-shear strains of tire
$\gamma_{23}, \gamma_{13}, \gamma_{12}$	shear strains of tire reference surface
ν_{12}, ν_{21}	Poisson's ratio
κ_1, κ_2	curvatures (see eq. (6))
$\kappa_s, \kappa_\theta, 2\kappa_{s\theta}$	bending strains of tire
σ	tension factor (see eq. (1))
σ'	normalized tension factor
σ_1, σ_2	elongation stresses of tire
θ	circumferential (hoop) coordinate of tire (see fig. 1)
$\tilde{\theta}, \tilde{\theta}_k$	nylon cord orientation angle (see eq. (22))
ξ	dimensionless coordinate along meridian (see fig. 4)
ϕ	rotation about normal to tire reference surface (see eq. (A9))
ϕ_s, ϕ_θ	rotational components of reference surface of tire (see fig. 1)
$\tau_{23}, \tau_{13}, \tau_{12}$	shear stresses of tire

Geometric and Stiffness Characteristics of Space Shuttle Orbiter Nose-Gear Tire

Tire Description

Numerical studies conducted assess the accuracy of the two-dimensional shell tire model, effectiveness of the proposed computational procedure, and performance of the contact algorithm. The 32 × 8.8, type VII, 16-ply-rating Space Shuttle orbiter nose-gear tire was modeled during these studies as a two-dimensional laminated shell with variable thickness and variable stiffness characteristics. The outer surface of the tire was used as the reference surface of the shell model. Figure 1 gives geometric characteristics of the tire. The tire carcass is constructed of 10 lamina of nylon and rubber with an additional reinforcing ply beneath the tire tread. (See fig. 2.) The tire has a three-groove tread pattern. The rated load for the tire is 15 000 lbf at an inflation pressure of 320 psi. All experiments and analyses were conducted at an inflation pressure of 300 psi.

The following sections describe the empirical procedures used to establish the tire geometry and to define the global elastic response of the tire to inflation and static vertical-loading conditions. These sections also present an evaluation of the tire stiffness characteristics.

Modeling of Tire Geometry

A Space Shuttle nose-gear tire was cut into sections and used to obtain accurate measurements of the cross-sectional profile of an uninflated tire. A smoothed spline under tension was used to fit a curve through the measured coordinates of the cross-sectional profile in a least-squares sense. (See refs. 28 and 29.) Because of symmetry, only half the cross section was modeled. A piecewise linear and continuous estimate of the second derivative d^2x/dz^2 was required by the cubic spline function, and this was achieved by adjusting the standard deviations of the measured profile at the data points. The second derivative with the effect of tension included is denoted by

$$\ddot{\mathbf{x}}(s) - \sigma^2\mathbf{x}(s) = \left[\ddot{\mathbf{x}}(s_i) - \sigma^2\mathbf{y}_i\right]\frac{s_{i+1}-s}{s_{i+1}-s_i} + \left[\ddot{\mathbf{x}}(s_{i+1}) - \sigma^2\mathbf{y}_{i+1}\right]\frac{s-s_i}{s_{i+1}-s_i} \quad (1)$$

for $(s_i \le s \le s_{i+1})$ where $\mathbf{x} = [x(s), z(s)]$ is the position vector for points along the segment, $\mathbf{y}_i = [x, z]_i$ is the corresponding data at point i, and a dot over a symbol denotes a derivative with respect to s. The chordal length (polygonal arc length) s_i is given by the following equation:

$$\left.\begin{aligned} s_1 &= 0 \\ s_i &= s_{i-1} + \left[(x_i - x_{i-1})^2 + (z_i - z_{i-1})^2\right]^{1/2} \end{aligned}\right\} \quad (2)$$

After solving equation (1) for $x(s)$ and replacing $\mathbf{x}(s_i)$ with $\mathbf{y}_i$, the following expression is obtained:

$$\mathbf{x}(s) = \frac{\left[\frac{\ddot{\mathbf{x}}(s_i)}{\sigma^2}\right]\sinh\sigma(s_{i+1}-s)}{\sinh\sigma(s_{i+1}-s_i)} + \frac{\left[\mathbf{y}_i - \frac{\ddot{\mathbf{x}}(s_i)}{\sigma^2}\right](s_{i+1}-s)}{s_{i+1}-s_i} + \frac{\left[\frac{\ddot{\mathbf{x}}(s_{i+1})}{\sigma^2}\right]\sinh\sigma(s-s_i)}{\sinh\sigma(s_{i+1}-s_i)} + \frac{\left[\mathbf{y}_{i+1} - \frac{\ddot{\mathbf{x}}(s_{i+1})}{\sigma^2}\right](s-s_i)}{s_{i+1}-s_i} \quad (3)$$

Upon differentiating equation (3) and equating right- and left-side derivatives at s_i (for $i = 2, 3, \ldots, l-1$), a set of linear algebraic equations for $\ddot{\mathbf{x}}(s_i)$ is obtained. With the assumption of a nonperiodic spline function in which the slopes at s_1 and s_l are given, the tridiagonal differential equation is easily solved. Once the second derivatives at point $i = 1, 2, \ldots, l$ are obtained, the first and second derivatives at the interpolation points $\dot{\mathbf{x}}(s)$ and

$\ddot{\mathbf{x}}(s)$ are evaluated by differentiating equation (3). References 29–31 give a detailed description of spline smoothing techniques.

A normalized tension factor is used to eliminate a nonlinear behavior by setting (see ref. 32)

$$\sigma' = \frac{\sigma(s_l - s_1)}{l - 1} \tag{4}$$

In practice, if this factor is less than 0.001, the resulting curve is approximately a cubic spline; if it is greater than 50, the curve is nearly piecewise linear. It should be noted that the variable s in equations (1)–(4) is not the actual arc length but the chordal length approximation of s. Thus, the accuracy of the arc length approximation is a function of the number of points used in the smoothing procedure.

Computed arc length s, coordinates x and z, and first and second derivatives $\dot{\mathbf{x}}(s)$ and $\ddot{\mathbf{x}}(s)$ are used to evaluate the various geometric parameters of the tire.

Normal vector:

$$\mathbf{n} = \begin{Bmatrix} \sin\phi \\ \cos\phi \end{Bmatrix} = \begin{Bmatrix} \dfrac{-dx/ds}{\sqrt{(dx/ds)^2 + (dz/ds)^2}} \\ \dfrac{dz/ds}{\sqrt{(dx/ds)^2 + (dz/ds)^2}} \end{Bmatrix} \tag{5}$$

Curvatures:

$$\kappa_1 = \frac{1}{R_1} = -\cos^3\phi\left(\frac{d^2x}{dz^2}\right) \tag{6}$$

$$\kappa_2 = \frac{1}{R_2} = \frac{\cos\phi}{x} \tag{7}$$

Figure 3 presents the resulting geometric characteristics of the Space Shuttle nose-gear tire. Thicknesses of the tire carcass at the node points of the finite-element model were computed along the normal vector to the tire reference (outer) surface by locating the points of intersection of the normal vectors with the inner surface of the tire carcass. To facilitate these computations the tire inner surface was approximated by a set of third-degree polynomials.

Evaluation of Stiffness Coefficients of Two-Dimensional Shell Model

The cord-rubber composite was treated as a laminated material. For the purpose of computing stiffness variations in the meridional direction, the tire model was divided into seven regions. (See fig. 2.) Thickness of the individual carcass plies was measured at the interfaces between the regions and these values are given in table 1. A linear variation was assumed for the thickness within each region. Thickness of the tire tread and sidewall covering was computed by subtracting the sum of the individual ply thicknesses from the total thickness of the carcass at each location.

Material properties of the different plies were obtained with the mechanics of materials approach, which is widely applied to rigid composites. (See refs. 33 and 34.) Table 2 presents elastic constants of the tire constituents used in this study. It was assumed that nylon cords of two different diameters were used in the construction of the tire. In region I, d = 0.022 in. for the bottom two plies and the tread reinforcement, and d = 0.031 in. for all other plies. Table 3 gives cord end counts (epi) for individual plies at the region interfaces. A linear variation was assumed for epi within each region.

Stress-strain relationships of the individual orthotropic and unidirectional layers are given by

$$\begin{Bmatrix} \sigma_1 \\ \sigma_2 \\ \tau_{23} \\ \tau_{13} \\ \tau_{12} \end{Bmatrix} = \begin{bmatrix} c_{11} & c_{12} & \bullet & \bullet & \bullet \\ c_{12} & c_{22} & \bullet & \bullet & \bullet \\ \bullet & \bullet & c_{44} & \bullet & \bullet \\ \bullet & \bullet & \bullet & c_{55} & \bullet \\ \bullet & \bullet & \bullet & \bullet & c_{66} \end{bmatrix} \begin{Bmatrix} \varepsilon_1 \\ \varepsilon_2 \\ \gamma_{23} \\ \gamma_{13} \\ \gamma_{12} \end{Bmatrix} \tag{8}$$

where the reduced stiffnesses c_{ij} are given by

$$c_{11} = \frac{E_1}{1 - \nu_{12}\nu_{21}} \tag{9}$$

$$c_{12} = \frac{E_1\nu_{21}}{1 - \nu_{12}\nu_{21}} \tag{10}$$

$$c_{22} = \frac{E_2}{1 - \nu_{12}\nu_{21}} \tag{11}$$

$$c_{44} = G_{23} \tag{12}$$

$$c_{55} = G_{13} \tag{13}$$

$$c_{66} = G_{12} \tag{14}$$

Elastic constants are computed by the law of mixtures (see ref. 34)

$$E_1 = E_c f_c + E_r(1 - f_c) \tag{15}$$

$$\nu_{12} = \nu_c f_c + \nu_r(1 - f_c) \tag{16}$$

$$E_2 = \frac{E_r[E_c(1 + 2f_c) + 2E_r(1 - f_c)]}{E_c(1 - f_c) + 2E_r(1 + 0.5f_c)} \tag{17}$$

$$G_{12} = G_{13} = \frac{G_r[G_c + G_r + (G_c - G_r)f_c]}{[G_c + G_r - (G_c - G_r)f_c]} \tag{18}$$

$$G_{23} = 0.6G_{12} \tag{19}$$

$$\nu_{21} = \frac{\nu_{12}E_2}{E_1} \tag{20}$$

where subscripts c and r represent the quantities of the nylon cord and the rubber, respectively, and f_c is the volume fraction of the nylon cord

$$f_c = \frac{\pi d^2(\text{epi})}{4h_k} \tag{21}$$

where d is cord diameter, h_k is layer thickness, and epi is cord end count (in ends per inch).

Stress-strain relationships of the two-dimensional shell were obtained by first transforming the stiffness of each of the individual layers to the global shell coordinates s and θ and then integrating these coefficients through the thickness. Table 4 gives cord orientations in the individual plies of each region. The following formula was used to determine $\tilde{\theta}_k$, the angle (in degrees) measured from the s-axis to the θ-axis, at the numerical quadrature points:

$$\tilde{\theta} = \max[(54.382 - 3.884\xi - 148.96\xi^2)°, 33°] \tag{22}$$

where ξ is the dimensionless coordinate along the tire meridian.

The appendix gives the resulting shell constitutive relations. Figure 4 shows meridional variations of the stiffness coefficients.

Experimental Measurements

A substantial experimental program has been underway at Langley for several years to obtain measurements of the Space Shuttle nose-gear tire response to various loading conditions. The following sections describe these experimental measurements and the techniques used to obtain them.

Measurements of Inflated Cross-Sectional Profile and Vertical Load-Deflection Response

Close-range photogrammetry measurements. Close-range photogrammetry techniques were used to define the inflated profile of the Space Shuttle orbiter nose-gear tire. To facilitate these measurements, 209 circular, reflective targets were attached to the Space Shuttle nose-gear tire as shown schematically in figure 5. Targets were aligned along 19 meridional lines of the tire sidewall and a video camera was used to record the target positions from 10 different camera locations. A stereophotography triangulation technique (refs. 35 and 36) was used to define the location of each target in a global coordinate system from these video images. The root mean square (rms) measurement accuracies were found to be 1.3 mils, 2.9 mils, and 1.5 mils in the x-, y-, and z-coordinate directions, respectively.

The same triangulation techniques were used to assess the ability of the loading fixture to subject the tire and wheel to a pure vertical load. Results of this triangulation study (illustrated in table below) indicate that there is a significant misalignment in the loading fixture that must be taken into account when analyzing the experimental results.

Fore and aft displacement	Lateral displacement	Vertical displacement
0.09 in.	–0.02 in.	1.42 in.

Figure 6 shows unloaded and loaded profiles of a portion of the Space Shuttle nose-gear tire sidewall. The intersections of the lines in figure 6 denote the locations of the photogrammetry targets shown in figure 5. The dashed lines represent the tire sidewall geometry under a uniform inflation-pressure loading of 300 psi. The solid lines in the figure represent the tire sidewall geometry when the inflated tire is loaded onto a rigid, flat plate. For this static-loaded case, the tire cross section was deflected approximately 1.42 in. in the direction normal to the surface. Three data points are missing for the loaded case because the flat plate that the tire was loaded against interfered with the field-of-view of the camera. Data in figure 6 indicate that the tire sidewall in the vicinity of contact bulges outward radially under the influence of the vertical load.

Static vertical load-deflection measurements. Static vertical load-deflection tests conducted on the inflated Space Shuttle nose-gear tire provide a global measure of tire elastic response. For these tests the tire was slowly lowered onto the flat plate until a maximum vertical load of approximately 30 000 lbf was obtained and then slowly unloaded until the tire lost contact with the

surface. During this loading process an *x-y* plotter was used to monitor the resulting tire hysteresis loop. (See fig. 7.) The resulting load-deflection curve indicates that the nonlinear response of the tire is similar to a hardening spring. The hysteresis loop provides a measure of the damping of the tire, but for this study the damping term was omitted.

Tire Footprint Geometry

Reference 37 presents data on the footprint geometry for a number of tires, including the Space Shuttle nose-gear tire. The footprint shapes were obtained by applying a mixture of lightweight oil and graphite powder on the tire tread area and statically loading the tire at preselected vertical loads onto posterboard affixed to the rigid flat plate. The following paragraphs provide information on the measured geometric characteristics of the Space Shuttle nose-gear tire footprints obtained over a range of vertical-loading conditions at an inflation pressure of 300 psi.

Footprint length and width measurements under static loading conditions. Figure 8 plots the length of the Space Shuttle nose-gear tire footprint as a function of vertical load. The symbols denote the specific incremental load applications ranging from 2000 lbf to 30 000 lbf. The line through the points represents a cubic least-squares curve fit to the data. Figure 8 also lists the equation representing the curve fit. Footprint length grew from slightly over 4 in. at a load of 2000 lbf to approximately 14 in. at 30 000 lbf. The data indicate that the rate of increase in footprint length decreases as the vertical load increases.

Figure 9 plots the width of the Space Shuttle nose-gear tire footprint as a function of vertical load. Various incremental loads between 2000 lbf and 30 000 lbf are denoted by the circular symbols in figure 9, and the cubic least-squares curve fit to the data is denoted by the line through the points. The equation of the curve fit is included in figure 9. Footprint width grows from slightly more than 2 in. at the 2000-lbf normal load case to a maximum width of about 7 in. at the 30 000-lbf loading condition. Data presented in figure 9 indicate that the rate of growth in footprint width diminishes as the vertical load increases.

Figure 10 plots footprint width for the Space Shuttle nose-gear tire as a function of footprint length. Data presented in this fashion indicate that there is a linear relationship between the length and width of the Space Shuttle nose-gear tire over the range of vertical loads investigated. The least-squares equation expressing this relationship is shown in figure 10.

Footprint area measurements under static loading conditions. Figure 11 plots the footprint area of the Space Shuttle nose-gear tire as a function of the applied vertical load. Numerical integration techniques were used to acquire the area measurements for each of the tire footprints at various vertical-loading conditions. For each footprint, two measurements were taken. The first measurement was obtained by computing the total area enclosed in the tire contact zone, including the tread groove area(s). These data are denoted by the circular symbols in figure 11 and are referred to as the gross footprint areas. The second measurement was obtained by computing the contact area of the individual contact lobes independently. These measurements, denoted by the square symbols in figure 11, are referred to as the net footprint areas and exclude the tread groove area(s) for each footprint. Both the gross and net footprint areas increase in a linear fashion as the vertical load is increased over the range of loads investigated. The linear least-squares curve fit to each data set, along with its equation, is presented in figure 11.

Figure 12 plots the ratio of net to gross footprint areas for the Space Shuttle nose-gear tire as a function of vertical load. The data in figure 12 indicate that the ratio of net to gross footprint areas is nearly constant over the range of vertical-loading conditions tested. This ratio is approximately 0.8 for the 2000-lbf load case and about 0.81 for the 30 000-lbf load case.

Tire Footprint Load Intensities

Tire footprint-force transducer. Reference 37 describes the tire footprint-force transducer used to obtain triaxial measurements in the contact region of the statically loaded Space Shuttle nose-gear tire. The force transducer includes 10 beam-columns spaced 1.36 in. from center to center with a 0.25 in^2 surface area. Each beam-column was instrumented to measure force components in the normal and the two tangential directions. The two tangential forces represent the components of the friction forces in the footprint.

The beam-columns measure total force within the beam-column contact surface. It should be noted that the instrumentation could not distinguish between distributed loads and concentrated loads at discrete points. For the purpose of this investigation, the forces were assumed to be distributed load intensities over the net contact area of the individual beam-columns.

Tire footprint areas and load intensity measurement procedures. Figure 13 shows schematically the tire footprint areas and the map of tire footprint-force transducer locations used to obtain the data with the Space Shuttle nose-gear tire for three distinct vertical-loading

cases: 2000 lbf, 15 000 lbf, and 30 000 lbf. The sequence of testing places the tire footprint-force transducer on top of the rigid flat plate with the row of beam-columns aligned with the meridional coordinate of the tire. The transducer was initially positioned at approximately the center of the footprint. The load was then applied incrementally up to the maximum load of 30 000 lbf, and data were recorded for each vertical-loading increment. For succeeding load applications, the tire footprint-force transducer was moved either forward or aft at half-inch increments in the footprint so that the entire footprint region was eventually covered.

In figure 13 the map of the tire footprint-force transducer locations is superimposed on the tire footprint. A trial-and-error iterative process was used to make small adjustments in positioning the transducer map on the tire footprint shapes. The final position of the transducer map shown in figure 13 is consistent with the pattern of nonzero force measurements for the various vertical-load cases reported in reference 37. The footprint shapes and the transducer outlines are drawn to scale in figure 13. It should be noted, however, that there is some uncertainty in the definition of the experimental footprint areas outlines from forces such as scrubbing (or squirm) in the footprint areas during the application of the static vertical loads.

Figure 13 also identifies the centers of contact for each beam-column and the percentage of actual contact for each beam-column that experienced less than full contact, i.e., loss of contact at the edge of the footprint or in the vicinity of tread grooves. This information was used to convert the transducer-force measurements into load intensity by dividing each normal- or tangential-force measurement by the appropriate beam-column contact area. The information in figure 13 also defines the contact boundary along the footprint periphery and along the edges of the tread grooves. Thus, each tire tread contact area (the ribs between the tread grooves) was treated as an independent zone or lobe of contact.

Symmetries exhibited by Space Shuttle nose-gear tire footprint. Figure 14 shows the symmetry exhibited in the Space Shuttle nose-gear tire contact area. For each vertical-loading condition, the tire footprint is shown two ways. The first plot shows the mirror image of the left half of the tire footprint (denoted by the dashed outline) superimposed over the right half of the footprint. The second plot shows the image of the left half of the tire footprint (denoted by the dashed outline) rotated by 180° about the centroid of contact superimposed over the right half of the footprint. The centroids of the contact areas are denoted by the plus signs in figure 13. The data presented in figure 14 indicate that the footprint of the Space Shuttle nose-gear tire exhibits rotational or inversion symmetry rather than reflective symmetry. The misalignments of the rotated dashed footprint outline relative to the solid footprint outline are a function of both the uncertainty of the footprint outline from the scrubbing during the loading history and imperfections in the tire construction.

Contour plots. Figures 15–17 present contour plots of measured tire footprint load intensities in the normal and two tangential directions. Figure 13 shows the location of the sensors used to obtain these load-intensity measurements. Caution should be exercised when interpreting this contour information because the contour patterns are sensitive to the sensor locations that were used to obtain the measurements. Note that for the 2000-lbf and 15 000-lbf load cases the data used to produce the contour plots were derived from a single row of sensors for each tire footprint contact lobe. For the 30 000-lbf load case a single row of sensors was used for the two inner lobes and a double row of sensors was employed for the outer lobes. The solid lines outlining the contour plots represent the experimentally-determined footprint areas for each load case.

Normal footprint load intensities. Figure 15 presents the distribution of normal load intensities in the form of contour plots for normal loads of 2000 lbf, 15 000 lbf, and 30 000 lbf. Rated load for the Space Shuttle nose-gear tire is 15 000 lbf at an inflation pressure of 320 psi. For the 2000-lbf normal load case (fig. 15(a)) peak normal load intensity is between 450 and 500 psi. At this loading condition only the two inner tread ribs (or lobes) are in contact with the surface. At a normal load of 15 000 lbf, the tire contact zone expands to include the two outer tread ribs. (See fig. 15(b).) Maximum normal load intensity for the 15 000-lbf load case is also 450 psi to 500 psi, but the footprint area of the tire increases substantially over the 2000-lbf load case footprint.

The contour plot in figure 15(c) for the 30 000-lbf normal load condition indicates the presence of a localized maximum load intensity along the outer edge of one of the outside circumferential tread grooves, and is shown in the bottom right corner of the tire contact zone in figure 15(c). This peak load intensity ranges between 650 psi and 700 psi. In the center of the outer contact lobes the normal load intensities range between 500 psi and 550 psi, and in the center of the inner lobes the normal load intensities range between 400 psi and 450 psi for the 30 000-lbf normal load condition. These maximum load intensities are equal in magnitude to approximately 150 percent to 180 percent of the inflation pressure.

Tangential load intensities in lateral direction. Figure 16 shows the lateral friction load-intensity distributions for the Space Shuttle nose-gear tire. For the

2000-lbf normal load case (fig. 16 (a)), the lateral friction load-intensity measurements indicate negative load intensities of −24 psi to −30 psi on the bottom contact lobe and a maximum positive lateral load intensity of 6 psi to 12 psi on the upper contact lobe. These lateral-traction load intensities retard the lateral growth of the tire footprint. Loss of skew symmetry in the lateral friction load-intensity distribution for the 2000-lbf load case is attributed to the misalignment in the loading fixture which allowed a slight lateral displacement of the tire during application of the normal load. Arrows in figure 16(a) indicate the directions of tire deflection associated with this misalignment. When the normal load is increased to 15 000 lbf (fig. 16(b)), the magnitude of the peak lateral friction load intensity is also increased to 75 psi to 90 psi and the four contact lobes exhibit a distribution of lateral load intensities which features an alternating sequence of positive and negative load-intensity regions. At 30 000 lbf (fig. 16(c)) peak lateral friction load intensities are increased to 125 psi to 150 psi and the alternating bands of positive and negative surface tractions are especially prominent. Loss of skew symmetry in the lateral friction load intensities is not as obvious for the larger normal load cases as it is for the 2000-lbf normal load case. Peak lateral friction load intensities occur near the lateral extremities of the tire footprint for the load conditions investigated.

Tangential load intensities in fore and aft direction. Figure 17 shows measured fore and aft tangential (or drag) friction load-intensity distributions for the Space Shuttle nose-gear tire inflated to 300 psi. For the 2000-lbf normal load case shown in figure 17(a), drag friction load-intensity measurements indicate that positive load intensities are present in both contact lobes and peak positive load intensities of 10 psi to 15 psi are located about 1 in. left of the center of contact. Fore and aft extremities of the tire footprint exhibit negative drag friction load intensities ranging up to −15 psi. Positive load intensities retard forward displacement of the tire footprint associated with misalignment of the loading fixture. Arrows in figure 17(a) indicate the directions of tire deflection associated with this misalignment. At a normal load of 15 000 lbf (fig. 17(b)) drag friction load intensities increase to a maximum positive value of 32 psi to 40 psi in the two inner lobes about 3 in. on either side of the contact center. Maximum negative drag friction load intensities of −8 psi to −16 psi are observed near the right edge of contact in the two center lobes in figure 17(b) and there is a sharp transition between positive and negative forces about 4 in. right of the center of contact. When normal force is increased to 30 000 lbf (fig. 17(c)) the transition between positive and negative drag friction load intensities is very prominent. Peak drag friction load intensities, both positive and negative, are 72 psi to 84 psi. About one quarter of the tire contact area is subjected to negative drag friction load intensities, and the remaining three quarters of the tire footprint are subjected to positive drag friction load intensities. Positive drag friction load intensities are minimum at the center of contact for each of the normal load cases. (See figs. 17(a)–(c).)

Numerical Results and Correlation With Experimental Results

Description of Finite-Element Models

To develop the finite-element models used in the analysis of the Space Shuttle nose-gear tire, the cubic spline approximation of the outer meridional surface of the tire half cross section was discretized into 75 potential node points. (See fig. 18.) From this population of possible nodes, a smaller number of nodes was chosen to approximate the tire cross section. To model the tire inflation response, a single strip of 30 finite elements was used to approximate the complete tire cross section. This model employed 61 nodes to characterize the tire meridian, and there were a total of 480 stress-resultant parameters and 293 nonzero generalized-displacement parameters to synthesize the tire inflation response.

Finite-element models employed to analyze the contact behavior and friction characteristics of the Space Shuttle nose-gear tire used 41 node points in one half of a meridional cross section (81 nodes for the entire cross section) and these nodes are denoted as the circular symbols in figure 18. Nodes associated with the circumferential tread grooves are also highlighted in figure 18. In the meridional direction, the tread area of the tire was modeled with the highest density of nodes and the sidewall and bead areas were modeled with progressively fewer nodes. This meridional node pattern was used for each of the two-dimensional finite-element tire models employed in this investigation. The circumference of the tire was divided into 240 possible node points and a smaller number of nodes was chosen from that population to construct the tire finite-element models. To refine the mesh in specific areas such as the contact zone, a higher density of nodes was chosen from the population in the specific region of interest.

Figure 19 shows a map of elements and node locations for one of the models used to analyze the contact problem. Figure 19 shows an array of elements, with 40 elements in the meridional direction and 18 elements in the circumferential direction. Numbers in the left and right margin of the figure denote the beginning and ending element numbers in specific rows. Black dots superimposed over the square grid of elements denote the individual nodes of the finite-element model. Several

individual elements are shaded and shown in an expanded scale to illustrate the node numbering sequence that was used to minimize the bandwidth for the finite-element models. The complicating factor here is that the elements in the circumferential direction are joined along the top and bottom edge. The numbering scheme that is illustrated in the example shown in figure 19 provides a minimum bandwidth for this tire model. For this specific example the bandwidth is 1635. The six rows of elements in the middle of the array, containing elements 1 through 240, comprise the possible contact region for this model. Also shown in figure 19 is the location of the circumferential tread grooves of the Space Shuttle nose-gear tire.

Three different models were used in the analysis of the Space Shuttle nose-gear tire in contact with a flat plate. These models, denoted as model 1, model 2, and model 3, are depicted in figure 20. Each model employed 480 elements in the region outside the contact zone ($\theta < -0.2\pi$, $\theta > 0.2\pi$). Model 1 includes 240 elements in the contact region of the tire ($-0.2\pi \le \theta \le 0.2\pi$) for a total of 720 elements. (See fig. 19.) Model 1 includes 14 076 nonzero generalized displacement parameters, 23 040 stress resultant parameters, and 3159 contact load-intensity parameters. Model 2 used a refined mesh within the contact region, with 480 contact elements and a total of 960 elements. Model 2 includes 18 776 nonzero generalized displacement parameters, 30 720 stress resultant parameters, and 6075 contact load-intensity parameters. Model 3 employed a more refined mesh in the contact zone, with 960 contact elements and a total of 1440 elements. Model 3 employed 28 152 generalized displacement parameters, 46 080 stress resultant parameters, and 11 907 contact load-intensity parameters. A single iteration for model 1 required about 12 min on a Cray 2 computer, and a single iteration for model 3 required about 12 min on a Cray Y-MP computer.

Correlation Between Analytical Results and Experimental Measurements

Tire response to inflation-pressure loading. To assess the accuracy of the high fidelity carcass model of the Space Shuttle nose-gear tire, profile deformations produced by a uniform inflation pressure of 300 psi and acting normal to the interior surface were calculated using a strip of geometrically nonlinear shell finite elements described above. Figure 21 presents inflated and uninflated cross-sectional profiles for the Space Shuttle nose-gear tire. The primary effect of inflation pressure is to expand the tire profile in the cross-sectional regions I–V. (See fig. 2.) The predicted inflated profile is in excellent agreement with the measured profiles from the photogrammetry studies. Photogrammetry data from a number of tire cross sections (denoted by the different symbols) are compared with the model predictions in figure 21. These results clearly illustrate the axisymmetric characteristics of the tire response to inflation loads. Reference 38 presents additional information on inflation pressure results.

Tire load-deflection and load-contact-area characteristics. One global measure of tire response to static contact loading is the normal load-deflection curve. Figure 22 presents measured and calculated normal load-deflection curves for the Space Shuttle nose-gear tire inflated to 300 psi and loaded against a flat plate. The measured load-deflection curve is denoted by square symbols in figure 22 and a quadratic curve is used to fair the measurements in a least-squares fashion. The calculated load-deflection response of the tire was obtained by taking the product of the predicted normal load intensities and the calculated contact area at each contact node and summing them over all contact nodes. Circular symbols denote the predicted load-deflection response based on the Newton-Cotes quadrature calculation of the contact areas associated with each contact node. Triangular symbols denote the predicted load-deflection response based on the contact area algorithm described in reference 27. Both calculation procedures perform well in matching the measured normal tire load-deflection response, but the calculation procedure based on the contact area algorithm appears to be more accurate over the load range analyzed.

A second global measure of tire response to static contact loading is the normal-load-contact-area behavior. Figures 23 and 24 present measured and calculated normal-load-contact-area characteristics of the Space Shuttle nose-gear tire subjected to static contact loading against a flat plate. In figure 23 measured and predicted net footprint areas are plotted as a function of the applied normal load. Net footprint area is defined as the sum of the contact areas of the individual tire tread ribs or lobes (see fig. 15, for example) and excludes the areas associated with the circumferential grooves. In figure 24 the gross footprint areas are plotted as a function of the applied normal load. Gross footprint area is defined as the total contact area of the tire, and the groove areas are included in this parameter. For a smooth tread tire, the net and gross footprint areas are identical.

Figures 23 and 24 denote experimental data by square symbols. Predicted contact areas based upon the Newton-Cotes quadrature calculation are denoted by circular symbols and the dashed linear curve representing a least-squares fairing of the analytical results. Predicted contact areas based upon the contact-area algorithm calculations are denoted by triangular symbols and the solid linear curve least-squares fairing of the analytical results.

Results presented in figures 23 and 24 indicate that contact-area predictions based upon the contact-area algorithm are much more accurate than those based upon the Newton-Cotes quadrature calculation. Predicted net footprint areas are more accurate than those of the gross footprint areas regardless of the calculation method used. Results presented in figures 23 and 24 also indicate that additional fine-tuning of the contact-area algorithm is needed for improved contact-area predictions, especially at the higher normal load conditions.

Figure 25 presents the method of obtaining a prediction of the tire footprint shape from the analytical results. Figure 25 shows a map of contact nodes, denoted by square symbols, in and around the footprint area projected onto the contact surface. Dark symbols represent nodes that are in contact with the flat surface and light symbols represent nodes that are not in contact. A solid line denotes the measured footprint outline obtained from the lightweight oil and graphite powder footprint stamps described previously in reference 37. A dashed line represents an elliptical curve approximation of the footprint shape based on the distribution of contact nodes. For the 2000-lbf normal load case shown in figure 25(a), measured and calculated footprint widths are in close agreement, but predicted footprint length is less than the measured length. These measured and/or calculated footprint shapes are included in figures 26–31 as an aid in interpreting the footprint load-intensity data. For the 15 000-lbf normal load case shown in figure 25(b), measured and calculated footprint shapes are in close agreement. It should be noted that the footprint outline looks distorted in figure 25(b) due to a difference in scaling factors between the two coordinates.

Tire contact load-intensity distributions. Figures 26–28 present comparisons of measured and predicted tire footprint load-intensity distributions. Data presented in the form of contour plots and measured load-intensity distributions shown in figures 15–17 are reproduced here to aid in the comparison. Boundary conditions used to produce the analytical results were chosen to simulate the misalignment in the loading fixture described earlier and arrows in figures 26–28 denote the direction, but not the magnitude, of tangential displacements that occurred during the normal loading sequence as a result of the misalignment. Part (a) of each figure presents results from the 2000-lbf normal load case, and part (b) of each figure presents results from the 15 000-lbf load case. All analytical results shown in figures 26–28 were obtained using model 1.

For the 2000-lbf normal load case the analysis predicts a ridge of high normal load intensities along both edges of the center circumferential tread groove. (See fig. 26(a).) The magnitude of normal load intensities along these ridges is between 900 psi and 1000 psi. Experimental measurements of the normal load-intensity distribution cannot confirm the existence of these high load-intensity ridges since no load transducers were located in the critical region along the edge of the center groove for this normal load condition. For the remainder of the footprint area the predicted magnitudes of normal load intensities are slightly less than the measured intensities, and the predicted distribution of normal load intensities is generally in fair agreement with experimental measurements. These results are consistent with analytical results for a tire tread presented in reference 39.

For the 15 000-lbf normal load case the analysis predicts ridges of high load intensities along each edge of the three circumferential tread grooves. Magnitudes associated with these ridges range between 500 psi and 800 psi, and are generally lower than the peak load intensities predicted for the 2000-lbf normal load case. Predicted and measured normal load-intensity distributions are in good agreement.

Figure 27 shows comparison of measured and predicted lateral friction load-intensity distributions. For the 2000-lbf normal load case (fig. 27(a)), both measured and predicted lateral friction load-intensity distributions exhibit loss in skew symmetry across the width of the footprint due to misalignment in the loading fixture. Measured and calculated lateral friction load-intensity distributions are in good agreement, and the magnitudes of the measured and predicted lateral friction load intensities are in fair agreement.

For the 15 000-lbf normal load case (fig. 27(b)), both predicted and measured lateral friction load intensities are shown to reach their maximum magnitudes in the lateral extremities of the tire footprint. This trend is more apparent for predicted results than for measured values. Both predicted lateral friction load intensities and measured results exhibit bands of alternating positive and negative friction values across the width of the tire footprint.

Figure 28 shows comparison of measured and predicted drag friction load-intensity distributions. For the 2000-lbf normal load case (fig. 28(a)) predicted drag friction load intensities are higher than the measured values. Experimental measurements and analytical predictions both indicate local maximums in the drag friction load intensities in the fore and aft sections of the tire footprint. However, the small negative drag friction load intensities seen in the experimental results are not present in the analytical predictions. Overall, the comparison between measured and predicted drag friction load-intensity distributions indicate that analytical predictions give a reasonable approximation of the drag friction distribution of the tire for static loading conditions, but

additional model fine-tuning efforts are needed to bring analytical and experimental drag friction load-intensity results into closer agreement.

For the 15 000-lbf normal load case (fig. 28(b)), both predicted and measured drag friction load-intensity distributions are shown to exhibit local positive and negative maximums in the fore and aft sections of the tire footprint and to exhibit minimum magnitudes near the center of the footprint. Predicted drag friction load-intensity magnitudes are generally higher than measured values. The analysis predicts the formation of larger pockets of negative drag friction load intensities in the leading edge of the footprint (the right edge of the footprint in fig. 28(b)) than the measurements indicate, but this trend is consistent with the experimental measurements obtained for the 30 000-lbf normal load case shown in figure 17(c).

Correlation between the analytical predictions and experimental measurements of tire footprint area, normal load-intensity distributions, and tangential load-intensity distributions appears to be stronger for the 15 000-lbf normal load case than for the 2000-lbf load case.

Influence of Model Refinement on Predicted Contact Load-Intensity Distributions

The contour plots in figure 29 show predicted contact load-intensity distributions for the Space Shuttle nose-gear tire subjected to an inflation pressure of 300 psi and unsymmetric static loading conditions associated with the experimental loading fixture misalignment. Load-intensity distribution predictions were made with model 1 and model 3 (figs. 19 and 20) for the 2000 lbf normal load case. Tangential displacement directions associated with the loading fixture misalignment are denoted by arrows in figure 29. Calculated contact area for each model is denoted by a dashed outline in each contour plot and there is no significant difference between the two calculated footprint shapes. Figure 29(a) shows calculated normal load-intensity distributions. The more refined model 3 and model 1 each predicted the existence of a ridge of high load intensities along both edges of the center tread groove for this loading case, but the predicted magnitudes of these load intensities from model 3 were about 200 psi lower than those predicted by model 1. This result is consistent with results presented in reference 38 for frictionless contact. Overall, the predicted normal load-intensity distribution from model 3 is smoother than the predicted distribution from model 1.

Figure 29(b) presents calculated lateral friction load-intensity distributions for model 1 and model 3. Generally, the predicted lateral friction load-intensity magnitudes from model 3 are larger than those from model 1 for the loading case considered. Both models predict a loss in lateral friction load-intensity skew symmetry due to the unsymmetric loading condition and this lack of symmetry is more pronounced for the model 1 predictions.

Figure 29(c) presents calculated drag friction load-intensity distributions for the models. Predicted drag friction load intensities from model 3 are consistently higher than those from model 1, and the model 3 drag friction load-intensity distribution is more uniform over the tire contact region than the predicted drag friction load-intensity distribution from model 1.

In summary, predicted contact load-intensity distributions for model 1 and model 3 are generally in close agreement. Model 3 softens the predicted peak normal load intensities along the edges of the center tread groove, but predicts larger friction load-intensity magnitudes than model 1. Predicted normal load-intensity distribution from model 3 is in closer agreement with the experimental measurements (see figs. 15–17 and figs. 26–28 for examples) than that from model 1, but predicted lateral friction and drag friction load-intensity distributions from model 1 are closer to the experimental measurements than those from model 3. Both models predict a shorter tire footprint length than the experimental measurement for the 2000-lbf normal load case.

Effect of Tread Grooves and Friction on Predicted Contact Load-Intensity Distributions

Figure 30 presents a comparison of predicted contact load-intensity distributions for a smooth-tread Space Shuttle nose-gear tire and a circumferentially-grooved tread Space Shuttle nose-gear tire subjected to a normal load of 2000 lbf. Analysis of both tread configurations was conducted with model 1, and for these results, tire normal loading was assumed to be symmetric with no tangential displacements associated with load fixture misalignments. Figure 30(a) shows normal load-intensity distributions. Smooth-tread tire results indicate peak normal load intensities between 300 psi and 400 psi near the center of contact. When the smooth tread is replaced with a circumferentially-grooved tread, two ridges of high normal load intensities are observed along the edges of the center groove. Magnitude of normal load intensities along these ridges is between 900 psi and 1000 psi. It should be noted that normal load-intensity distribution for the symmetrically-loaded grooved-tread tire is nearly identical to the predicted normal load-intensity distribution shown in figure 26(a) for the unsymmetrically loaded tire. The presence of the circumferential tread grooves also affects the predicted footprint shape. The grooved-tread footprint is slightly longer and thinner than the smooth-tread footprint.

Figure 30(b) shows comparison of the lateral friction load-intensity distributions for the grooved- and smooth-tread tire and figure 30(c) shows the drag friction load-intensity distribution comparison. Lateral friction load intensities for both tread configurations exhibit skew symmetric distributions across the width of the tire footprint and the presence of the center circumferential groove does not have a significant effect on the lateral friction load-intensity distribution. Insensitivity of the lateral friction load-intensity distribution to the presence of a center groove is attributed to the natural distribution of lateral friction load intensities which concentrate these friction forces in the lateral extremities of the footprint. Predicted drag friction load intensities for this symmetric loading condition are uniformly small over the entire footprint and should be compared with the predicted drag friction load intensities for the unsymmetric loading case. (See fig. 28(a).)

In summary, a comparison of the predicted load-intensity distributions presented in figure 30 with those presented in figures 26–28 indicates that predicted normal load-intensity distributions are strongly influenced by the presence of tread grooves and generally unaffected by unsymmetric loading conditions associated with the loading fixture misalignments. Conversely, lateral friction and drag friction load-intensity distributions were unaffected by the presence of tread grooves for the loading conditions examined, but were very sensitive to tangential displacements associated with the misalignment in the loading fixture.

Figure 31 presents a comparison of predicted normal load intensities for frictional and frictionless contact of a grooved-tread Space Shuttle nose-gear tire. Both analyses were conducted with model 1. The comparison presented in figure 31 indicates that the normal load-intensity distribution for symmetric static loading cases is unaffected by the presence of friction forces. This result implies that a reasonable modeling strategy for tires subjected to static loading contact conditions might involve operator splitting techniques to first apply the normal load with a frictionless contact assumption and then apply subsequent tangential loads with a contact-friction algorithm.

Strain Energy Density Distributions

One method of showing the regions of high strain due to the imposed loads on a complex structure such as a tire is strain energy density. Calculated variations in the strain energy density for the Space Shuttle nose-gear tire are presented in figure 32 in the form of contour plots. Results are shown for normal loading cases of 2000 lbf and 15 000 lbf. Figure 32(a) presents total strain energy density and figure 32(b) presents transverse-shear strain energy density. For the load cases shown, the total strain energy density is primarily influenced by the inflation pressure load. Since the normal loads associated with contact are compressive, the total strain energy density is reduced in the region of contact. Total strain energy density is also reduced in the lower tire sidewall near the bead. Transverse-shear strain energy density is maximized in the tire sidewall near the contact zone and along the lower sidewall near the bead. In the upper sidewall and shoulder of the tire near the contact region (see fig. 32(b) insert) the transverse-shear strain energy represents about 25 percent to 50 percent of the total strain energy associated with static contact.

Conclusions

A computational procedure is presented for the solution of frictional contact problems for aircraft tires. The Space Shuttle nose-gear tire is modeled using a two-dimensional laminated anisotropic shell theory with the effects of variations in material and geometric parameters, transverse-shear deformation, and geometric nonlinearities included.

Experimental results are presented that describe the response of the Space Shuttle nose-gear tire to inflation-pressure loads and to combined inflation-pressure loads and normal static loads against a rigid flat plate. These experimental results describe the meridional growth of the tire cross section due to inflation loading, the static load-deflection characteristics of the tire, the geometry of the tire footprint under static loading conditions, and the normal and tangential load-intensity distributions in the tire footprint for the various static vertical-loading conditions.

Numerical results are presented for the Space Shuttle nose-gear tire subjected to inflation-pressure loads and combined inflation-pressure and contact loads against a rigid flat plate.

Results from this investigation lead to the following observations and conclusions:

1. The predicted inflated profile is in excellent agreement with measured profiles from the photogrammetry studies. Predicted normal and tangential contact load-intensity distributions are in fair to good agreement with experimental measurements, though additional experimental and analytical studies are needed. Correlation between analytical predictions and experimental measurements of tire footprint area, normal load-intensity distributions, and tangential load-intensity distributions appears to be stronger for the 15 000-lbf normal load case than for the 2000-lbf load case.

2. Predicted normal load-intensity distribution from the model with a refined grid in the tire contact area is in closer agreement with the experimental measurements than the distribution from the least refined model used in this investigation, but predicted lateral friction and drag friction load-intensity distributions from that least refined model are closer to the experimental measurements than those from the refined model.

3. Predicted normal load-intensity distributions are strongly influenced by the presence of tread grooves and generally unaffected by unsymmetric loading conditions associated with the loading fixture misalignments. Lateral friction and drag friction load-intensity distributions are unaffected by the presence of tread grooves for the loading conditions examined, but are very sensitive to tangential displacements associated with the misalignment in the loading fixture.

4. Normal load-intensity distributions for symmetric static loading cases are unaffected by the presence of friction forces. This result implies that a reasonable modeling strategy for tires subjected to static-loading contact conditions might involve operator splitting techniques to first apply the normal load with a frictionless contact assumption and then apply subsequent tangential loads with a contact-friction algorithm.

5. In the upper sidewall and shoulder of the tire near the contact region the transverse-shear strain energy represents about 25 percent to 50 percent of the total strain energy associated with static contact.

NASA Langley Research Center
Hampton, VA 23681-0001
February 6, 1996

Appendix

Fundamental Equations of Shell Theory Used in Present Study

This appendix summarizes the fundamental equations of the Sanders-Budiansky type shell of revolution used in this study. Effects of laminated, anisotropic material response and transverse-shear deformation are included in these relationships.

Strain-Displacement Relationships

$$\varepsilon_s = \partial_s u + \frac{w}{R_1} + \underline{\frac{1}{2}\left(\frac{u}{R_1} - \partial_s w\right)^2} + \frac{1}{2}\phi^2 \tag{A1}$$

$$\varepsilon_\theta = \frac{\partial_s r}{r} u + \frac{1}{r}\partial_\theta v + \frac{w}{R_2} + \underline{\frac{1}{2}\left(\frac{v}{R_2} - \frac{1}{r}\partial_\theta w\right)^2} + \frac{1}{2}\phi^2 \tag{A2}$$

$$2\varepsilon_{s\theta} = \frac{1}{r}\partial_\theta u + \left(\partial_s - \frac{\partial_s r}{r}\right)v + \underline{\left(\frac{u}{R_1} - \partial_s w\right)\left(\frac{v}{R_2} - \frac{1}{r}\partial_\theta w\right)} \tag{A3}$$

$$\kappa_s = \partial_s \phi_s \tag{A4}$$

$$\kappa_\theta = \frac{\partial_s r}{r}\phi_s + \frac{1}{r}\partial_\theta \phi_\theta \tag{A5}$$

$$2\kappa_{s\theta} = \frac{1}{r}\partial_\theta \phi_s + \left(\partial_s - \frac{\partial_s r}{r}\right)\phi_\theta + \left(\frac{1}{R_2} - \frac{1}{R_1}\right)\phi \tag{A6}$$

$$2\varepsilon_{s3} = -\frac{u}{R_1} + \partial_s w + \phi_s \tag{A7}$$

$$2\varepsilon_{\theta 3} = -\frac{v}{R_2} + \frac{1}{r}\partial_\theta w + \phi_\theta \tag{A8}$$

where ε_s and ε_θ are extensional strains in the meridional and circumferential directions, $2\varepsilon_{s\theta}$ is the in-plane shear strain, κ_s and κ_θ are bending strains in the meridional and circumferential directions, $2\kappa_{s\theta}$ is the twisting strain, $2\varepsilon_{s3}$ and $2\varepsilon_{\theta 3}$ are transverse-shear strains, $\partial_s \equiv \frac{\partial}{\partial_s}$, $\partial_\theta \equiv \frac{\partial}{\partial_\theta}$, and ϕ is the rotation around the normal to the shell, which is given by

$$\phi = \left[-\frac{1}{r}\partial_\theta u + \left(\partial_s + \frac{\partial_s r}{r}\right)v\right] \tag{A9}$$

Nonlinear terms that account for moderate rotations are underlined with dashes in equations (A1) –(A3).

Constitutive Relations

The shell is assumed to be made of a laminated, anisotropic, linearly elastic material. Every point of the shell is assumed to possess a single plane of elastic symmetry parallel to the middle surface. The relationships between the stress resultants and the strain measures of the shell are given by

$$\begin{Bmatrix} N_s \\ N_\theta \\ N_{s\theta} \\ \hdashline M_s \\ M_\theta \\ M_{s\theta} \\ \hdashline Q_s \\ Q_\theta \end{Bmatrix} = \left[\begin{array}{ccc:ccc:cc} c_{11} & c_{12} & \textcircled{c_{16}} & f_{11} & f_{12} & \textcircled{f_{16}} & \bullet & \bullet \\ & c_{22} & \textcircled{c_{26}} & f_{12} & f_{22} & \textcircled{f_{26}} & \bullet & \bullet \\ & & c_{66} & \textcircled{f_{16}} & \textcircled{f_{26}} & f_{66} & \bullet & \bullet \\ \hdashline & & & d_{11} & d_{12} & \textcircled{d_{16}} & \bullet & \bullet \\ & & & & d_{22} & \textcircled{d_{26}} & \bullet & \bullet \\ & \text{Symmetric} & & & & d_{66} & \bullet & \bullet \\ \hdashline & & & & & & c_{55} & \textcircled{c_{45}} \\ & & & & & & & c_{44} \end{array}\right] \begin{Bmatrix} \varepsilon_s \\ \varepsilon_\theta \\ 2\varepsilon_{s\theta} \\ \hdashline \kappa_s \\ \kappa_\theta \\ 2\kappa_{s\theta} \\ \hdashline 2\varepsilon_{s3} \\ 2\varepsilon_{\theta 3} \end{Bmatrix} \tag{A10}$$

where c_{ij}, f_{ij}, and d_{ij} (i, j = 1, 2, 6) are shell stiffness coefficients. Nonorthotropic (anisotropic) terms are circled and dots indicate zero terms.

References

1. Zhong, Zhi-Hua; and Mackerle, Jaroslav: Static Contact Problems—A Review. *Eng. Comput*., vol. 9, Feb. 1992, pp. 3–37.
2. Tanner, J. A.: *Static and Yawed-Rolling Mechanical Properties of Two Type VII Aircraft Tires*. NASA TP-1863, 1981.
3. Stubbs, Sandy M.; Tanner, John A.; and Smith, Eunice G.: *Behavior of Aircraft Antiskid Braking Systems on Dry and Wet Runway Surfaces—A Slip-Velocity-Controlled, Pressure-Bias-Modulated System*. NASA TP-1051, 1978.
4. Tanner, John A.; Dreher, Robert C.; Stubbs, Sandy M.; and Smith, Eunice G.: *Tire Tread Temperatures During Antiskid Braking and Cornering on a Dry Runway.* NASA TP-2009, 1982.
5. Daugherty, Robert H.; and Stubbs, Sandy M.: *Cornering and Wear Behavior of the Space Shuttle Orbiter Main Gear Tire*. SAE Paper 871867, Oct. 1987.
6. Daugherty, Robert H.; and Stubbs, Sandy M.: *Spin-Up Studies of the Space Shuttle Orbiter Main Gear Tire*. SAE Paper 881360, Oct. 1988.
7. Oden, J. T.; and Martins, J. A. C.: Models and Computational Methods for Dynamic Friction Phenomena. *Comput. Methods Appl. Mech. & Eng*., vol. 52, nos. 1–3, Sept. 1985, pp. 527–634.
8. Clark, Samuel K.; and Dodge, Richard N.: *Heat Generation in Aircraft Tires Under Free Rolling Conditions.* NASA CR-3629, 1982.
9. Clark, Samuel K.; and Dodge, Richard N.: *Heat Generation in Aircraft Tires Under Braked Rolling Conditions*. NASA CR-3768, 1984.
10. McCarty, John L.: *Temperature Distribution in an Aircraft Tire at Low Ground Speeds*. NASA TP-2195, 1983.
11. Schaeffer, H. G.; and Ball, R. E.: Nonlinear Deflections of Asymmetrically Loaded Shells of Revolution. AIAA-68-292, Apr. 1968.
12. Wunderlich, W.; Cramer, H.; and Obrecht, H.: Application of Ring Elements in the Nonlinear Analysis of Shells of Revolution Under Nonaxisymmetric Loading. *Comput. Methods Appl. Mech. & Eng.*, vol. 51, Sept. 1985, pp. 259–275.
13. Noor, A. K.: On Making Large Nonlinear Problems Small. *Comput. Methods Appl. Mech. & Eng.*, vol. 34, nos. 1–3, Sept. 1982, pp. 955–985.
14. Noor, Ahmed K.; Andersen, Carl M.; and Tanner, John A.: *Mixed Models and Reduction Techniques for Large-Rotation, Nonlinear Analysis of Shells of Revolution With Application to Tires*. NASA TP-2343, 1984.
15. Noor, Ahmed K.: Reduction Method for the Non-Linear Analysis of Symmetric Anisotropic Panels. *Int. J. Numer. Methods Eng.*, vol. 23, July 1986, pp. 1329–1341.
16. Noor, Ahmed K.; and Peters, Jeanne M.: Nonlinear Analysis of Anisotropic Panels. *AIAA J*., vol. 24, Sept. 1986, pp. 1545–1553.
17. Noor, Ahmed K.; Andersen, Carl M.; and Tanner, John A.: *Exploiting Symmetries in the Modeling and Analysis of Tires*. NASA TP-2649, 1987.
18. Noor, Ahmed K.; and Tanner, John A.: *Advances in Contact Algorithms and Their Application to Tires*. NASA TP-2781, 1988.
19. Sanders, J. L., Jr.: Nonlinear Theories for Thin Shells. *Q. Appl. Math.*, vol. 21, no. 1, Apr. 1963, pp. 21–36.
20. Budiansky, Bernard: Notes on Nonlinear Shell Theory. *J. Appl. Mech.*, vol. 35, no. 2, June 1968, pp. 393–401.
21. Simo, Juan C.; Wriggers, Peter; and Taylor, Robert L.: A Perturbed Lagrangian Formulation for the Finite Element Solution of Contact Problems. *Comput. Methods Appl. Mech. & Eng*., vol. 50, no. 2, Aug. 1985, pp. 163–180.
22. Stein, E.; Wagner, W.; and Wriggers, P.: Finite Element Postbuckling Analysis of Shells With Nonlinear Contact Restraints. *Finite Element Methods for Nonlinear Problems*. P. G. Bergan, K. J. Bathe, and W. Wunderlich, eds., Springer-Verlag, 1986, pp. 719–744.
23. Wriggers, Peter; and Nour-Omid, Bahram: *Solution Methods for Contact Problems*. Rep. No. UCB/SESM-84/09 (Contract N00014-76-C-0013), Dep. of Civil Engineering, Univ. of California, July 1984.
24. Concus, Paul; Golub, Gene H.; and O'Leary, Dianne P.: A Generalized Conjugate Gradient Method for the Numerical Solution of Elliptic Partial Differential Equations. *Sparse Matrix Computations*. James R. Bunch and Donald J. Rose, eds., Academic Press Inc., 1976, pp. 309–332.
25. Adams, Loyce: M-Step Preconditioned Conjugate Gradient Methods. *SIAM J. Sci. & Stat. Comput*., vol. 6, no. 2, Apr. 1985, pp. 452–463.
26. Tanner, J. A.; Martinson, V. J.; and Robinson, M. P.: Static Frictional Contact of the Space Shuttle Nose Gear Tire. *Tire Sci. & Tech.*, TSTCA, vol. 22, no. 4, Oct.–Dec. 1994, pp. 242–272.
27. Tanner, John A.: *Computational Methods for Frictional Contact With Applications to the Space Shuttle Orbiter Nose-Gear Tire—Development of Frictional Contact Algorithm*. NASA TP-3574, 1996.
28. *User's Manual—ISML Math/Library, Version 1.1*, MALB-USM-PERFCT-EN8901-1.1, IMSL, Inc., Jan. 1989.
29. Cline, Alan Kaylor: *Fitpack—A Software Package for Curve and Surface Fitting Employing Splines Under Tension.* Pleasant Valley Software, 1985.
30. De Boor, Carl: *A Practical Guide to Splines*. Springer-Verlag, 1978.
31. Reinsch, Christian H.: Smoothing by Spline Functions. *Numer. Math.*, vol. 10, no. 3, 1967, pp. 177–183.
32. Cline, A. K.: Scalar- and Planar-Valued Curve Fitting Using Splines Under Tension. *Commun. ACM*, vol. 17, no. 4, Apr. 1974, pp. 218–220.

33. Jones, Robert M.: *Mechanics of Composite Materials*. McGraw-Hill Book Co., 1975.

34. Walter, J. D.: Cord Reinforced Rubber. *Mechanics of Pneumatic Tires*, Samuel K. Clark, ed., U.S. Dep. of Transportation, 1981, pp. 123–202.

35. Karara, H. M., ed.: *Non-Topographic Photogrammetry*, Second ed. American Soc. for Photogrammetry and Remote Sensing, 1989.

36. Schroeder, Lyle C.; Adams, Richard C.; Bailey, M. C.; Belvin, W. Keith; Butler, David H.; and Campbell, Thomas G.: *Near-Field Testing of the 15-Meter Hoop-Column Antenna*. NASA TM-4073, 1989.

37. Howell, William E.; Tanner, Sharon E.; and Vogler, William A.: *Static Footprint Local Forces, Areas, and Aspect Ratios for Three Type VII Aircraft Tires*. NASA TP-2983, 1991.

38. Kim, Kyun O.; Noor, Ahmed K.; and Tanner, John A.: *Modeling and Analysis of the Space Shuttle Nose-Gear Tire With Semianalytic Finite Elements*. NASA TP-2977, 1990.

39. Gall, R.; Tkacik, P.; and Andrews, M.: On the Incorporation of Frictional Effects in the Tire/Ground Contact Area. *Tire Sci. and Tech.*, vol. 21, no. 1, Jan.–Mar. 1993, pp. 2–22.

Table 1. Variation of Ply Thickness h_k/h_0

[h_0 = 0.7513 in.]

Ply number (top to bottom)	h_k/h_0 for region—						
	I	II	III	IV	V	VI	VII
1 (tread and sidewall)	$h_1 = h - \sum_{k=2}^{16} h_k$						
[a]2	0.0865–.0865	0.0865–.0658	0.0658–.0692	0.0692–.0813	0.0801–.0937	0.0681–.1238	0.0918–.1240
3	0.0865–.0865	0.0865–.0658	0.0658–.0692	0.0692–.0813	0.0801–.0937	0.0681–.1238	0.0918–.1240
4	0.0865–.0865	0.0666–.0506	0.0506–.0532	0.0692–.0813	0.0488–.0571	0.0523–.0950	0.0652–.0880
5	0.0666–.0666	0.0666–.0506	0.0506–.0532	0.0426–.0500	0.0488–.0571	0.0523–.0950	0.0652–.0880
6	0.0666–.0666	0.0666–.0506	0.0506–.0532	0.0426–.0500	0.0488–.0571	0.0523–.0950	[b]0.2662–.3594
7	0.0666–.0666	0.0666–.0506	0.0506–.0532	0.0426–.0500	0.0488–.0571	0.0523–.0950	0.0652–.0880
8	0.0666–.0666	0.0666–.0506	0.0506–.0532	0.0426–.0500	0.0488–.0571	0.0523–.0950	0.0652–.0880
9	0.0666–.0666	0.0666–.0506	0.0506–.0532	0.0426–.0500	0.0488–.0571	0.0523–.0950	0.0652–.0880
10	0.0666–.0666	0.0466–.0354	0.0354–.0373	0.0426–.0500	0.0488–.0571	0.0523–.0950	0.0652–.0880
11	0.0466–.0466	0.0466–.0354	0.0354–.0373	0.0346–.0407	0.0488–.0571	0.0523–.0950	[b]0.2662–.3594
12	0.0466–.0466	0.0798–.0798	0.0798–.0798	0.0346–.0407	0.0375–.0439	0.0523–.0950	0.0652–.0880
13	0.0798–.0798	0	0	0.0798–.0798	0.0375–.0439	0.0523–.0950	0.0652–.0880
14	0	0	0	0	0.0798–.0798	0.0366–.0666	0.0466–.0629
15	0	0	0	0	0	0.0366–.0666	0.0466–.0629
16	0	0	0	0	0	0.0798–.1464	0.1464–.1597

[a]Second layer of region I represents layer which has reinforcement (see fig. 2).

[b]Represents thickness of bead wires.

Table 2. Values of Elastic Constants of Tire Constituents Used in Present Study

Tire constituent	Young's modulus, psi	Shear modulus, psi	Poisson's ratio
Rubber	4.5×10^2	1.51×10^2	0.49
Nylon cord	3.5×10^5	7.00×10^2	.66
Bead[a]	2.9×10^7	1.10×10^7	.30

[a]Since deformations are small in bead area, it is reasonable to assume that bead wires are isotropic.

Table 3. Variation of Nylon Cord End Counts in Different Plies Along Meridian

Ply number (top to bottom)	Cord end count, ends per inch, for region—						
	I	II	III	IV	V	VI	VII
1 (tread and sidewall)	Rubber	Rubber	Rubber	Rubber	Rubber	Rubber	Rubber
2	16–16	18–14	14–14	14–14	14–14	14–14	14–14
3	18–18	18–14	14–14	14–14	14–14	14–14	14–14
4	18–18	21–20	20–18	18–16	16–16	16–14	14–14
5	23–21	21–20	20–18	18–16	16–16	16–14	14–14
6	23–21	21–20	20–18	18–16	16–16	16–14	Bead
7–9	23–21	21–20	20–18	18–16	16–16	16–14	14–14
10	23–21	29–26	26–25	18–16	16–16	16–14	14–14
11	30–29	29–26	26–25	25–24	16–16	16–14	Bead
12	30–29	Rubber	Rubber	25–24	24–22	16–14	14–14
13	Rubber			Rubber	24–22	16–14	14–14
14					Rubber	22–22	22–22
15						22–22	22–22
16						Rubber	Rubber

Table 4. Variation of Cord Orientation of Individual Plies, $\tilde{\theta}_k$, Along Meridian

Ply number (top to bottom)	$\tilde{\theta}_k$, deg, for region—						
	I	II	III	IV	V	VI	VII
1	Rubber	Rubber	Rubber	Rubber	Rubber	Rubber	Rubber
2	$-\tilde{\theta}-6$	$\tilde{\theta}$	$\tilde{\theta}$	$\tilde{\theta}$	$\tilde{\theta}$	$\tilde{\theta}$	$\tilde{\theta}$
3	$\tilde{\theta}$	$-\tilde{\theta}$	$-\tilde{\theta}$	$-\tilde{\theta}$	$-\tilde{\theta}$	$-\tilde{\theta}$	$-\tilde{\theta}$
4	$-\tilde{\theta}$	$\tilde{\theta}$	$\tilde{\theta}$	$-\tilde{\theta}$	$-\tilde{\theta}$	$-\tilde{\theta}$	$\tilde{\theta}$
5	$\tilde{\theta}$	$-\tilde{\theta}$	$-\tilde{\theta}$	$\tilde{\theta}$	$\tilde{\theta}$	$\tilde{\theta}$	$-\tilde{\theta}$
6	$-\tilde{\theta}$	$\tilde{\theta}$	$\tilde{\theta}$	$-\tilde{\theta}$	$\tilde{\theta}$	$-\tilde{\theta}$	Bead
7	$\tilde{\theta}$	$-\tilde{\theta}$	$-\tilde{\theta}$	$\tilde{\theta}$	$-\tilde{\theta}$	$\tilde{\theta}$	$-\tilde{\theta}$
8	$-\tilde{\theta}$	$\tilde{\theta}$	$\tilde{\theta}$	$-\tilde{\theta}$	$\tilde{\theta}$	$-\tilde{\theta}$	$\tilde{\theta}$
9	$\tilde{\theta}$	$-\tilde{\theta}$	$-\tilde{\theta}$	$\tilde{\theta}$	$-\tilde{\theta}$	$\tilde{\theta}$	$-\tilde{\theta}$
10	$-\tilde{\theta}$	$\tilde{\theta}+6$	$\tilde{\theta}+6$	$-\tilde{\theta}$	$\tilde{\theta}$	$-\tilde{\theta}$	$\tilde{\theta}$
11	$\tilde{\theta}+6$	$-\tilde{\theta}-6$	$-\tilde{\theta}-6$	$\tilde{\theta}+6$	$-\tilde{\theta}$	$\tilde{\theta}$	Bead
12	$-\tilde{\theta}-6$	Rubber	Rubber	$-\tilde{\theta}-6$	$\tilde{\theta}+6$	$\tilde{\theta}$	$\tilde{\theta}$
13	Rubber			Rubber	$-\tilde{\theta}-6$	$-\tilde{\theta}$	$-\tilde{\theta}$
14					Rubber	$\tilde{\theta}+6$	$\tilde{\theta}+6$
15						$-\tilde{\theta}-6$	$-\tilde{\theta}-6$
16						Rubber	Rubber

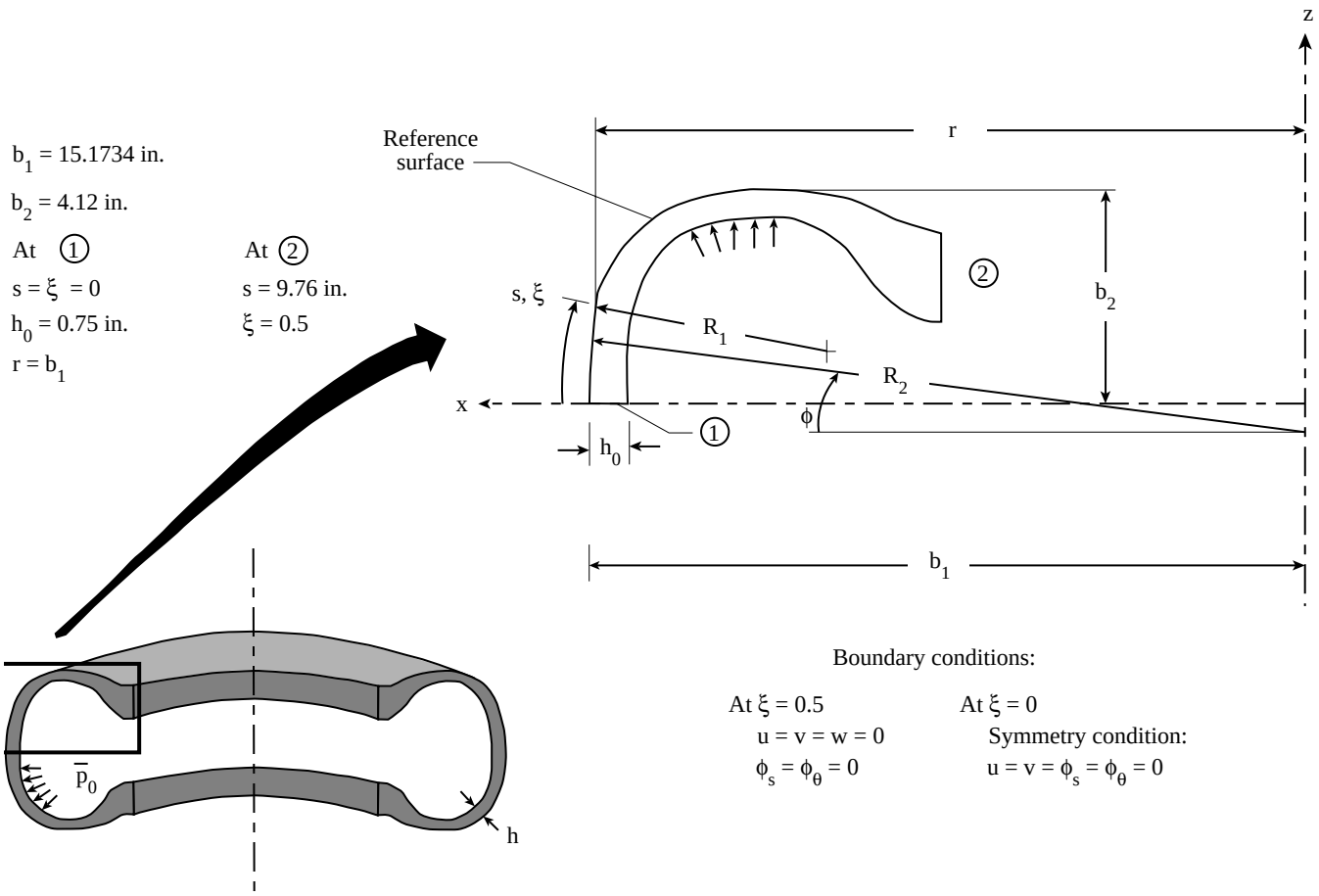

Figure 1. Geometric characteristics of Space Shuttle nose-gear tire.

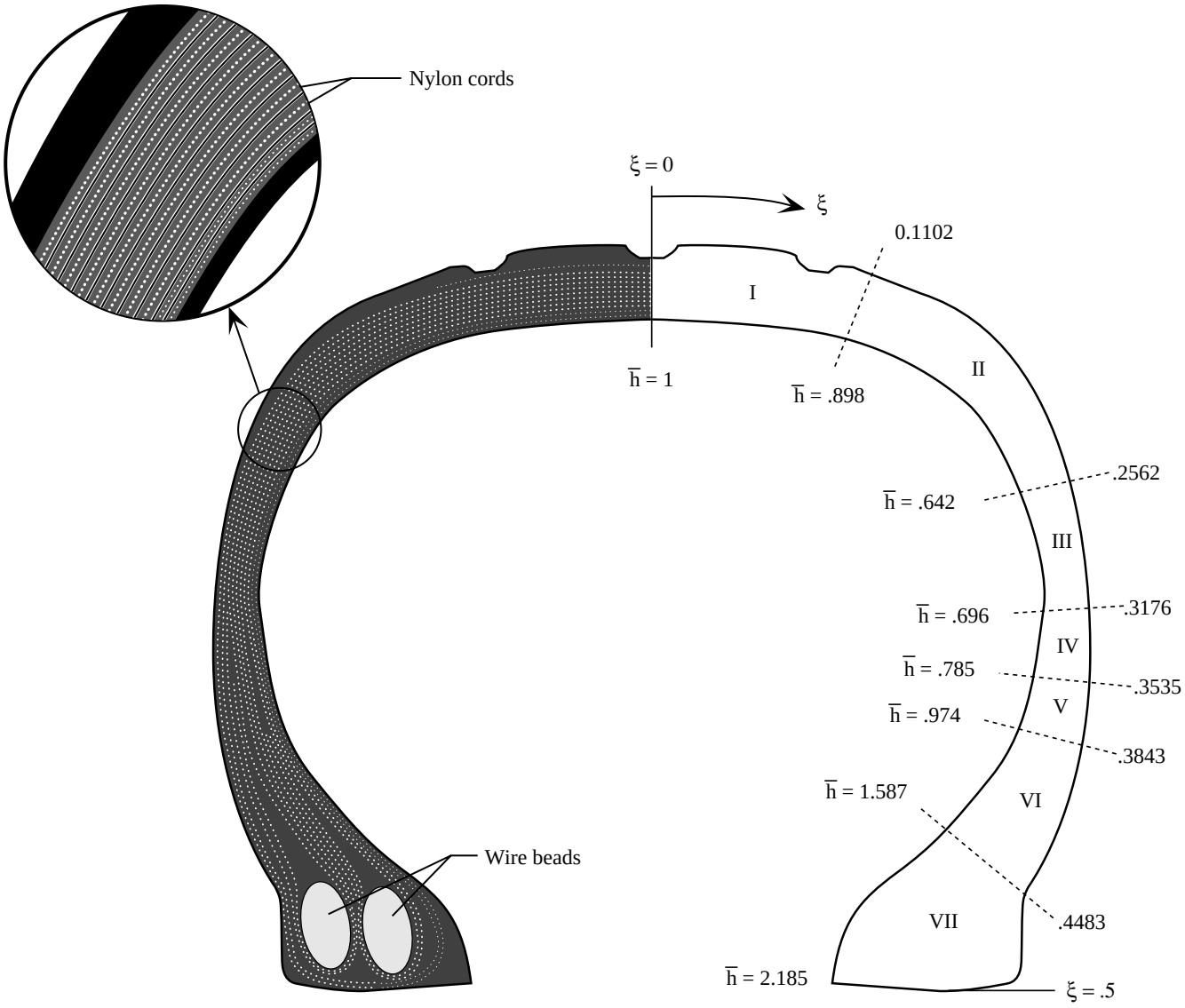

Figure 2. Cross section of Space Shuttle nose-gear tire showing seven model regions.

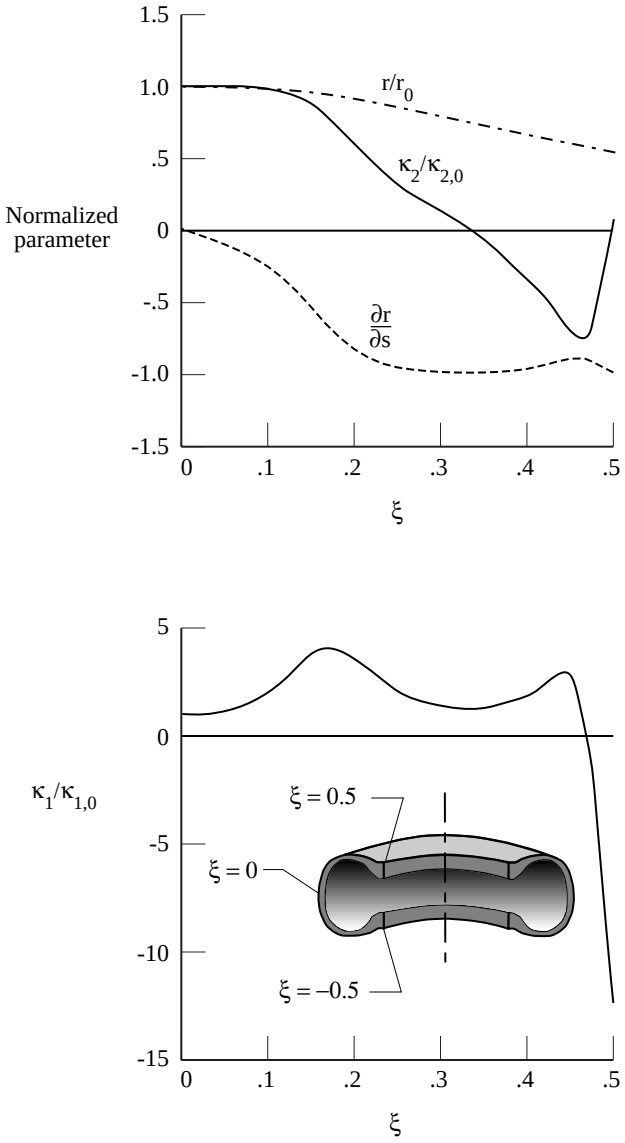

Figure 3. Meridional variation of geometric parameters of two-dimensional shell model of Space Shuttle nose-gear tire. Reference surface chosen to be outer surface. r_0 = 15.1737 in.; $\kappa_{2,0}$ = 0.0659 in^{-1}; $\kappa_{1,0}$ = 0.1091 in^{-1}.

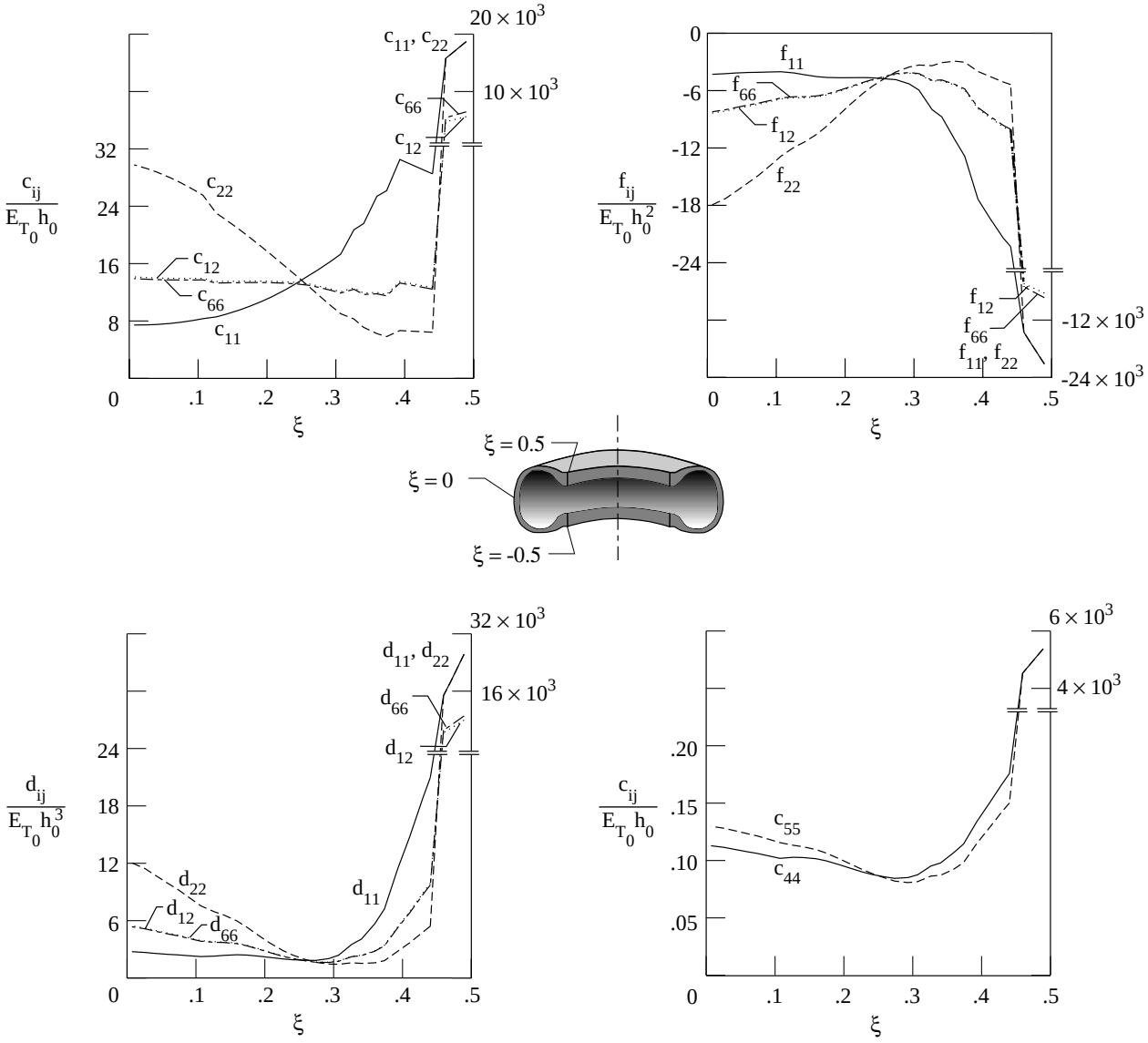

(a) Stiffness coefficients associated with uncoupled (orthotropic) response.

Figure 4. Meridional variation of stiffness coefficients of two-dimensional shell model of Space Shuttle nose-gear tire. E_{T_0} = 1160.3 psi; h_0 = 0.7513 in.

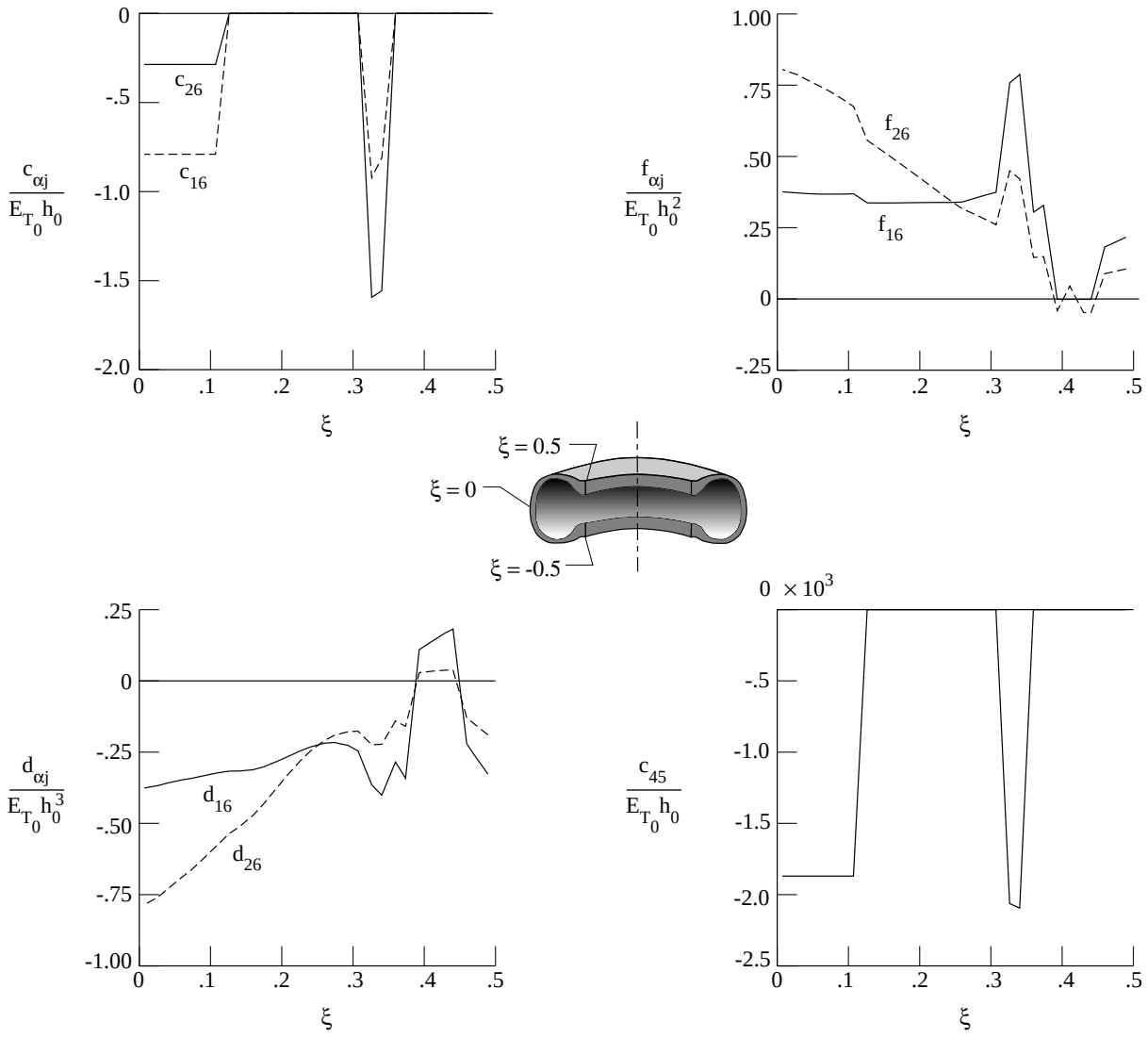

(b) Coupling (nonorthotropic) stiffness coefficients. $\alpha = 1,2$.

Figure 4. Concluded.

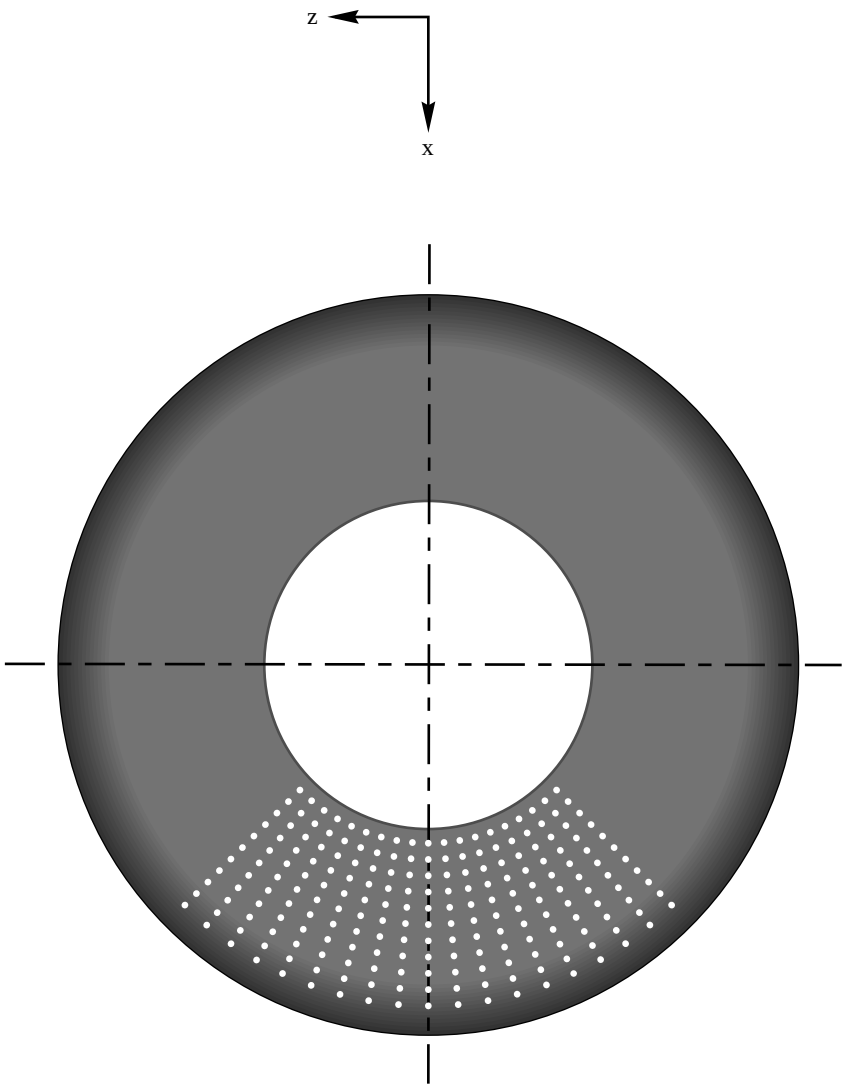

Figure 5. Arrangement of photogrammetry targets on Space Shuttle nose-gear tire.

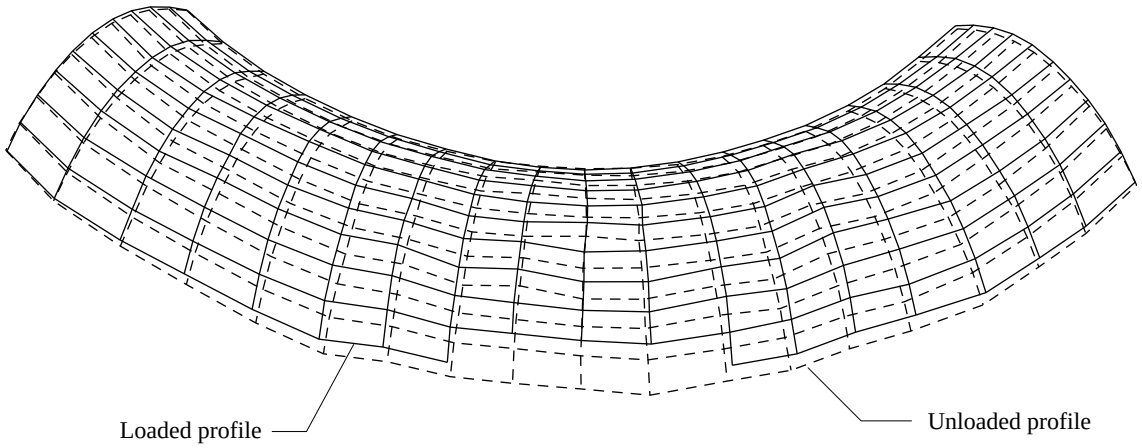

Figure 6. Unloaded and loaded sidewall profiles for Space Shuttle nose-gear tire.

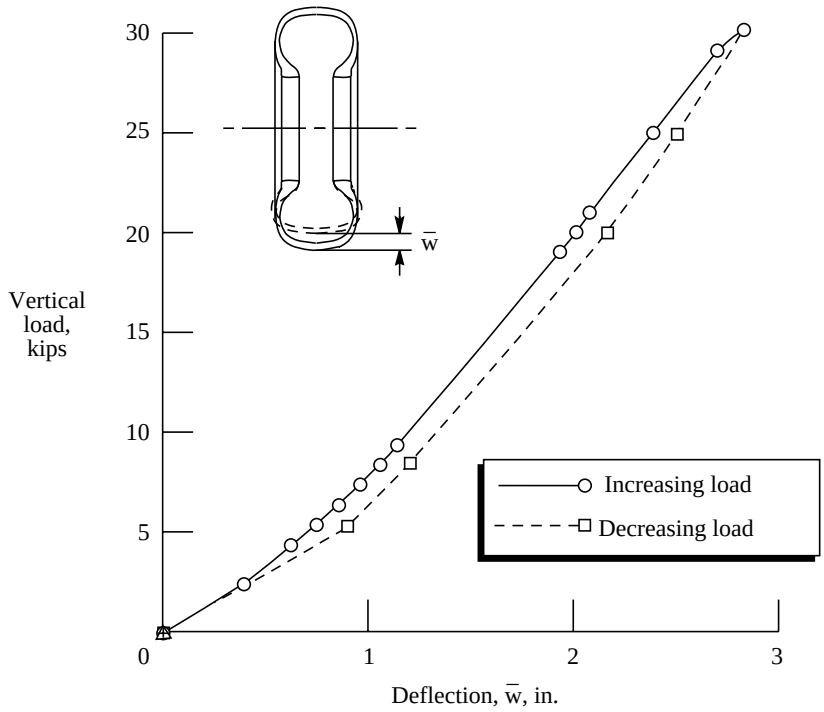

Figure 7. Static vertical load-deflection curve for Space Shuttle nose-gear tire.

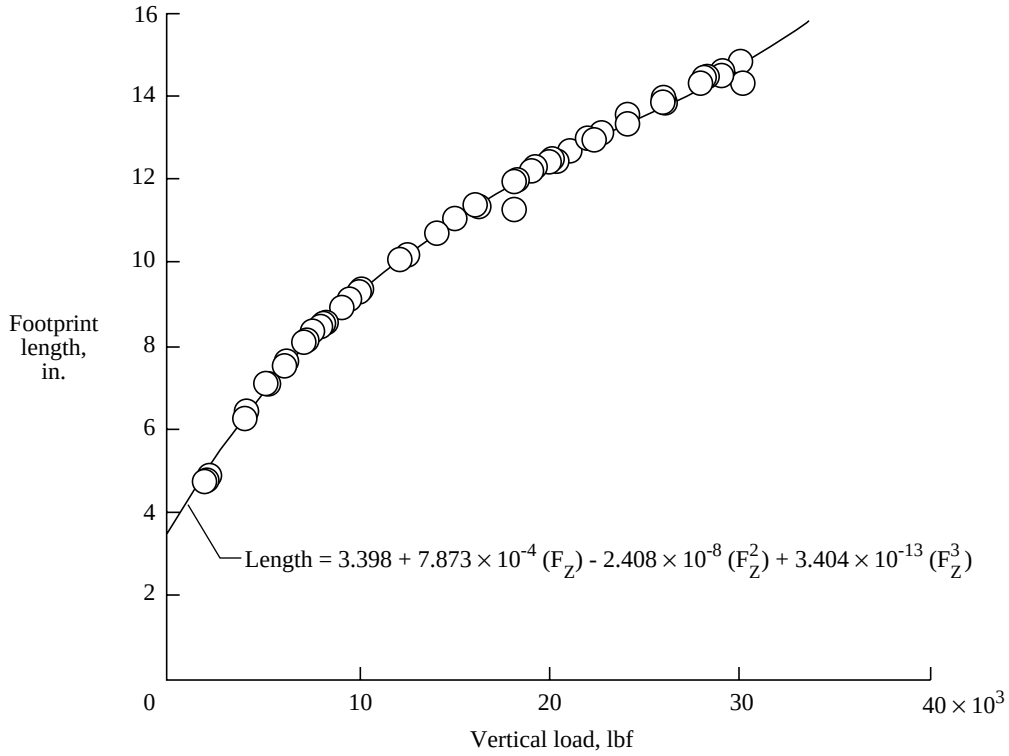

Figure 8. Footprint length as a function of vertical load for Space Shuttle nose-gear tire. Inflation pressure = 300 psi.

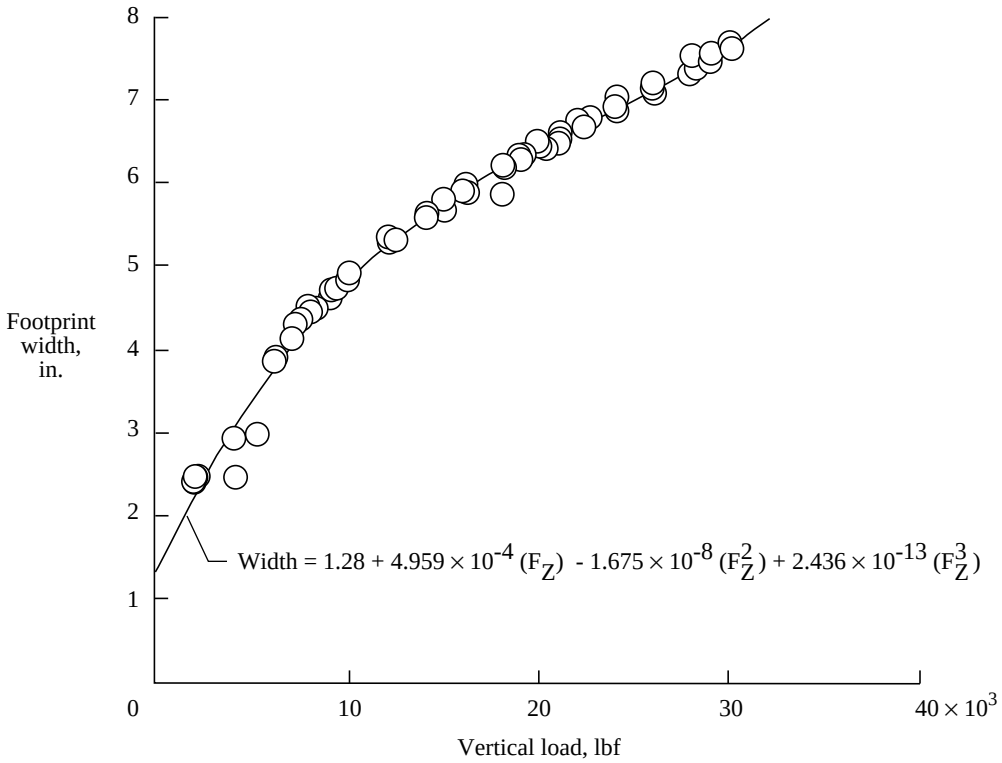

Figure 9. Footprint width as a function of vertical load for Space Shuttle nose-gear tire. Inflation pressure = 300 psi.

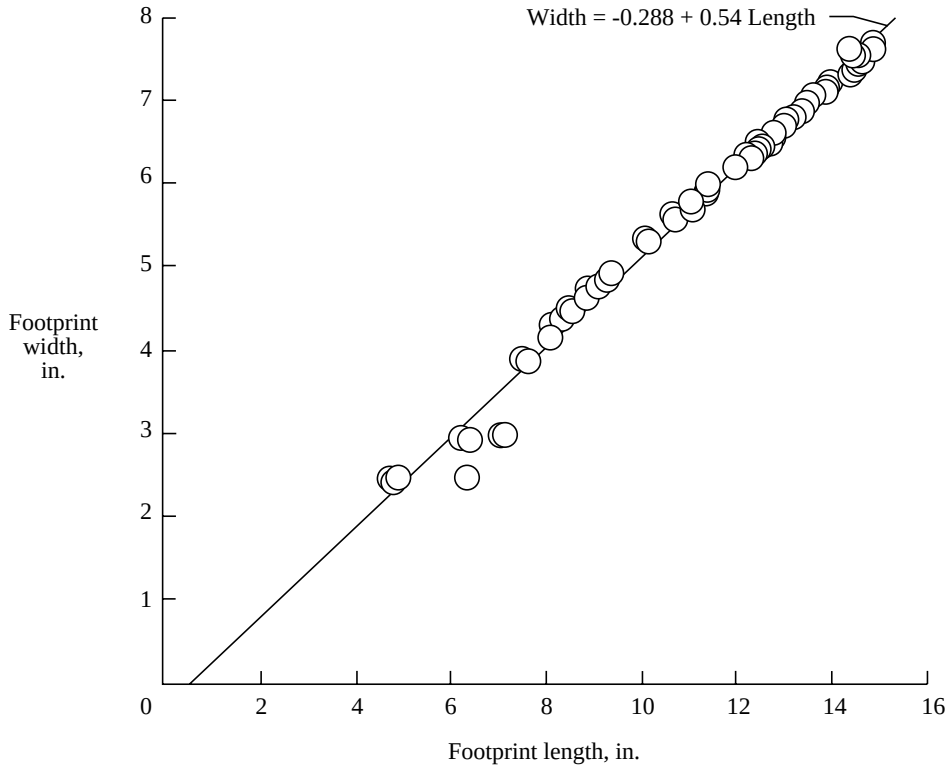

Figure 10. Footprint width as a function of footprint length for Space Shuttle nose-gear tire. Inflation pressure = 300 psi.

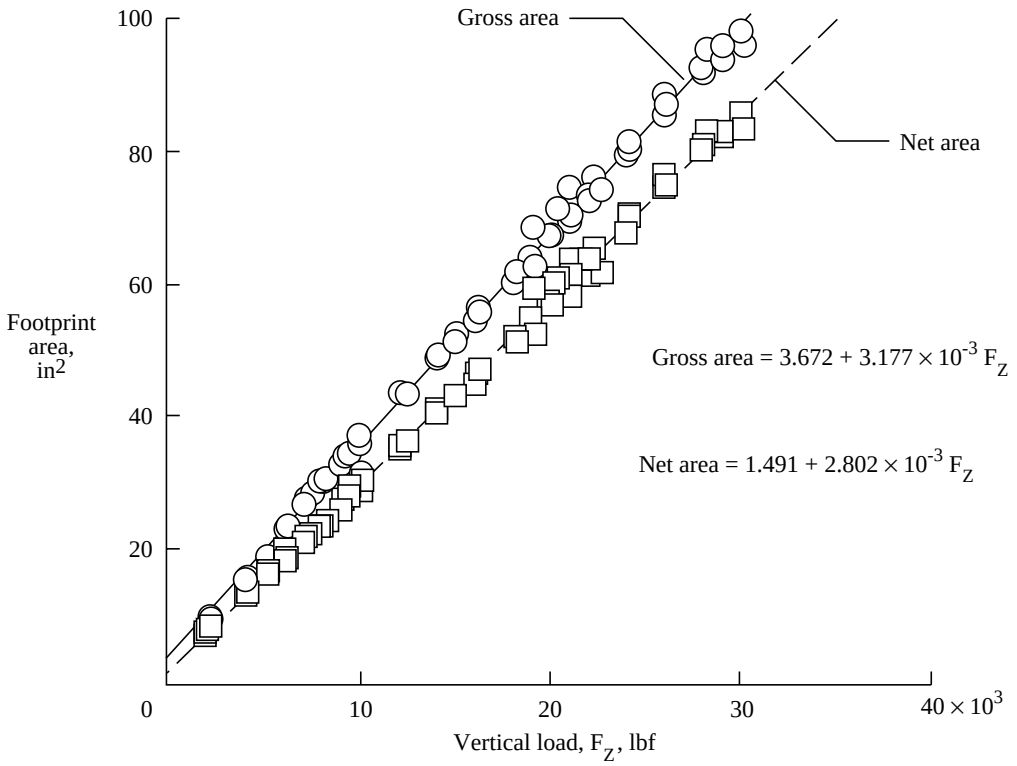

Figure 11. Footprint area as a function of vertical load for Space Shuttle nose-gear tire. Inflation pressure = 300 psi.

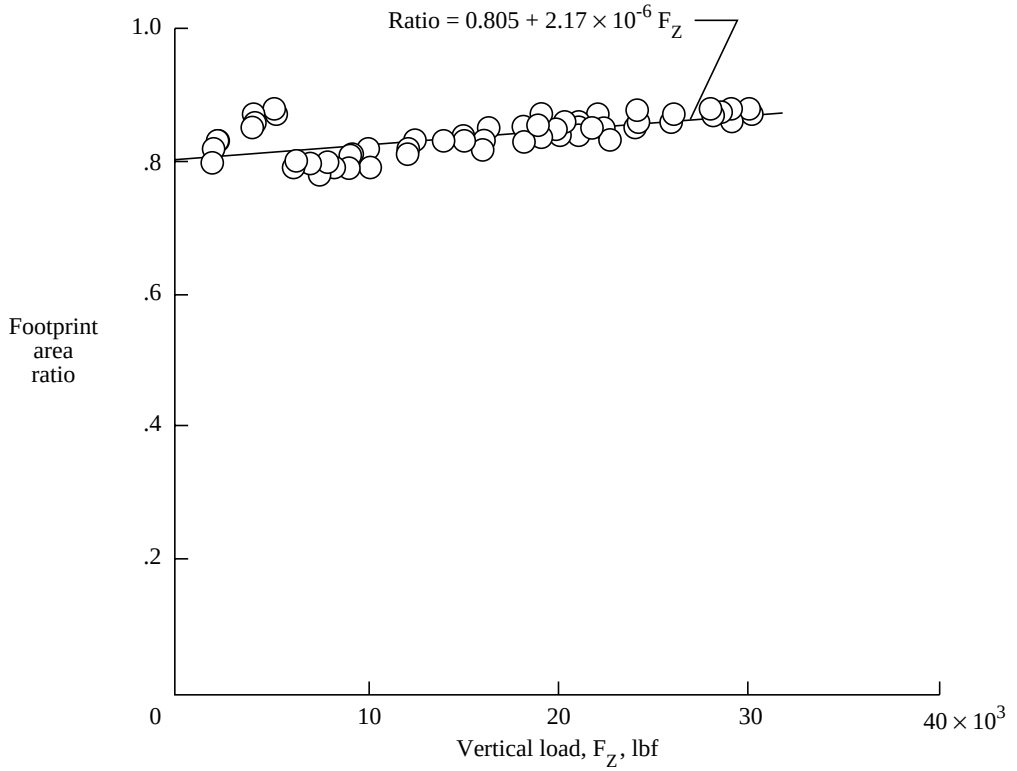

Figure 12. Footprint area ratio as a function of vertical load for Space Shuttle nose-gear tire. Inflation pressure = 300 psi.

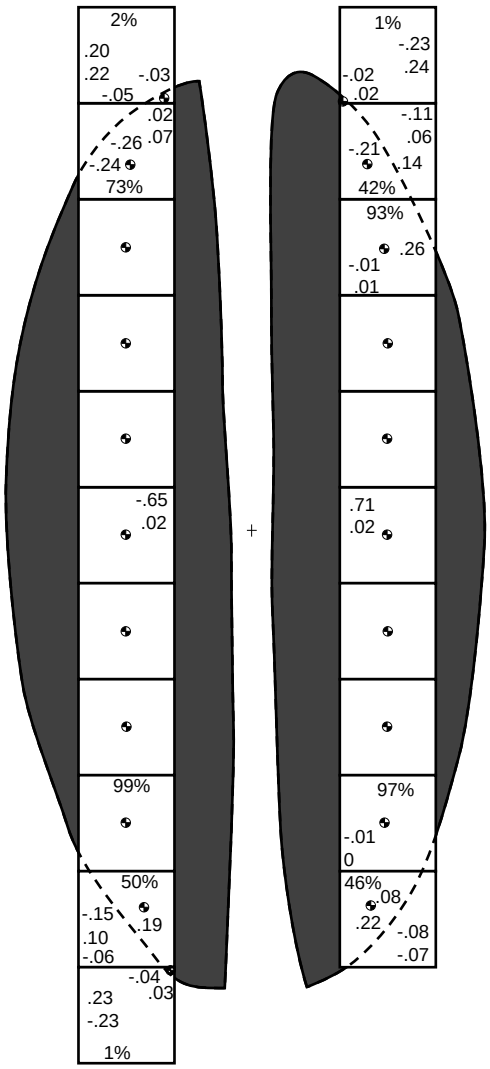

(a) Vertical load = 2000 lbf.

Figure 13. Footprint area and map of tire footprint-force transducer locations for Space Shuttle nose-gear tire.

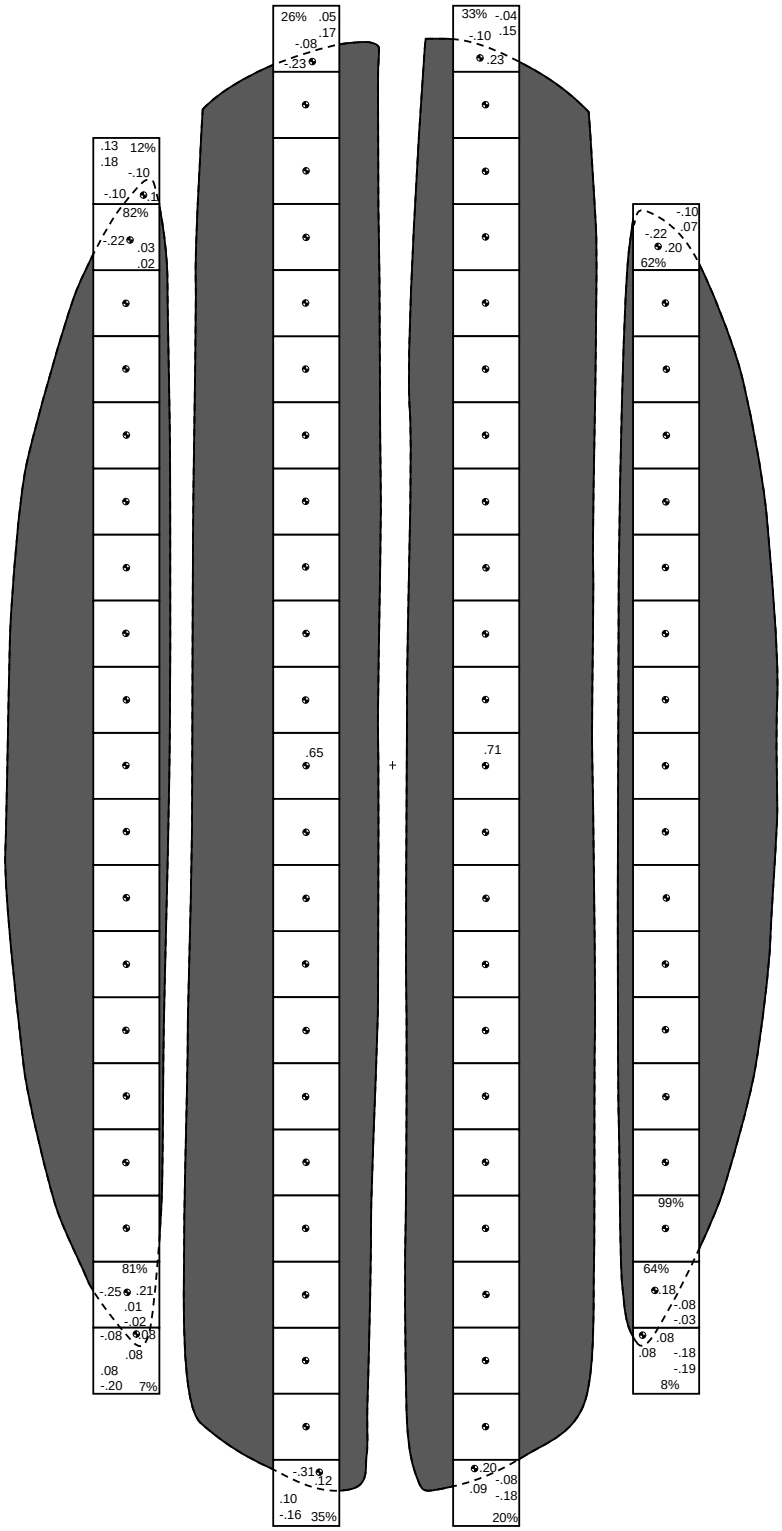

(b) Vertical load = 15000 lbf.

Figure 13. Continued.

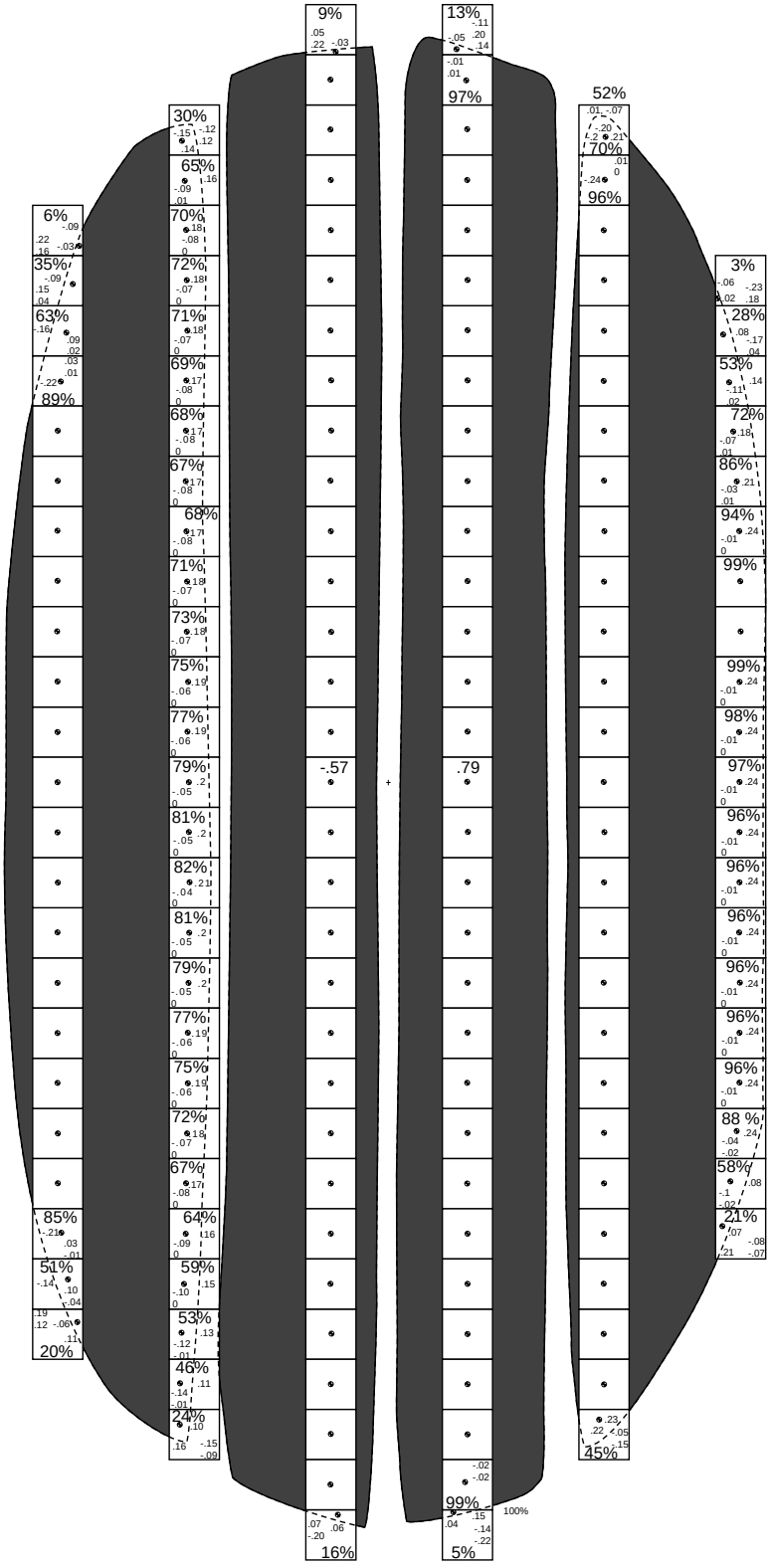

(c) Vertical load = 30 000 lbf.

Figure 13. Concluded.

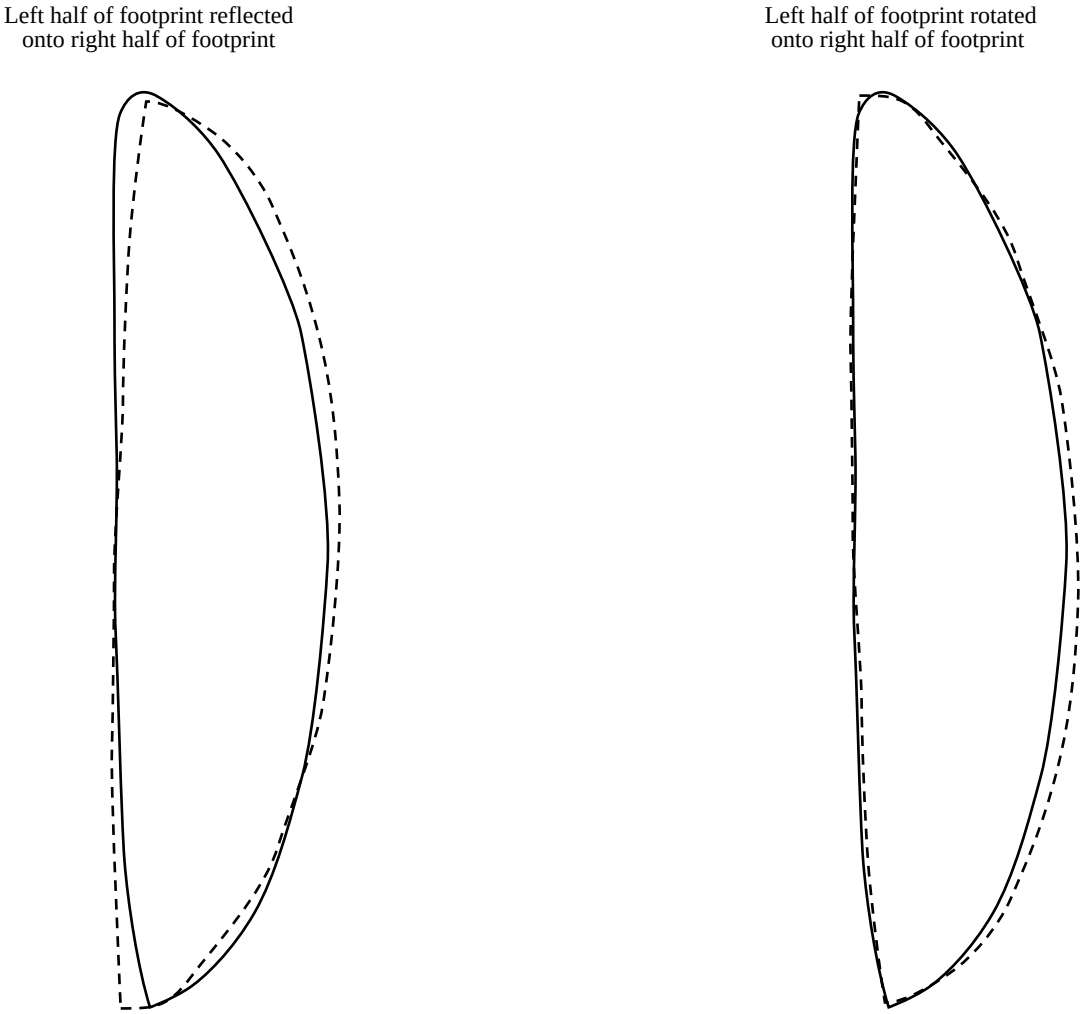

(a) Vertical load = 2000 lbf.

Figure 14. Symmetries exhibited by footprint of Space Shuttle nose-gear tire.

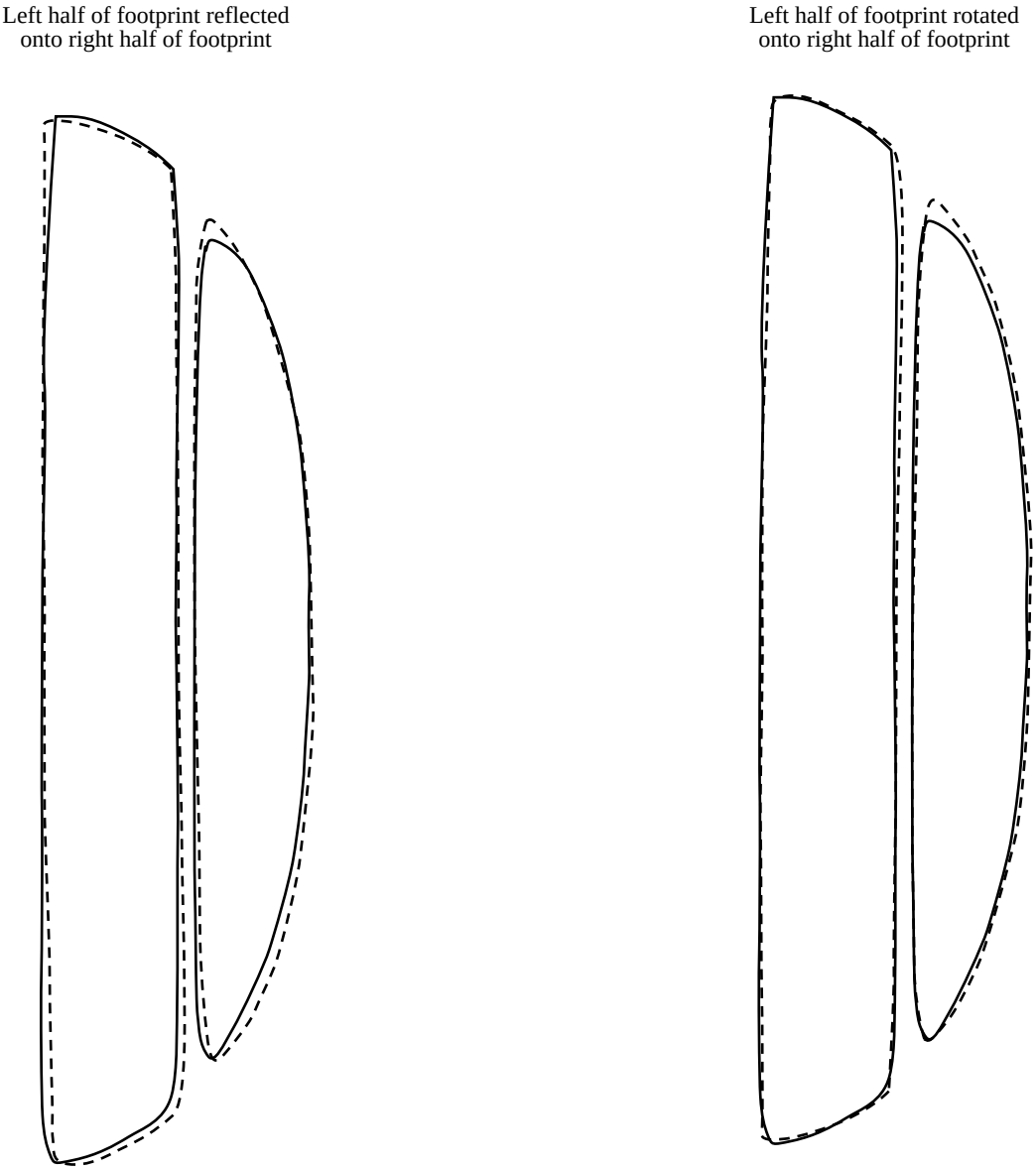

(b) Vertical load = 15000 lbf.

Figure 14. Continued.

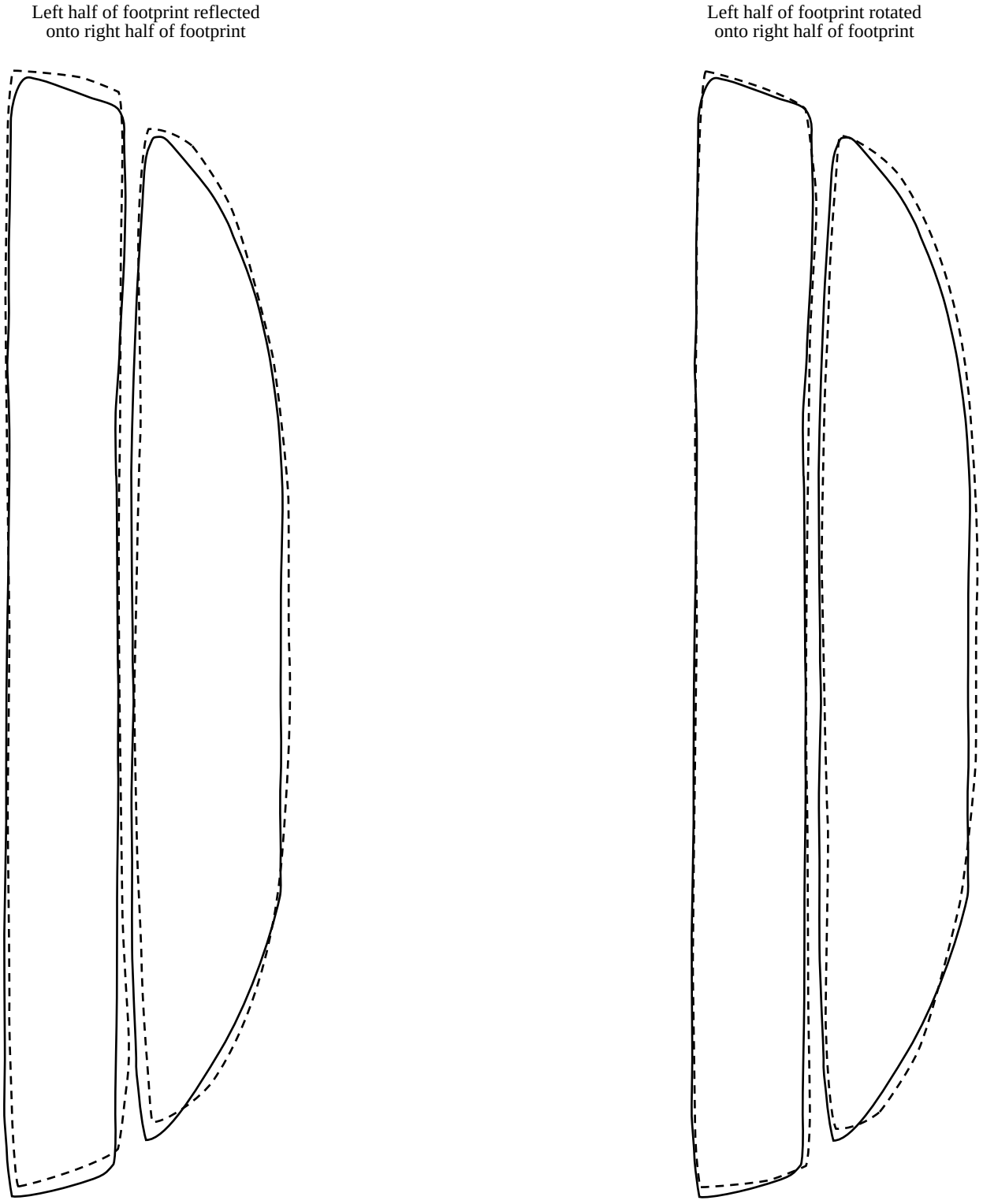

(c) Vertical load = 30 000 lbf.

Figure 14. Concluded.

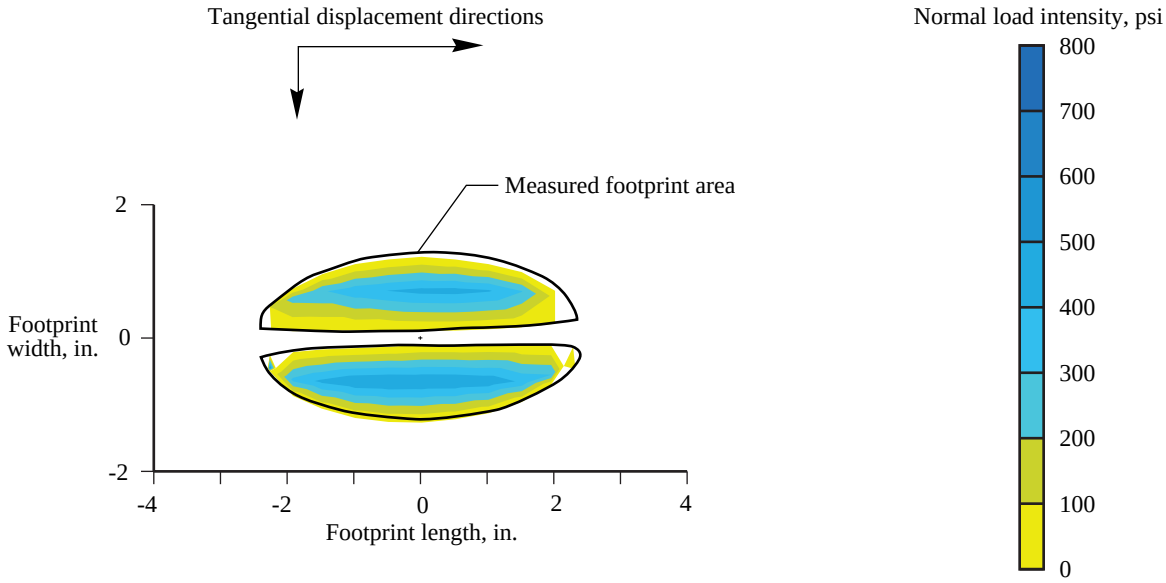

(a) Normal load, 2000 lbf.

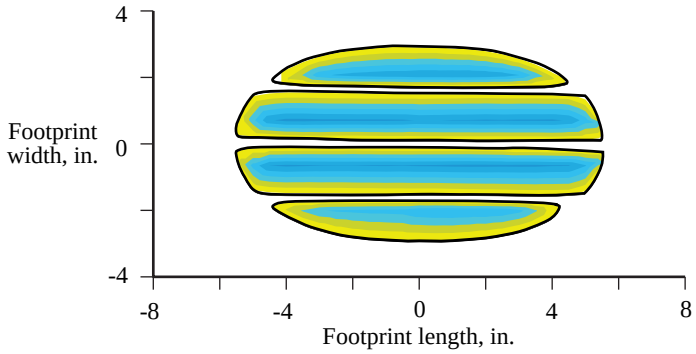

(b) Normal load, 15000 lbf.

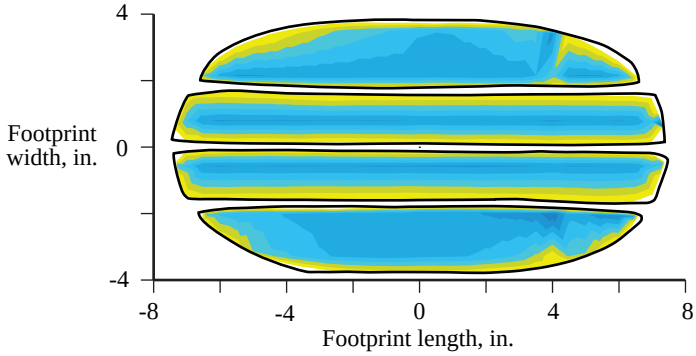

(c) Normal load, 30000 lbf.

Figure 15. Color contour plot of measured footprint normal load-intensity distribution for Space Shuttle orbiter nose-gear tire subjected to an inflation pressure of 300 psi.

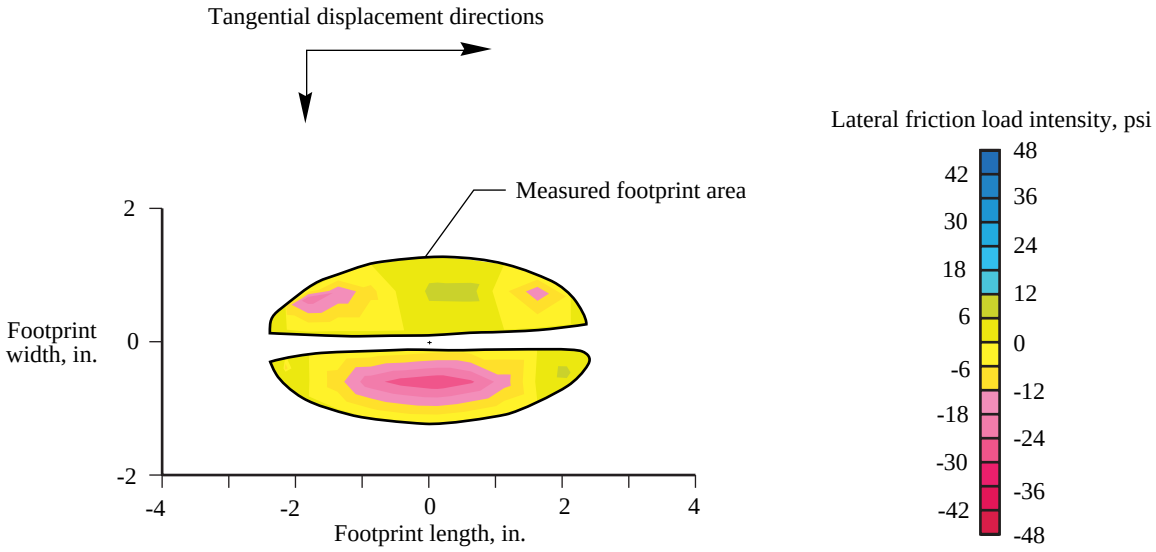

(a) Lateral friction load intensity for a normal load of 2000 lbf.

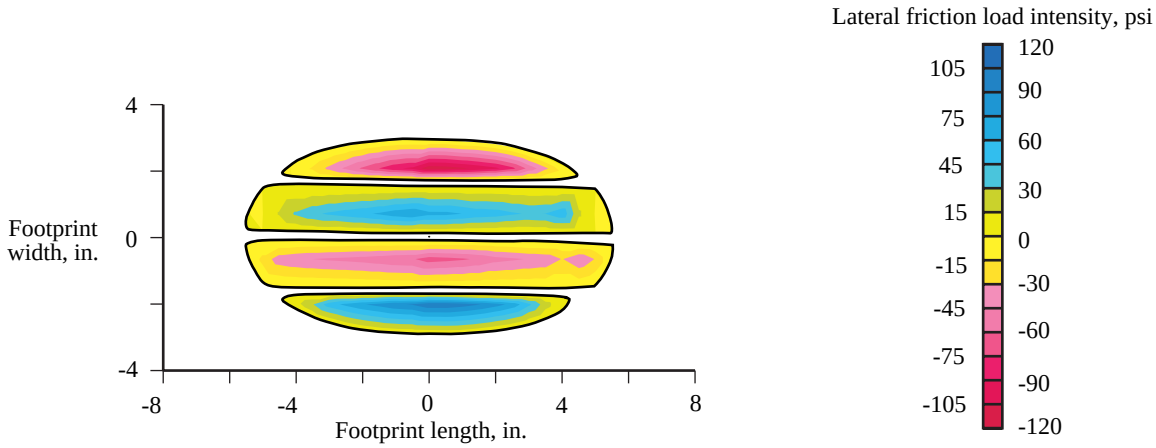

(b) Lateral friction load intensity for a normal load of 15000 lbf.

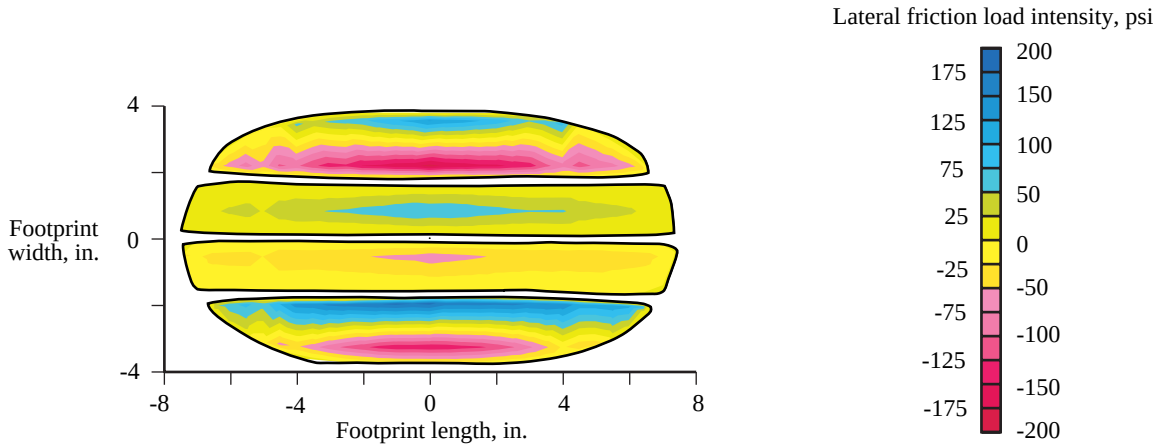

(c) Lateral friction load intensity for a normal load of 30000 lbf.

Figure 16. Color contour plot of measured footprint lateral load-intensity distribution for Space Shuttle orbiter nose-gear tire subjected to an inflation pressure of 300 psi.

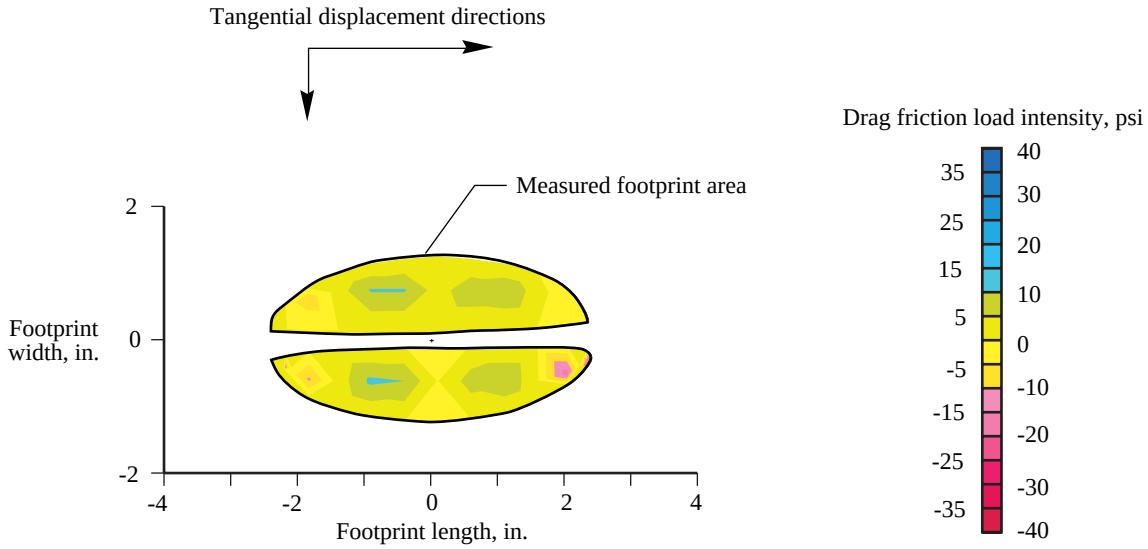

(a) Drag friction load intensity for a normal load of 2000 lbf.

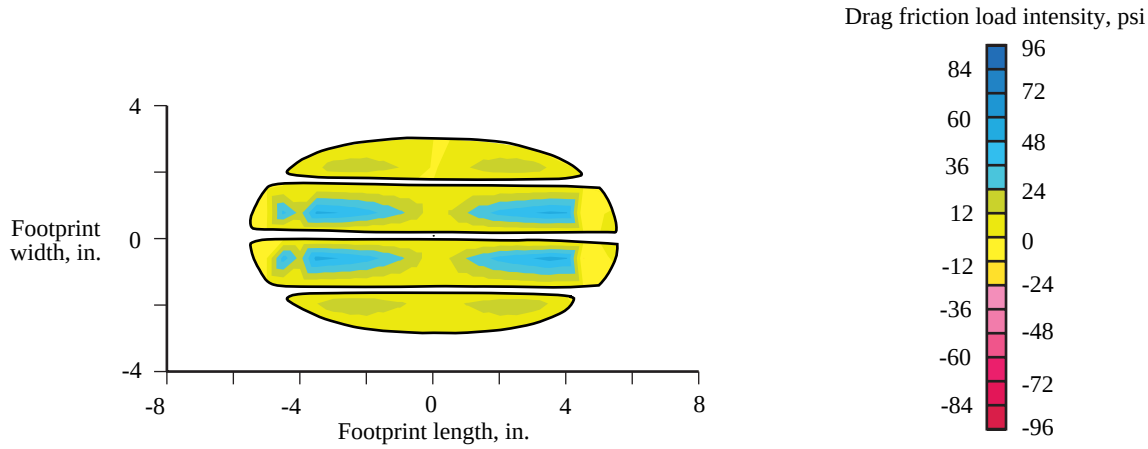

(b) Drag friction load intensity for a normal load of 15000 lbf.

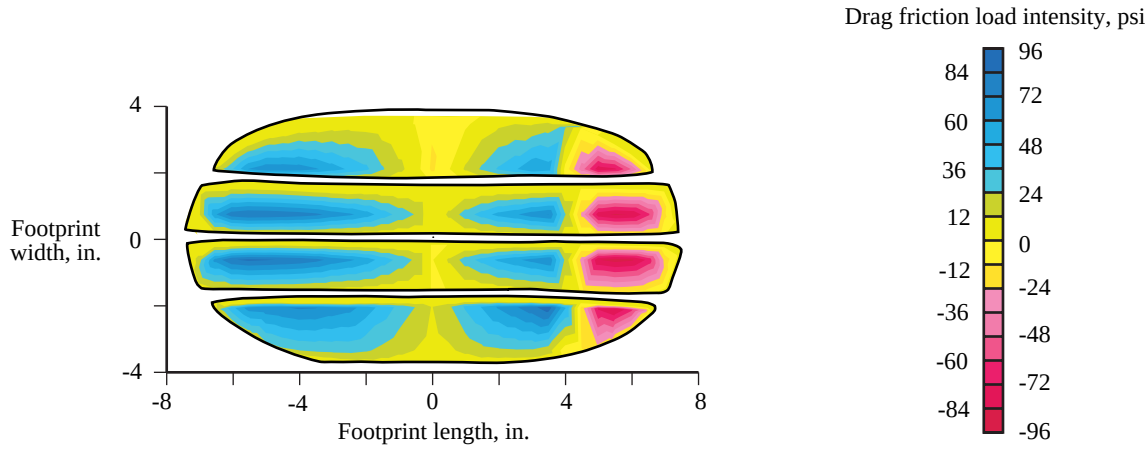

(c) Drag friction load intensity for a normal load of 30000 lbf.

Figure 17. Color contour plot of measured footprint drag load-intensity distribution for Space Shuttle orbiter nose-gear tire subjected to an inflation pressure of 300 psi.

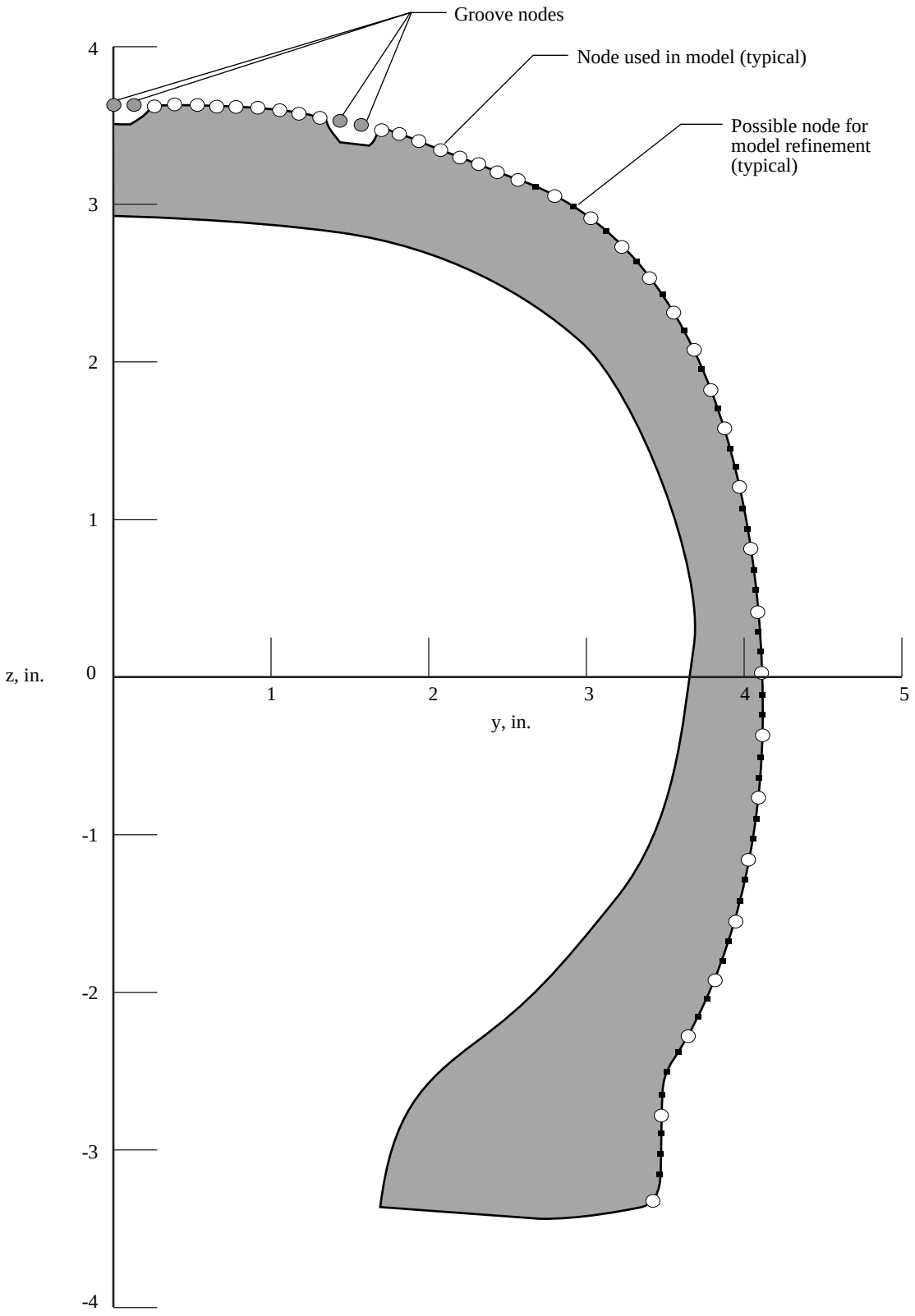

Figure 18. Meridional profile of Space Shuttle nose-gear tire models denoting node point locations.

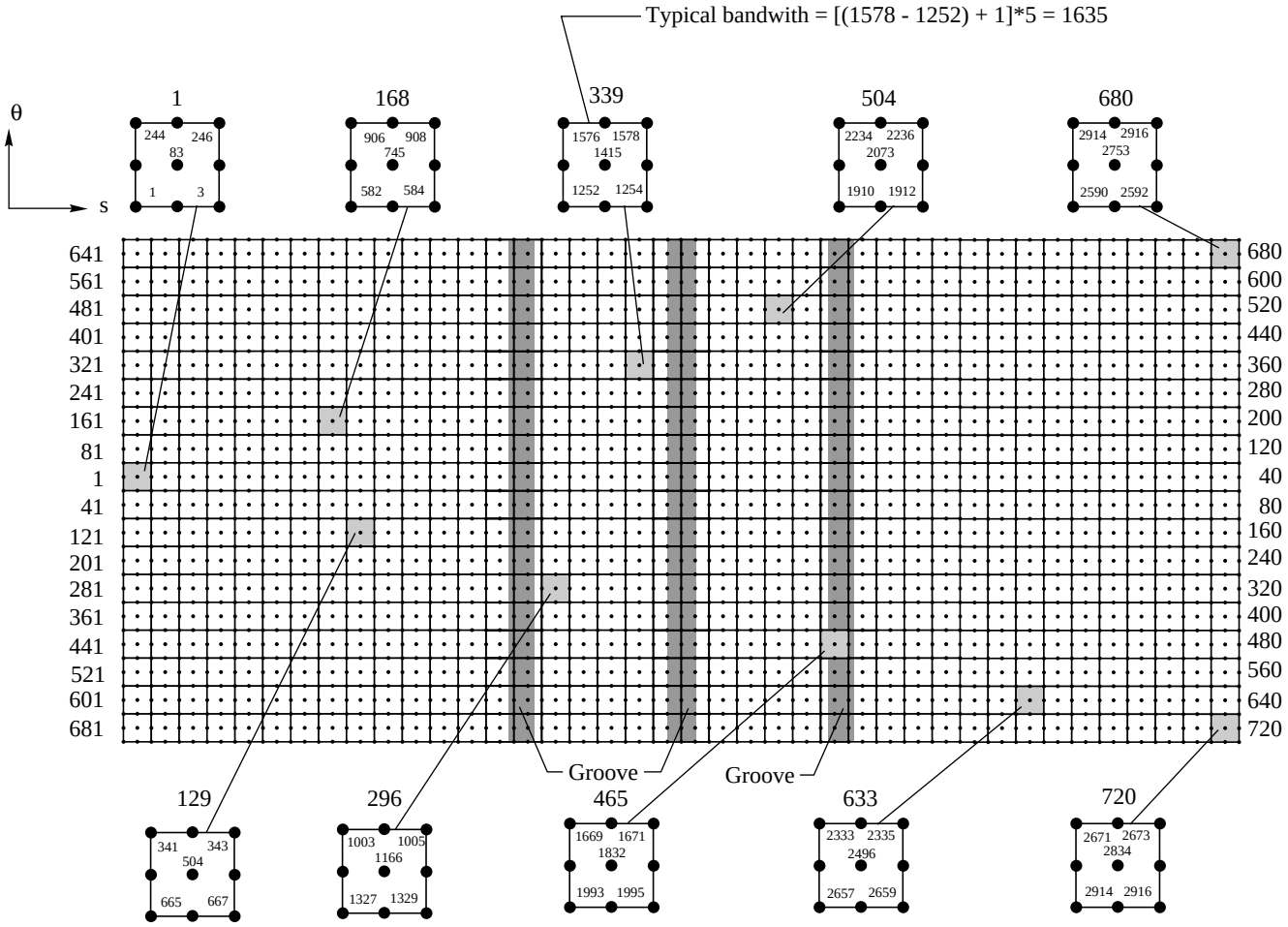

Figure 19. Typical array of finite elements and nodes used to model Space Shuttle nose-gear tire.

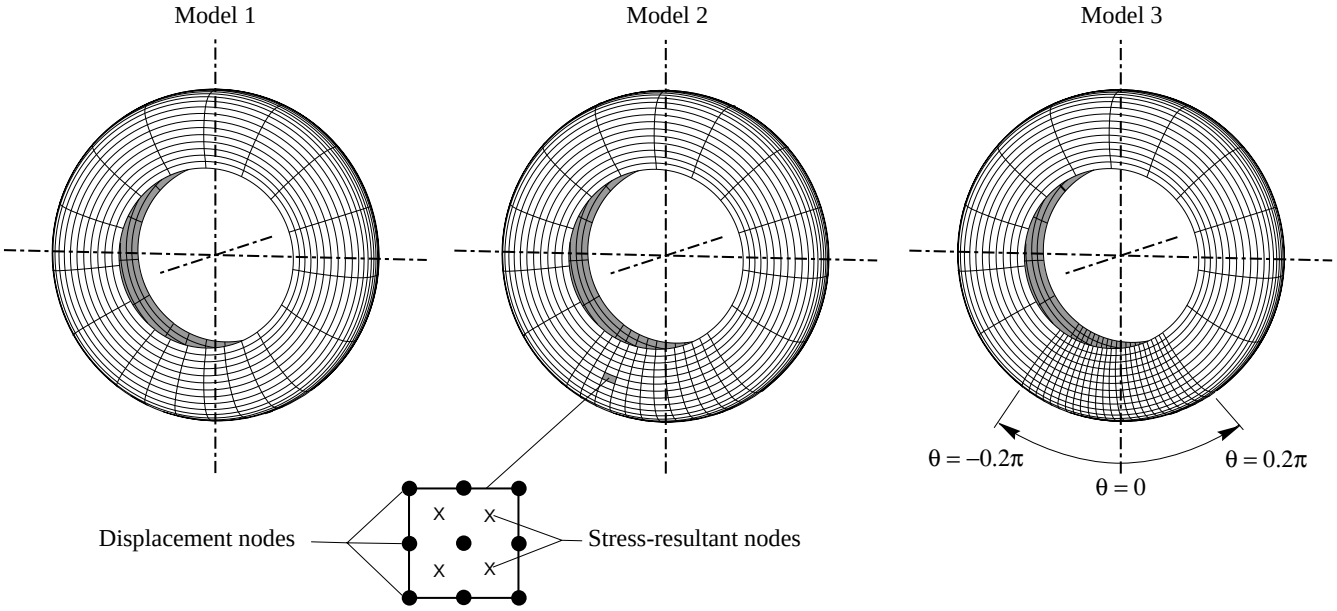

Sector	Number of elements (M9-4) for—		
	Model 1	Model 2	Model 3
$-0.2\pi \le \theta \le 0.2\pi$	240 (40 × 6)	480 (40 × 12)	960 (40 × 24)
$\theta < -0.2\pi, \theta > 0.2\pi$	480 (40 × 12)	480 (40 × 12)	480 (40 × 12)
Total	720 (40 × 18)	960 (30 × 24)	1440 (40 × 36)

Figure 20. Finite-element models of Space Shuttle nose-gear tire used in present study.

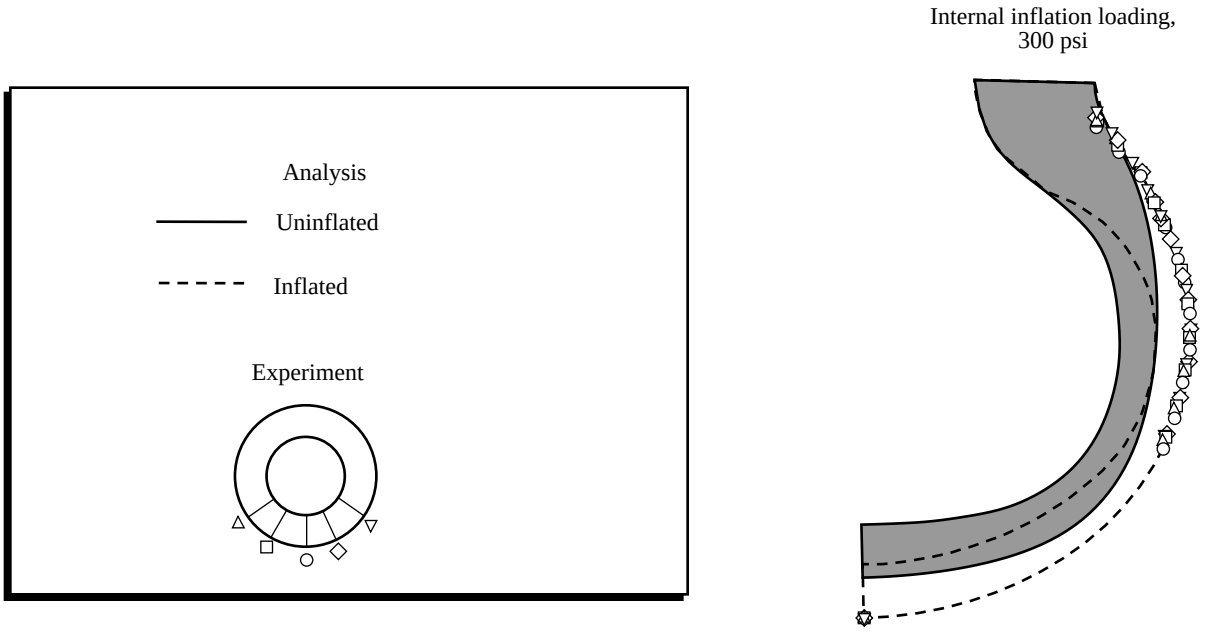

Figure 21. Inflated and uninflated profiles of Space Shuttle nose-gear tire.

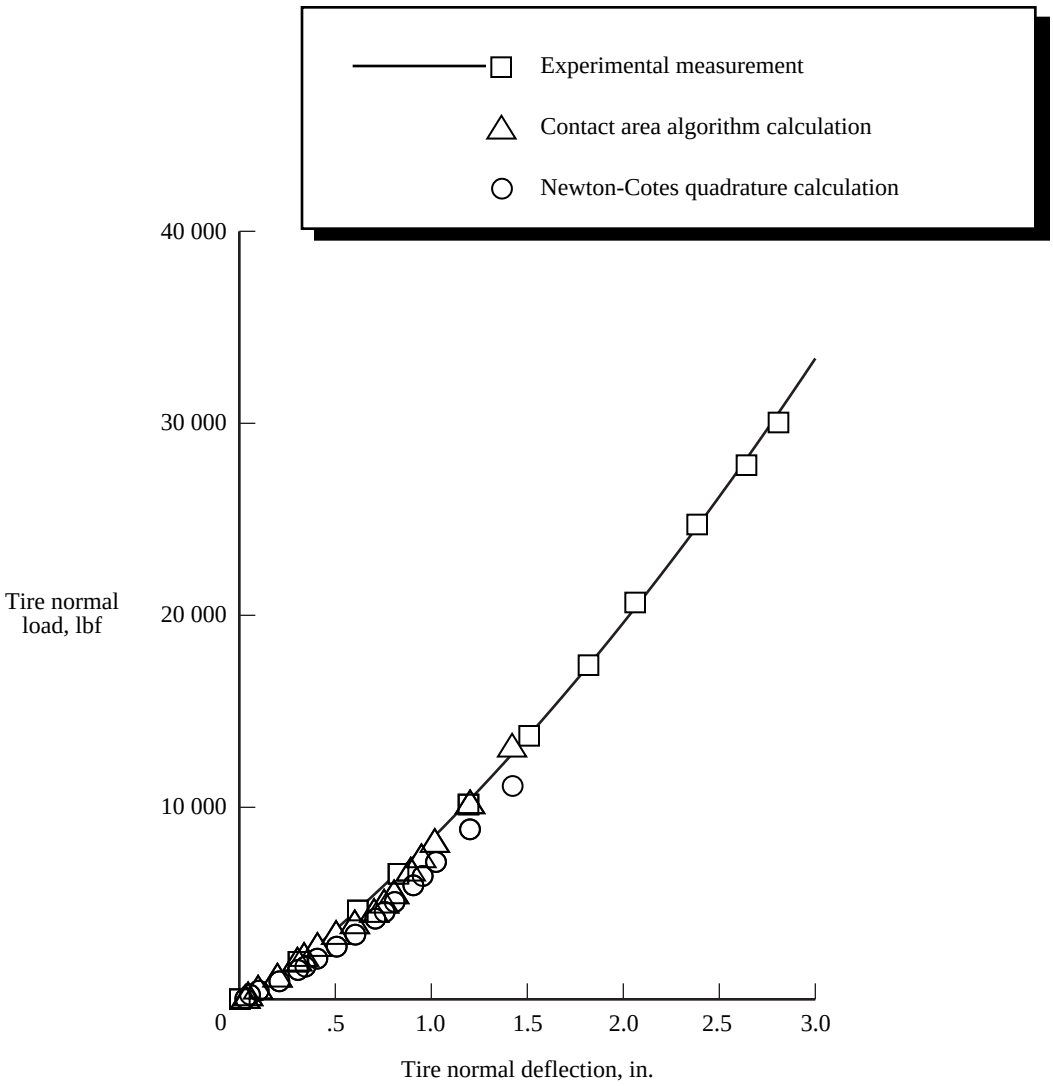

Figure 22. Comparison of calculated and measured normal load-deflection curve for Space Shuttle nose-gear tire. Inflation pressure = 300 psi.

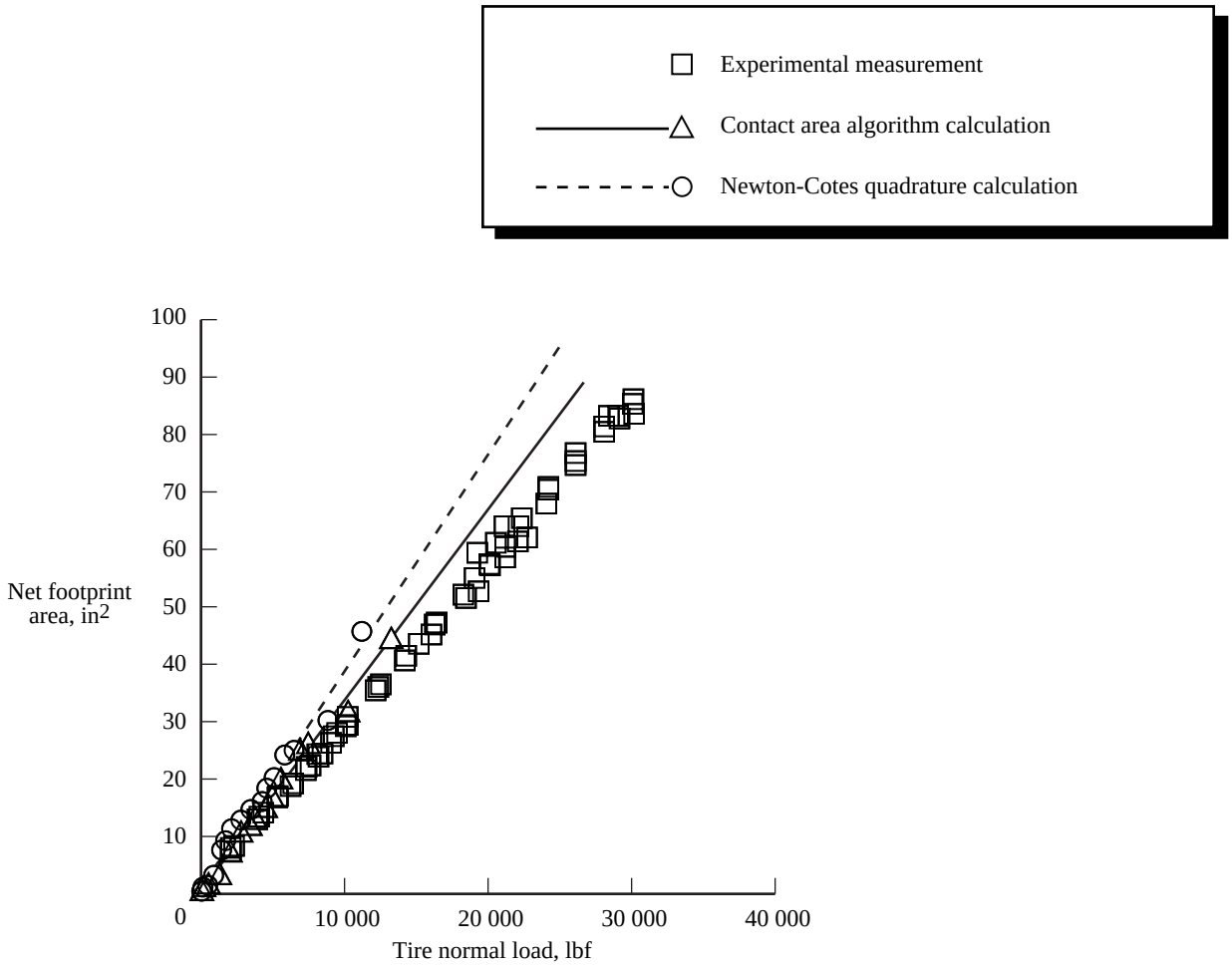

Figure 23. Comparison of calculated and measured net tire footprint areas for Space Shuttle nose-gear tire. Inflation pressure = 300 psi.

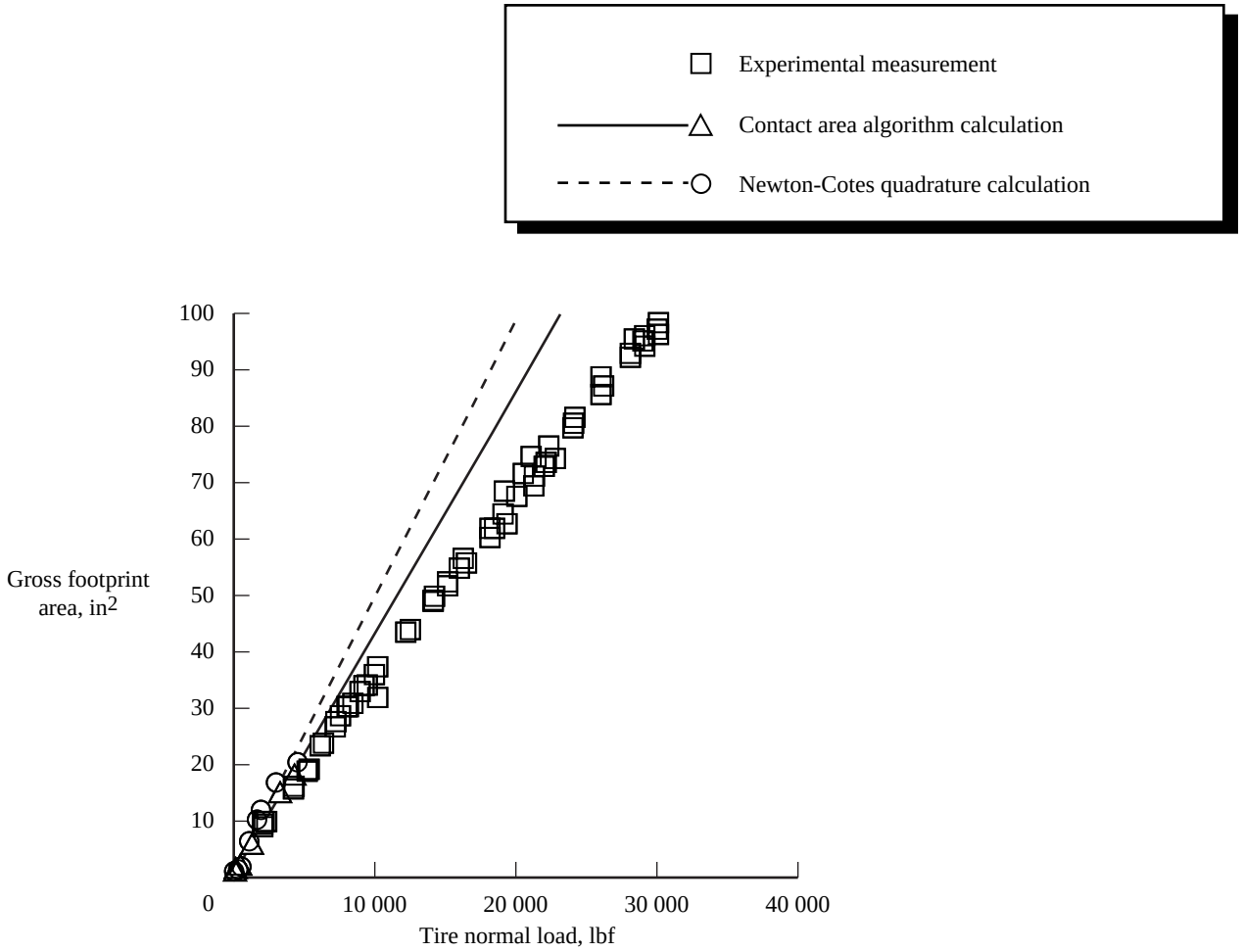

Figure 24. Comparison of calculated and measured gross tire footprint areas for Space Shuttle nose-gear tire. Inflation pressure = 300 psi.

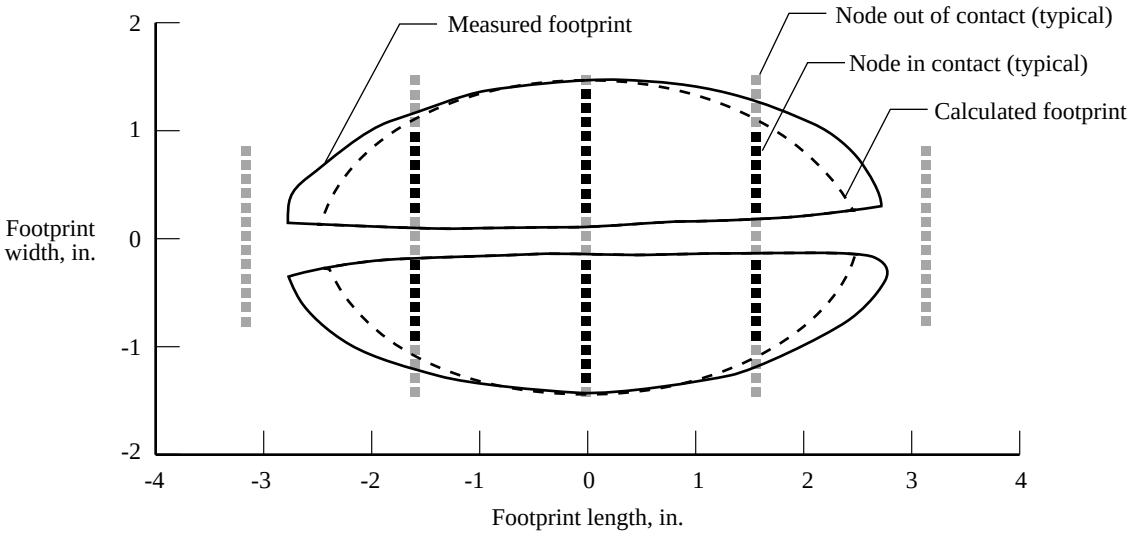

(a) Normal load = 2000 lbf.

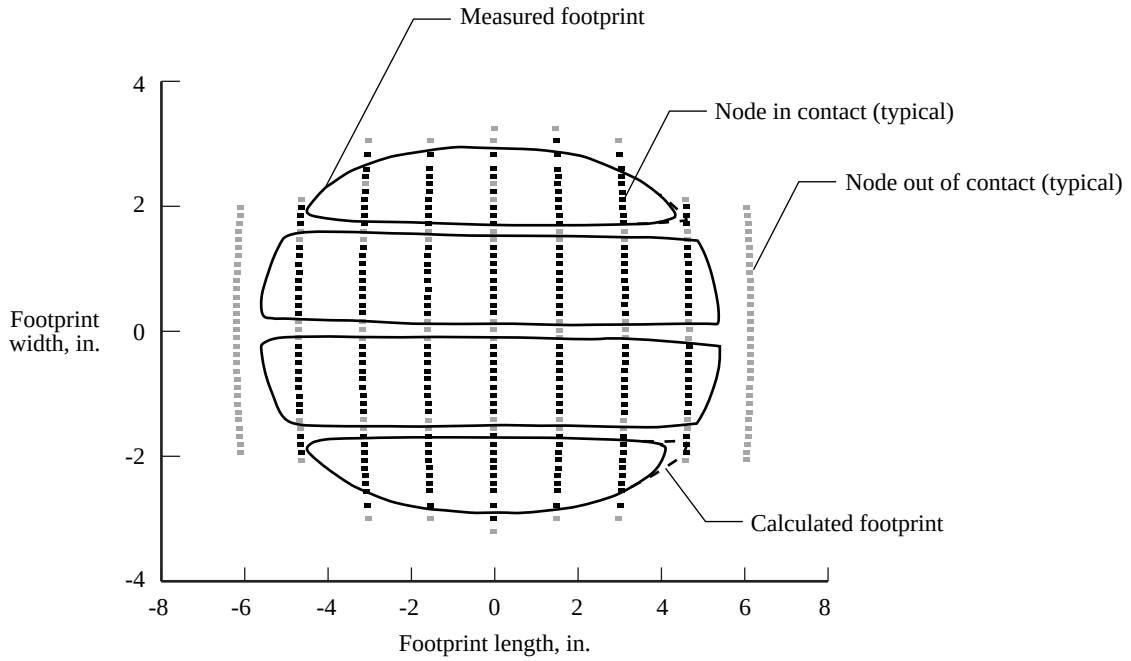

(b) Normal load = 15000 lbf.

Figure 25. Measured and calculated footprints for Space Shuttle nose-gear tire. Inflation pressure = 300 psi; analytical results from model 1.

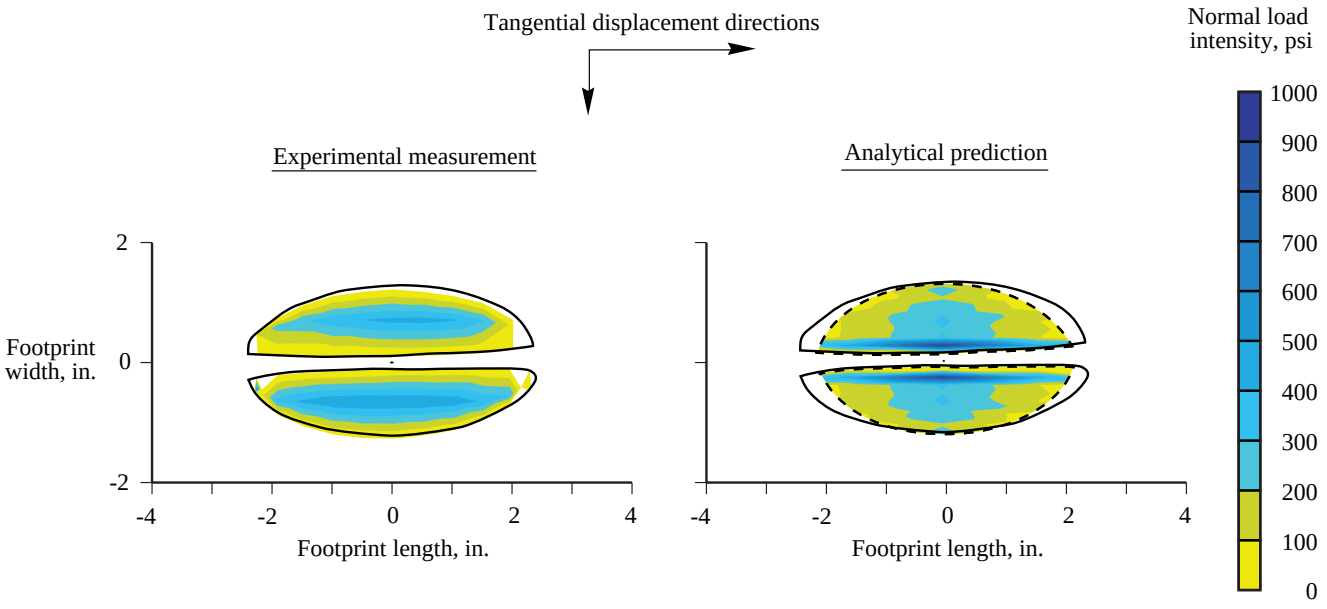

(a) Normal load = 2000 lbf.

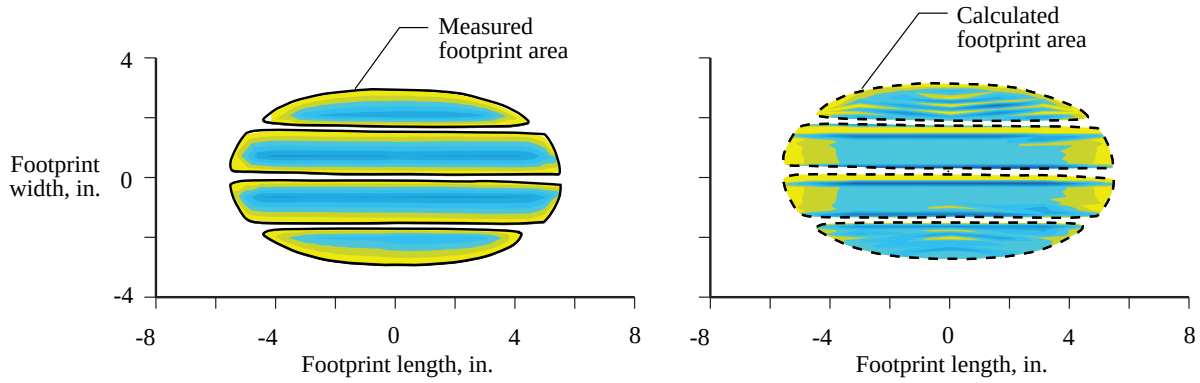

(b) Normal load = 15 000 lbf.

Figure 26. Comparison of measured and predicted footprint normal load-intensity distribution for Space Shuttle nose-gear tire subjected to an inflation pressure of 300 psi. For model 1: μ_{static} = 0.6; $\mu_{dynamic}$ = 0.51; ε_n = 1.0E+12; ε_t = 2.0E+03; ε_{relax} = 0.5.

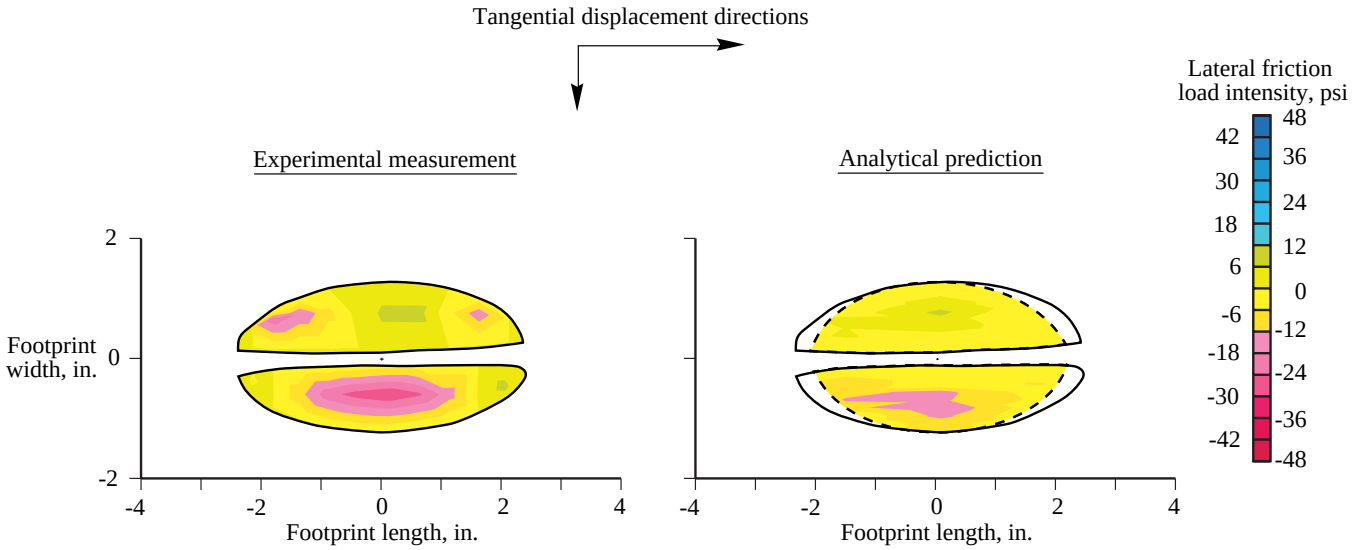

(a) Lateral friction load intensity for a normal load of 2000 lbf.

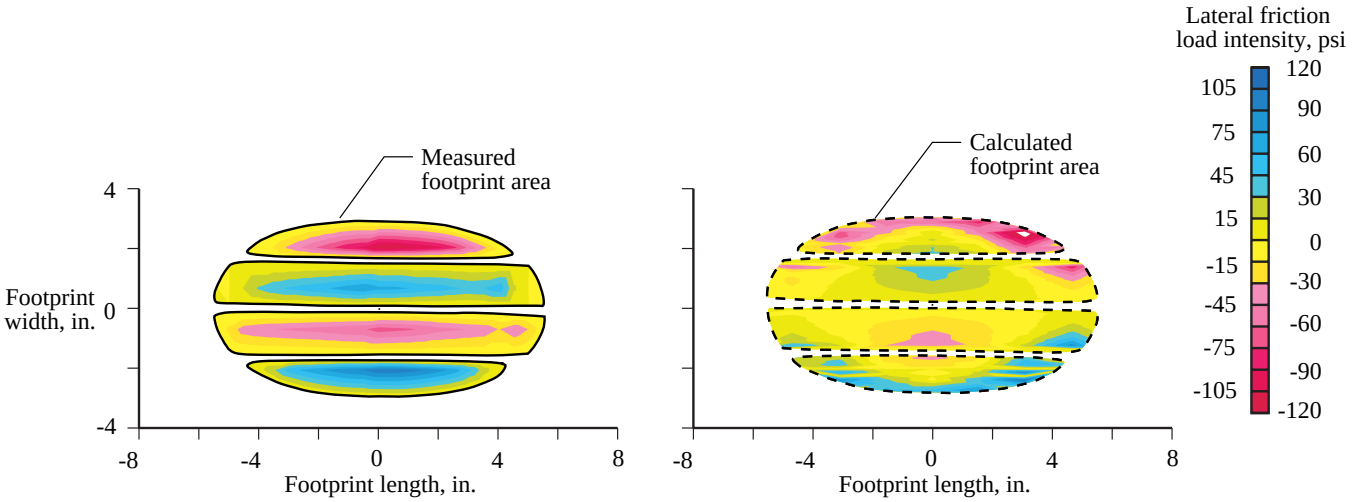

(b) Lateral friction load intensity for a normal load of 15000 lbf.

Figure 27. Comparison of measured and predicted footprint lateral friction load-intensity distribution for Space Shuttle nose-gear tire subjected to an inflation pressure of 300 psi. For model 1: μ_{static} = 0.6; $\mu_{dynamic}$ = 0.51; ε_n = 1.0E+12; ε_t = 2.0E+03; ε_{relax} = 0.5.

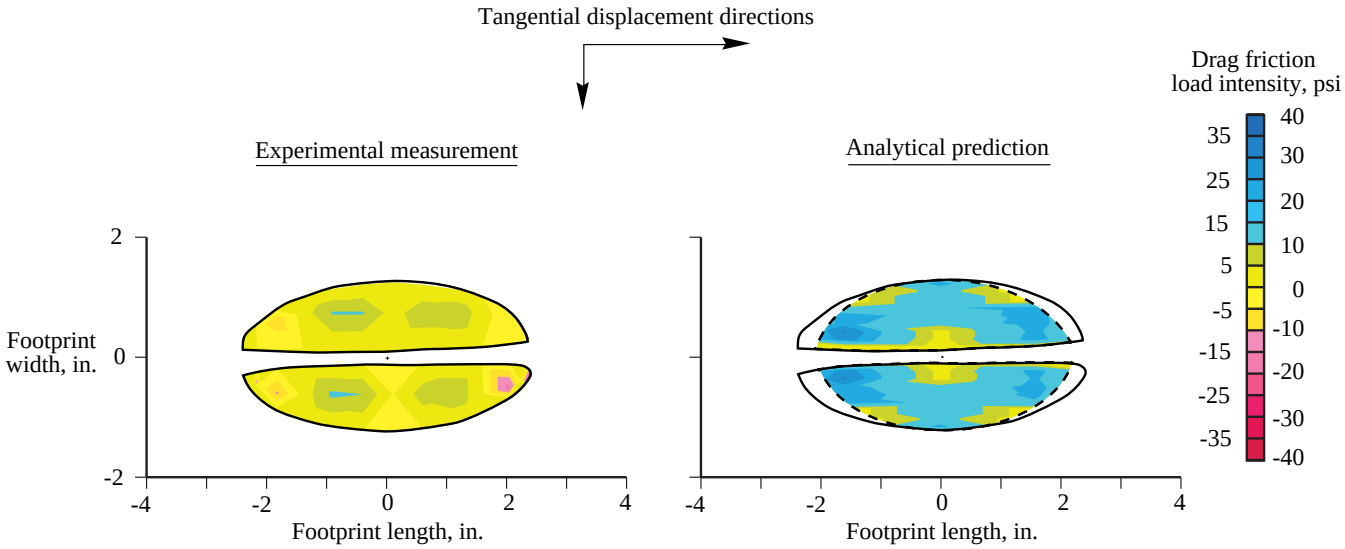

(a) Drag friction load intensity for a normal load of 2000 lbf.

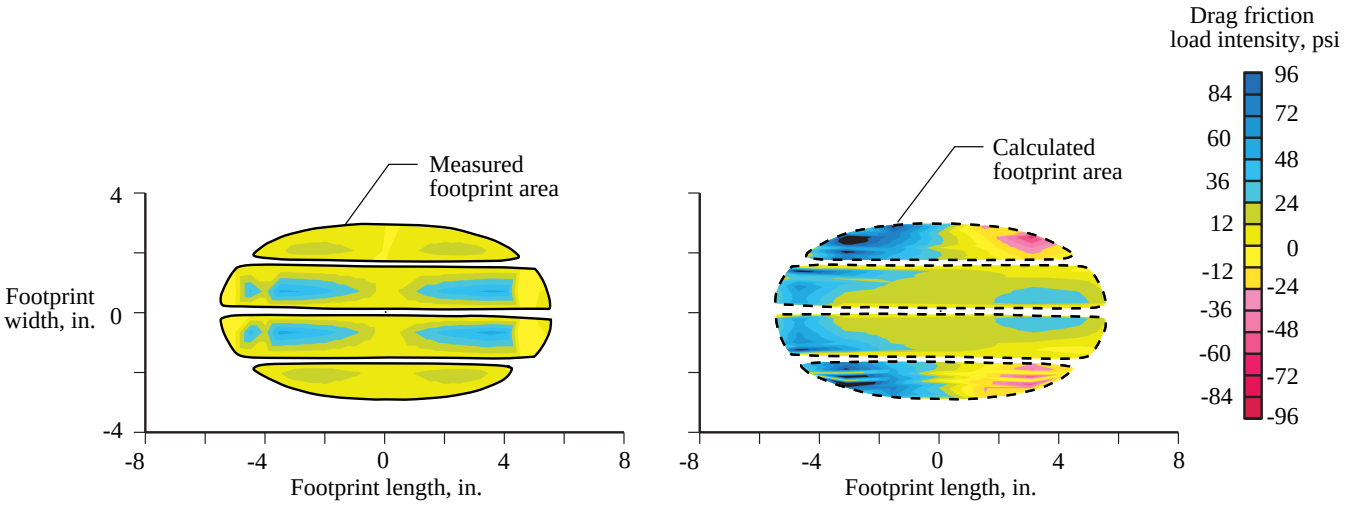

(b) Drag friction load intensity for a normal load of 15000 lbf.

Figure 28. Comparison of measured and predicted footprint drag friction load-intensity distribution for Space Shuttle nose-gear tire subjected to an inflation pressure of 300 psi. For model 1: μ_{static} = 0.6; $\mu_{dynamic}$ = 0.51; ε_n = 1.0E+12; ε_t = 2.0E+03; ε_{relax} = 0.5.

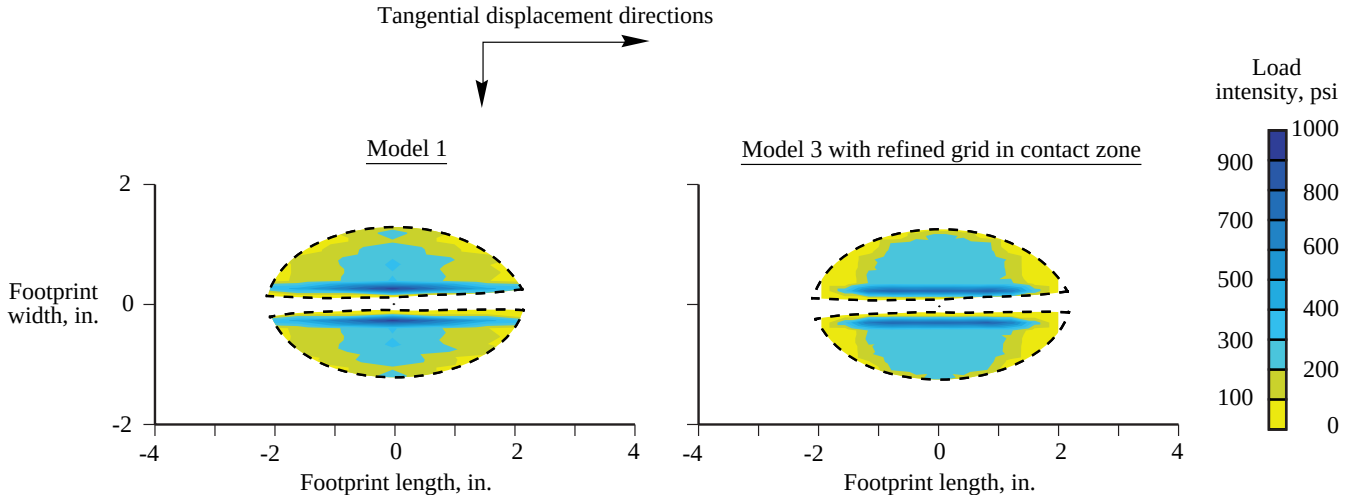

(a) Normal load = 2000 lbf.

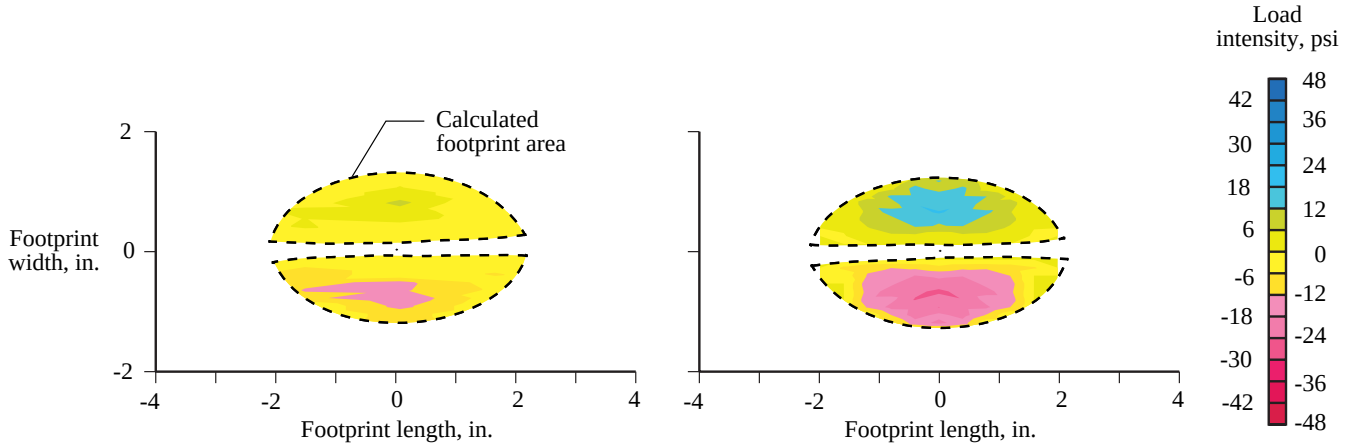

(b) Lateral friction load intensity, normal load = 2000 lbf.

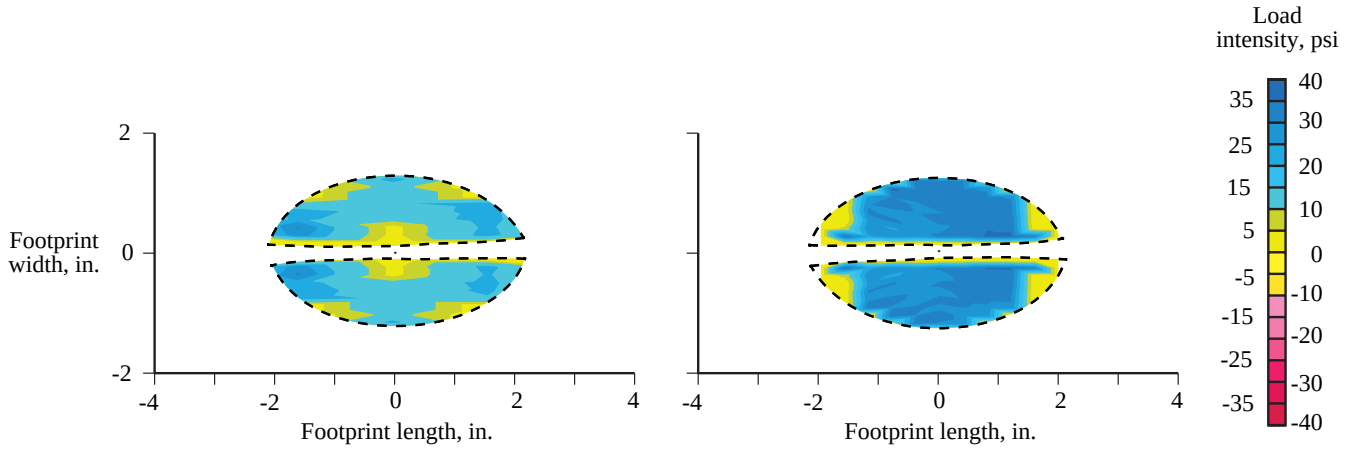

(c) Drag friction load intensity, normal load = 2000 lbf.

Figure 29. Effect of contact-area grid refinement on predicted contact load-intensity distributions. Space Shuttle nose-gear tire subjected to an inflation pressure of 300 psi and unsymmetric static loading conditions. For model 1: μ_{static} = 0.6; $\mu_{dynamic}$ = 0.51; ε_n = 1.0E+12; ε_t = 2.0E+03; ε_{relax} = 0.5.

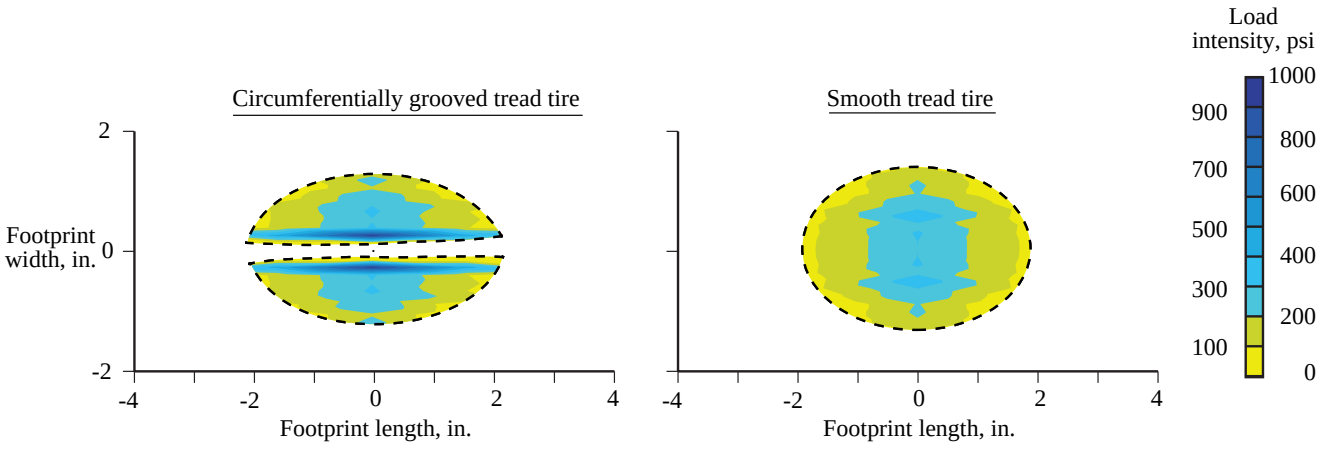

(a) Normal load = 2000 lbf.

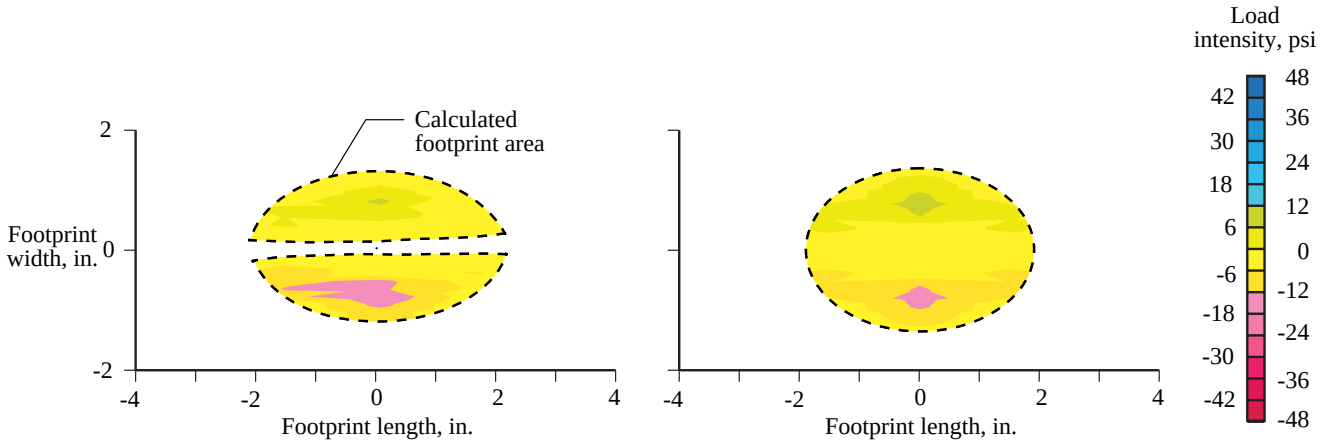

(b) Lateral friction load intensity, normal load = 2000 lbf.

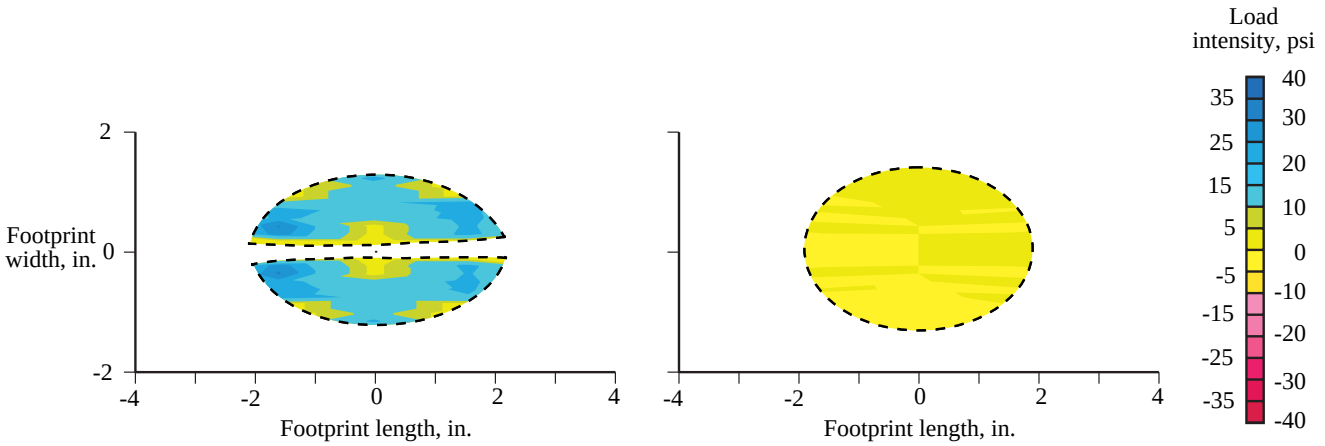

(c) Drag friction load intensity, normal load = 2000 lbf.

Figure 30. Comparison of circumferentially-grooved tread tire and smooth-tread tire contact load intensities. Space Shuttle nose-gear tire subjected to an inflation pressure of 300 psi and symmetric static loading conditions. For model 1: μ_{static} = 0.6; $\mu_{dynamic}$ = 0.51; ε_n = 1.0E+12; ε_t = 2.0E+03; ε_{relax} = 0.5.

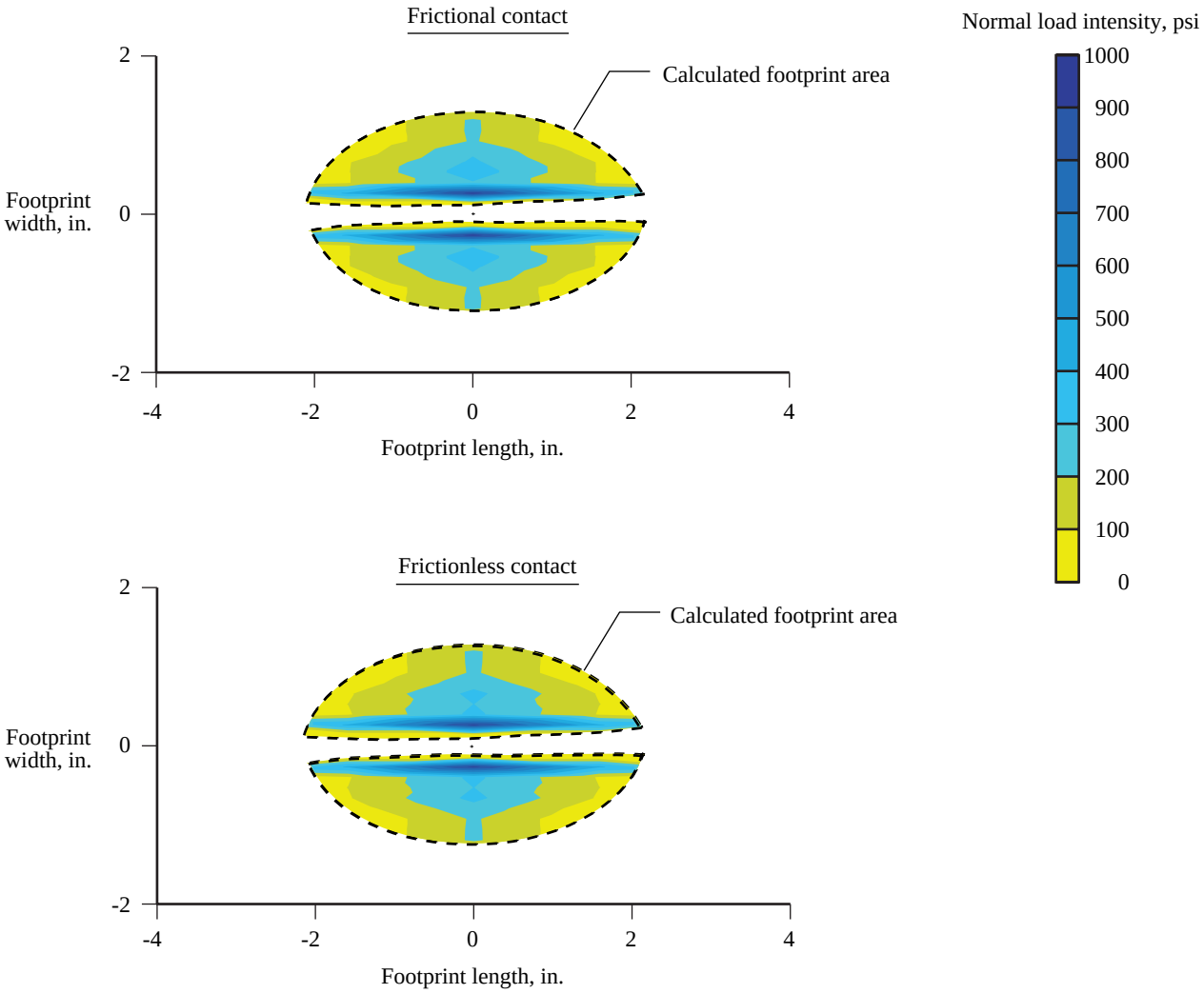

Figure 31. Comparison of normal load intensities from frictional and frictionless contact. Space Shuttle nose-gear tire subjected to an inflation pressure of 300 psi and symmetric static loading conditions. For model 1: $\mu_{static} = 0.6$; $\mu_{dynamic} = 0.51$; $\varepsilon_n = 1.0E+12$; $\varepsilon_t = 2.0E+03$; $\varepsilon_{relax} = 0.5$.

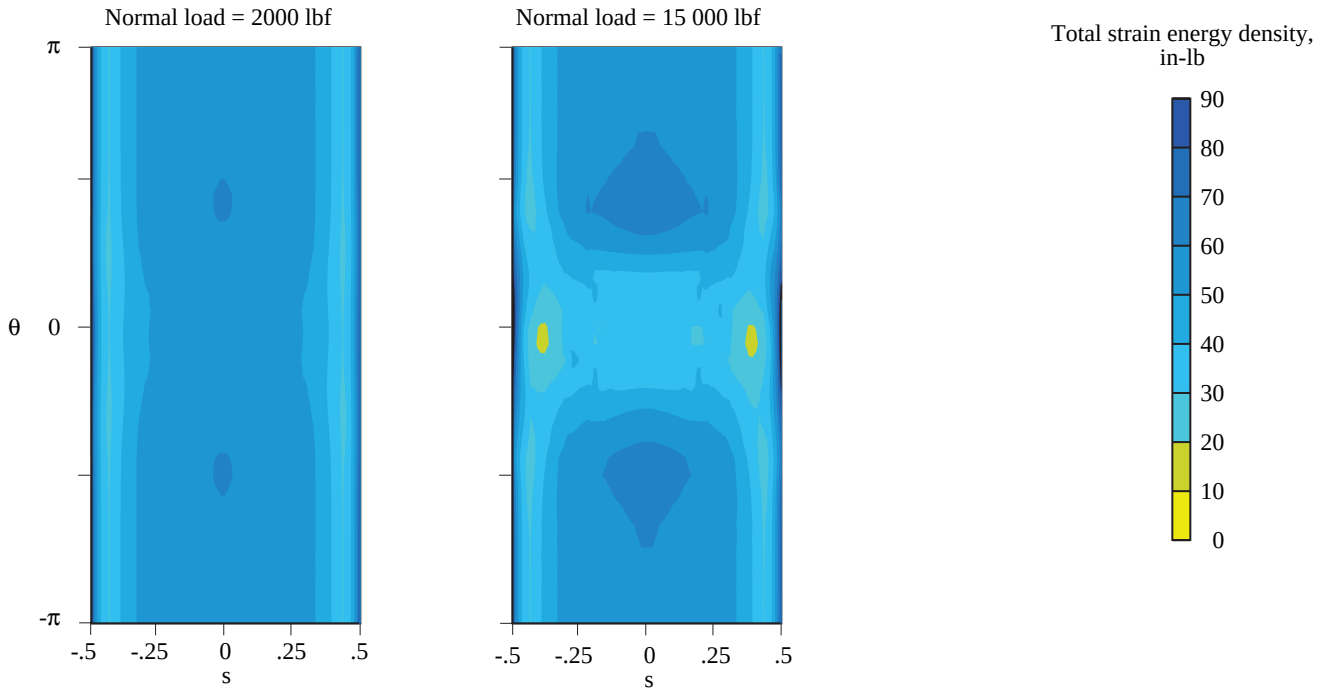

(a) Total strain energy density.

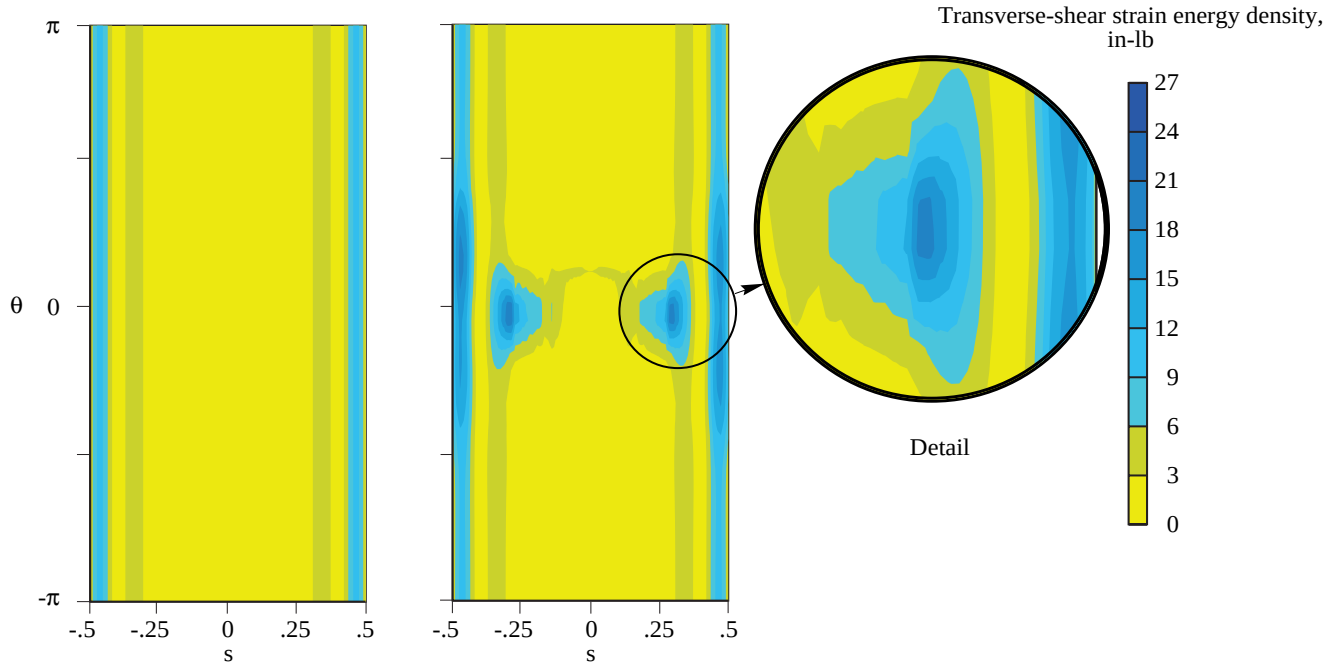

(b) Transverse-shear strain energy density.

Figure 32. Variation of calculated strain energy density distribution. Space Shuttle nose-gear tire subjected to an inflation pressure of 300 psi and symmetric static loading conditions. For model 1: μ_{static} = 0.6; $\mu_{dynamic}$ = 0.51; ε_n = 1.0E+12; ε_t = 2.0E+03; ε_{relax} = 0.5.

REPORT DOCUMENTATION PAGE

Form Approved
OMB No. 0704-0188

1. AGENCY USE ONLY *(Leave blank)*	2. REPORT DATE	3. REPORT TYPE AND DATES COVERED
	May 1996	Technical Paper

4. TITLE AND SUBTITLE
Computational Methods for Frictional Contact With Applications to the Space Shuttle Orbiter Nose-Gear Tire
Comparisons of Experimental Measurements and Analytical Predictions

5. FUNDING NUMBERS
WU 505-63-50-19

6. AUTHOR(S)
John A. Tanner

7. PERFORMING ORGANIZATION NAME(S) AND ADDRESS(ES)
NASA Langley Research Center
Hampton, VA 23681-0001

8. PERFORMING ORGANIZATION REPORT NUMBER
L-17211A

9. SPONSORING/MONITORING AGENCY NAME(S) AND ADDRESS(ES)
National Aeronautics and Space Administration
Washington, DC 20546-0001

10. SPONSORING/MONITORING AGENCY REPORT NUMBER
NASA TP-3573

11. SUPPLEMENTARY NOTES

12a. DISTRIBUTION/AVAILABILITY STATEMENT
Unclassified–Unlimited
Subject Category 39
Availability: NASA CASI (301) 621-0390

12b. DISTRIBUTION CODE

13. ABSTRACT *(Maximum 200 words)*

A computational procedure is presented for the solution of frictional contact problems for aircraft tires. A Space Shuttle nose-gear tire is modeled using a two-dimensional laminated anisotropic shell theory which includes the effects of variations in material and geometric parameters, transverse-shear deformation, and geometric nonlinearities. Contact conditions are incorporated into the formulation by using a perturbed Lagrangian approach with the fundamental unknowns consisting of the stress resultants, the generalized displacements, and the Lagrange multipliers associated with both contact and friction conditions. The contact-friction algorithm is based on a modified Coulomb friction law. A modified two-field, mixed-variational principle is used to obtain elemental arrays. This modification consists of augmenting the functional of that principle by two terms: the Lagrange multiplier vector associated with normal and tangential node contact-load intensities and a regularization term that is quadratic in the Lagrange multiplier vector. These capabilities and computational features are incorporated into an in-house computer code. Experimental measurements were taken to define the response of the Space Shuttle nose-gear tire to inflation-pressure loads and to inflation-pressure loads combined with normal static loads against a rigid flat plate. These experimental results describe the meridional growth of the tire cross section caused by inflation loading, the static load-deflection characteristics of the tire, the geometry of the tire footprint under static loading conditions, and the normal and tangential load-intensity distributions in the tire footprint for the various static vertical-loading conditions. Numerical results were obtained for the Space Shuttle nose-gear tire subjected to inflation pressure loads and combined inflation pressure and contact loads against a rigid flat plate. The experimental measurements and the numerical results are compared.

14. SUBJECT TERMS
Finite elements; Frictional contact; Nose-gear; Shell theory; Shuttle; Tire modeling

15. NUMBER OF PAGES
55

16. PRICE CODE
A04

17. SECURITY CLASSIFICATION OF REPORT	18. SECURITY CLASSIFICATION OF THIS PAGE	19. SECURITY CLASSIFICATION OF ABSTRACT	20. LIMITATION OF ABSTRACT
Unclassified	Unclassified	Unclassified	

NSN 7540-01-280-5500

Standard Form 298 (Rev. 2-89)
Prescribed by ANSI Std. Z39-18
298-102